On the importance of electronic correlations in potassium-doped organic semiconductors

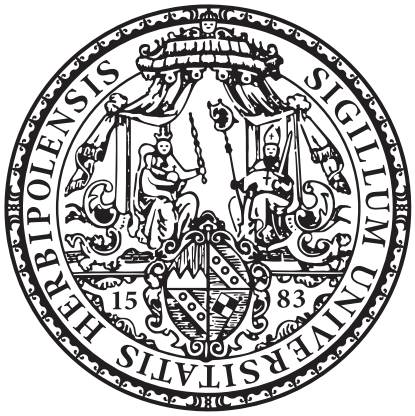

Dissertation zur Erlangung des
naturwissenschaftlichen Doktorgrades der
Julius-Maximilians-Universität Würzburg

vorgelegt von: Andreas Ruff
aus: Würzburg

Würzburg 2013

ep4

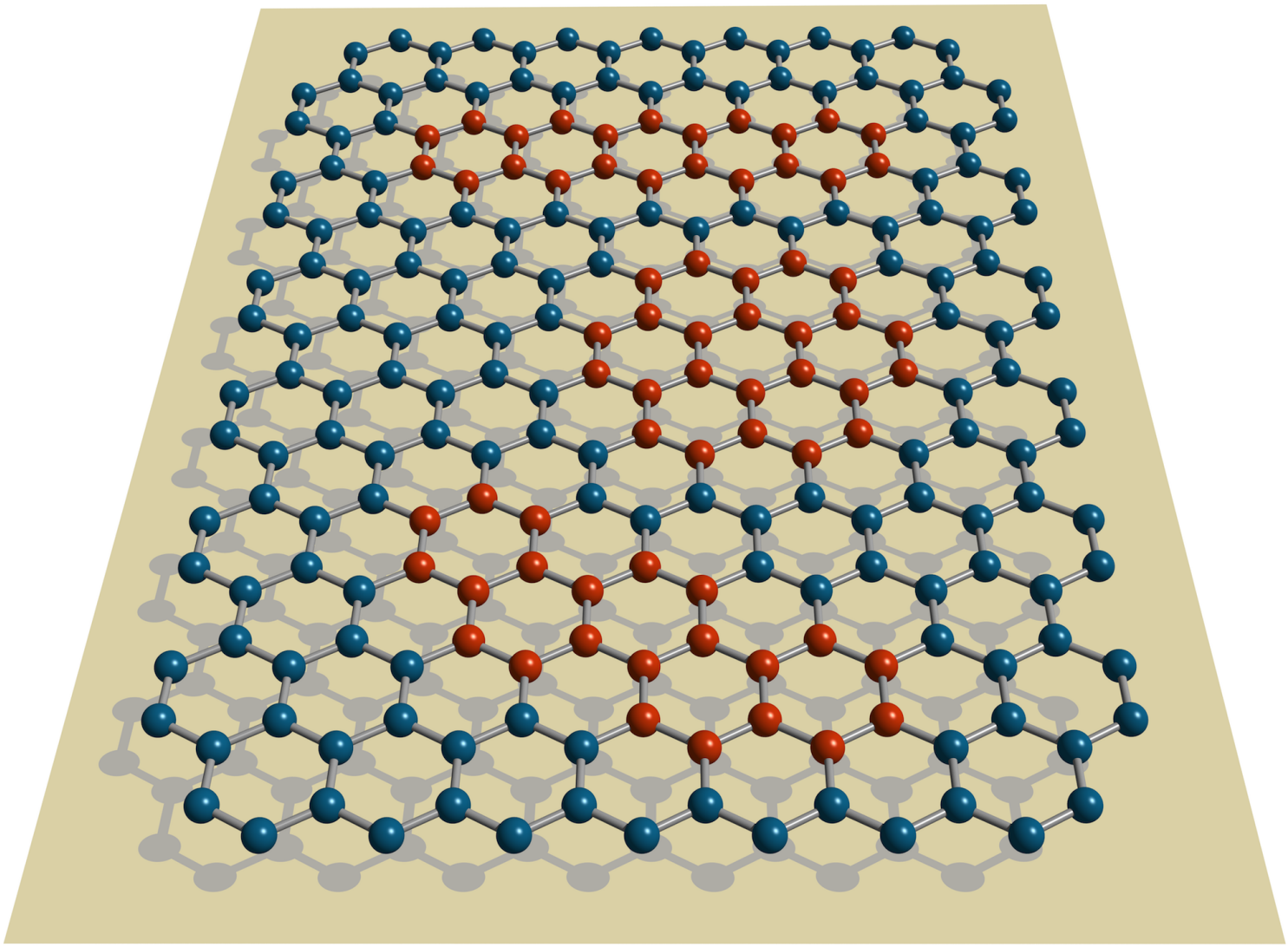

Figure 0: *Nano-graphenes: The molecules pentacene, coronene, and picene as cutouts of a graphene sheet.*

Eingereicht am: 25. April 2013

bei der Fakultät für Physik und Astronomie

Gutachter der Dissertation:

1. Gutachter: Prof. Dr. Ralph Claessen

2. Gutachter: Prof. Dr. Jens Pflaum

Prüfer im Promotionskolloquium:

1. Prüfer: Prof. Dr. Ralph Claessen

2. Prüfer: Prof. Dr. Jens Pflaum

3. Prüfer: Prof. Dr. Roser Valentí (Universität Frankfurt)

Tag des Promotionskolloquiums: 25. Oktober 2013

Zusammenfassung

Die vorliegende Arbeit beschäftigt sich mit der Dotierung organischer Dünnfilme mittels Alkalimetall-Interkalation sowie deren Einfluss auf die elektronische Struktur der Filme. Untersucht wurden zu diesem Zweck die polyzyklischen aromatischen Kohlenwasserstoffe *Picen*, *Pentacen* und *Coronen*. Berichte über außerordentliche Eigenschaften wie Supraleitung und elektronische Korrelationen in Alkalimetall-dotierten Verbindungen der genannten organischen Halbleiter liefern die Motivation für diese Arbeit.
Die elektronische Struktur sowohl der reinen Filme als auch ihrer dotierten Verbindungen wurde unter Verwendung von Photoelektronenspektroskopie untersucht. Rumpfniveau- und Valenzband-Spektren der reinen Filme spiegeln deren hohe Qualität wider. Die Dotierung mit Alkalimetallen äußert sich für die drei untersuchten Probensysteme auf eine überraschend einheitliche Art und Weise in der elektronischen Struktur: In Diskrepanz zu Berichten aus der Literatur über Metallizität oder gar Supraleitung in Alkalimetall-dotiertem Picen, Pentacen und Coronen zeigen *alle* Filme isolierendes Verhalten mit einer Energielücke in der Größenordnung von einem Elektronenvolt. Dieses Verhalten tritt unabhängig von der Dotierkonzentration und der Art des Donators (Kalium, Cäsium oder Natrium) auf. Basierend auf dem Zusammenspiel schmaler Bandbreiten in organischen Halbleitern und hoher Coulomb-Abstoßung der Elektronen auf den Molekülen wird die beobachtete Nicht-Metallizität dem starken Einfluss elektronischer Korrelationen zugeschrieben. Im Fall von Picen wird diese Annahme durch theoretische Betrachtungen bekräftigt, wobei Rechnungen im Rahmen einer Kombination aus Dichtefunktionaltheorie und dynamischer Molekularfeldtheorie durchgeführt wurden.
Neben den Ausführungen hinsichtlich elektronischer Korrelationen werden in dieser Arbeit weitere interessante Beobachtungen adressiert. So hat das Wachstum dünner Picen-Filme die Entstehung eines Nicht-Gleichgewichts zwischen Substrat und Filmoberfläche zur Folge: Auf Grund der nur schwachen van der Waals-Wechselwirkung zwischen den Molekülagen der Filme wird die Ausbildung eines homogenen chemischen Potentials erschwert. Dies führt zu der unerwarteten Beobachtung von spektralem Gewicht oberhalb des chemischen Potentials des Referenzsystems. Des Weiteren konnte gefunden werden, dass die Akzeptanz zusätzlicher Elektronen in Pentacen limitiert ist. Während Picen und Coronen in der Lage sind, bis zu *drei* weitere Elektronen aufzunehmen, ist die entsprechende Grenze bei Pentacen schon für *ein* Elektron erreicht.
Abschließend wurden weitere extrinsische Effekte aufgeklärt, die im Zusammenhang mit der Alkalimetall-Dotierung auftraten. Zum einen führt die Reaktion von Kalium-Atomen mit molekularem Sauerstoff im Restgas der Ultrahochvakuum-Apparatur zur Bildung von Kaliumoxid. Dies äußert sich deutlich in der elektronischen Struktur von Alkalimetall-dotiertem Picen und Coronen. Des Weiteren zeigte hier die verwendete Röntgen- sowie UV-Strahlung deutliche Auswirkungen auf die Photoemissionsspektren. Beide Effekte spielten im Fall der Studien an Pentacen keine Rolle.

Abstract

The present thesis is concerned with the impact of alkali metal-doping on the electronic structure of semiconducting organic thin films. The organic molecular systems which have been studied are the polycyclic aromatic hydrocarbons *picene*, *pentacene*, and *coronene*. Motivated by reports about exceptional behavior like superconductivity and electronic correlations of their alkali metal-doped compounds, high quality films fabricated from the above named molecules have been studied.
The electronic structure of the pristine materials and their doped compounds has been investigated using photoelectron spectroscopy. Core level and valence band studies of undoped films yield excellent photoemission spectra agreeing with or even outperforming previously reported data from the literature. Alkali metal-doping manifests itself in a uniform manner in the electronic structure for all probed samples: Opposed to reports from the literature about metallicity and even superconductivity in alkali metal-doped picene, pentacene, and coronene, all films exhibit insulating nature with an energy gap of the order of one electron-volt. Remarkably, this is independent of the doping concentration and the type of dopant, i.e., potassium, cesium, or sodium. Based on the interplay between narrow bandwidths in organic semiconductors and sufficiently high on-molecule Coulomb repulsion, the non-metallicity is attributed to the strong influence of electronic correlations leading to the formation of a Mott insulator. In the case of picene, this is consolidated by calculations using a combination of density functional theory and dynamical mean-field theory.
Beyond the extensive considerations regarding electronic correlations, further intriguing aspects have been observed. The deposition of thin picene films leads to the formation of a non-equilibrium situation between substrate and film surface. Here, the establishment of a homogeneous chemical potential is hampered due to the only weak van der Waals-interactions between the molecular layers in the films. Consequently, spectral weight is measurable *above* the reference chemical potential in photoemission. Furthermore, it has been found that the acceptance of additional electrons in pentacene is limited. While picene and coronene are able to host up to *three* extra electrons, in pentacene the limit is already reached for *one* electron.
Finally, further extrinsic effects, coming along with alkali metal-doping, have been scrutinized. The oxidation of potassium atoms induced by the reaction with molecular oxygen in the residual gas of the ultra-high vacuum system turned out to significantly influence the electronic structure of alkali metal-doped picene and coronene. Moreover, also the applied X-ray and UV irradiation caused a certain impact on the photoemission spectra. Surprisingly, both effects did not play a role in the studies of potassium-doped pentacene.

Contents

List of Figures

List of acronyms

AFM	atomic force microscopy
ARPES	angle-resolved photoelectron spectroscopy
BC-MIT	bandwidth-controlled metal-to-insulator transition
DFT	density functional theory
DMFT	dynamical mean-field theory
DOS	density of states
EELS	electron energy loss spectroscopy
ESCA	electron spectroscopy for chemical analysis
FC-MIT	filling-controlled metal-to-insulator transition
FPLO	full potential local orbital
FWHM	full width at half maximum
GGA	generalized gradient approximation
HAXPES	hard X-ray photoelectron spectroscopy
HOMO	highest occupied molecular orbital
IMFP	inelastic mean free path
LDA	local density approximation
LEED	low energy electron diffraction
LHB	lower Hubbard band
LUMO	lowest unoccupied molecular orbital
OME	organic molecular effusion
PAH	polycyclic aromatic hydrocarbon
PEEM	photoemission electron microscopy
PES	photoelectron spectroscopy
QCM	quartz crystal microbalance
RPA	random phase approximation
SPV	surface photovoltage
UHB	upper Hubbard band
UHV	ultrahigh vacuum

UPS	ultraviolet photoelectron spectroscopy
UV	ultraviolet
VASP	Vienna *ab initio* simulation package
VT-SPM	variable temperature scanning probe microscope
XAS	X-ray absorption spectroscopy
XPS	X-ray photoelectron spectroscopy
XRD	X-ray diffraction

1 Introduction

Carbon forms the key component for life on earth. Most molecules and compounds mainly consisting of carbon are thus summarized in the class of *organic* substances (well-known exceptions are the *inorganics* diamond, graphite, and graphene). The dedicated scientific discipline dealing with these materials is organic chemistry. However, the task of organic chemistry is the analysis of substances and their reactions on a macroscopic scale. The interest in more profound properties of a substances' basic constituents on a microscopic, atomic scale creates the link to *physics*. Quantum physics provides access to, e.g., the atomic and electronic structure of organic molecules as well as single crystals and thin films fabricated thereof. In this way, a deeper understanding of composition, behavior and properties can be gained, which allows finding, understanding and controlling the fascinating nature of a manifold of materials. Exploiting the intriguing physical properties of organic molecules nowadays sets the focus essentially on their application in future electronics [1, 2]. Most attractive features are the flexibility of organic devices [3] and the practical ability of being printed [4], leading to the development of, e.g., new innovative kinds of displays.

Besides the efforts in applied physics, organic compounds are also a debated topic in basic research. In particular, the remarkable property of becoming superconducting attracts considerable attention to many organic materials. Since the discovery of superconductivity in layered organic charge transfer salts in the late 1970s [5], a large variety of organic superconductors have been reported with critical temperatures ranging from a few Kelvins to values as high as 38 K in the case of alkali metal-doped fullerenes [6]. Recently, a new 'family' of organic molecules, viz., the polycyclic aromatic hydrocarbons, joined this 'illustrious community' of organic superconductors. Upon intercalation with alkali metal or alkaline earth metal atoms, powder samples of the aromatic molecules picene, phenanthrene, coronene, and dibenzopentacene have been reported to exhibit a pronounced Meissner-Ochsenfeld effect below impressive transition temperatures as high as 30 K [7–11]. For potassium-intercalated picene, additionally, a second characteristic feature of superconductivity has been claimed by the observation of zero resistivity below the critical temperature [12]. It is noteworthy that in each case the occurrence of superconductivity is achieved by intercalation with either *three* alkali metal atoms or *1.5* alkaline earth metal atoms per molecule. Both imply doping with *three* electrons. Whether superconductivity is driven by electron-phonon interactions or by electronic correlations has been a subject of intense debate in the last decade, and indeed a significant fraction of organic systems are presently being discussed as correlated materials [13, 14]. Consequently, the issue of electronic correlations also plays a role in

the context of aromatic molecules. In 2009, a Mott metal-to-insulator transition has been reported for potassium-intercalated pentacene based on conductivity measurements [15]. Insulating behavior has been found despite a half-filled conduction band. This is the basic characteristic of a Mott insulator. Moreover, non-metallicity has also been observed in photoemission for a vast zoo of semiconducting organic molecular systems intercalated with alkali metals, manifested by a clear gap in the photoemission spectra. Here, the copper phthalocyanines, Alq_3, and PTCDA are only a few examples [16–26]. Besides an interpretation in terms of polaronic effects, again electronic correlations have been taken into consideration.
Setting out to fully characterize the properties of pristine and doped organic compounds, the configuration of the *electronic structure* is of general interest. Hence, the impact of potassium-doping on the electronic structures of three selected aromatic hydrocarbons, namely *picene*, *pentacene*, and *coronene* (all semiconductors), has been studied within this thesis. Thin films fabricated from the respective molecules have been comprehensively investigated by means of photoelectron spectroscopy. Furthermore, the results for picene have been compared to calculations from a combination of density functional theory and dynamical mean-field theory.

Outline of the Thesis

The present dissertation is structured as follows. Chapter 2 deals with the theoretical approach to the physics of electronic correlations. After a phenomenological entry into Mott physics, the one-dimensional Hubbard model is introduced. Furthermore, a little insight into the theoretical methods of density functional theory and dynamical mean-field theory is given. The basic principles of the mainly applied technique, photoelectron spectroscopy, are depicted in Chap. 3. Moreover, the relevant quantitative aspects used in the course of this thesis are described there. In the main part the organic materials under investigation and the corresponding results are presented. Chapters 4, 5, and 6 report about picene, pentacene, and coronene, respectively, as well as their alkali metal-doped compounds. Finally, a short summary is given in Chap. 7.

Remarks

Two important remarks, which have to be kept in mind, shall be made at this point.
(1) In this thesis, the term Fermi level (E_F) will appear several times. Although, strictly speaking, the Fermi level is only defined for T=0, this notation will be used conterminously with 'chemical potential'. In the context of photoemission experiments, this is a common practice.
(2) Doping is generally achieved by alkali metal-intercalation. Doping concentrations, x, quantified in this thesis always mean concentrations of intercalated alkali metal atoms. This has to be distinguished from the actual concentration of electrons donated to the conduction band.

2 Theoretical approach to Mott physics

For the majority of existing materials it is sufficient to consider the electrons in the solid as non-interacting particles in order to describe the electronic structure. These electrons reside in energy bands in k-space which are formed due to the orbital overlap of adjacent atoms in real space. In this non-interacting particle picture mainly two scenarios can occur depending on the filling of the bands at the Fermi level. On the one hand, the bands can be partially filled, i.e., the solid is a metal. On the other hand, the bands can be completely filled resulting in an insulator. One distinguishes between a real insulator having a large band gap ($> 2\,\mathrm{eV}$) and a semiconductor displaying a small band gap ($< 2\,\mathrm{eV}$) [27]. Transitions between metallic and insulating states are easily achieved by varying the band filling via electron or hole-doping. If structural modifications are absent, the different fillings typically manifest themselves in rigid shifts of the electronic band structure with respect to the chemical potential. By applying physical or chemical pressure or by causing structural changes, deviations from such a rigid band behavior can occur without affecting the non-interacting character of the electrons.

However, for many materials the simple conception introduced above reaches its limits. Already in the early days of experimental solid state physics, samples exhibiting insulating behavior despite half band filling have been observed. The following sections will address the physics behind such deviations from a non-interacting particle picture.

2.1 Mott physics

The profound principle causing deviations from a nearly-free electron picture is the mutual repulsion between two negatively charged electrons. It was already realized in the 1930s that the insulating behavior of some materials, although having partially filled outer shells, has to be ascribed to electron-electron interactions [28, 29]. The most prominent example is NiO but also various other materials with partially filled d and f shells (particularly transition metals and their oxides and rare earth compounds, respectively) exhibit such unusual behavior [30]. Based on a *gedanken experiment* by N. F. Mott [31], the underlying fundamentals can be phenomenologically described with the help of Fig. 2.1. Imagine a square lattice with lattice constant a. Every site shall be singly occupied with an electron represented by the spin in Fig. 2.1. The spin orientation (up or down) is arbitrarily distributed.

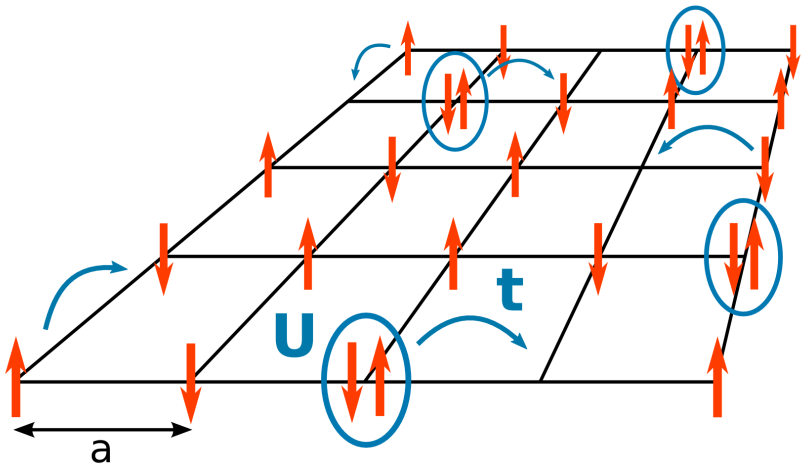

Figure 2.1: *(a) Sketch of a square lattice with singly occupied sites separated by the lattice constant a. Electrons are represented by the spins with arbitrarily distributed orientation. Hopping between two sites is determined by the hopping parameter t, the on-site Coulomb repulsion between two electrons is denoted by U.*

Now, two mechanisms are of importance:

(1) An electron can move to a neighboring empty or singly occupied site, described by the hopping parameter t. This process is associated with an energy gain.

(2) The formation of a doubly occupied site implies that the electrons experience their mutual Coulomb repulsion. Thus, double occupation means an energy cost of U.

Note that the spin orientation plays an important role in the hopping process which will be addressed at the end of Chap. 2.2. In the original *gedanken experiment* Mott increased the lattice constant a, moving from a metallic solid with itinerant electrons – which is due to the band formation by orbital overlap – to an insulating arrangement of single atoms with localized electrons. In a solid the same effect, i.e., the transition from itinerant to localized electrons, can be achieved by the appropriate choice of U and t. Thus, by continuously varying U/t, the system passes a metal-to-insulator transition. If the Coulomb repulsion is small compared to the hopping parameter, $U/t \ll 1$, the solid is a metal. For the other extreme, $U/t \gg 1$, where electron-electron interaction is large, one obtains an insulator, commonly termed Mott insulator. $U/t \gtrsim 1$ represents a special range describing a so-called correlated metal. With this, Mott found an easy, phenomenological way to explain the insulating nature of materials with partially filled outer shells. Beyond this description, the physics of electron-electron interaction will be addressed more thoroughly from a theoretical view in the following.

2.2 The Hubbard model

The most simple model describing systems with strong electron-electron interactions is the Hubbard model [32–34]. Note that, if the electron-electron interactions are strong and cannot be described within Hartree-Fock, they are commonly referred to as electronic correlations. Two assumptions are made which are that all interactions are purely local as well as that only a single (half-filled) band is involved. Since in many Mott insulators indeed only one or few bands cross the Fermi level and participate in low-energy excitations, the Hubbard model is very powerful in describing their effective low-energy and low-temperature properties despite the simplifications mentioned above. In the second quantization formalism the Hubbard Hamiltonian can be written as [32]

$$H_{Hubbard} = \mathcal{T} + \mathcal{U} = -t \sum_{\langle ij \rangle, \sigma} \left(c^{\dagger}_{i\sigma} c_{j\sigma} + c^{\dagger}_{j\sigma} c_{i\sigma} \right) + U \sum_{i} n_{i\uparrow} n_{i\downarrow} \, , \tag{2.1}$$

where the indices i, j denote lattice sites, $\langle ij \rangle$ terms the summation over nearest neighbors only (avoiding double counting), and $\sigma = \uparrow, \downarrow$ represents the spin. The operator $c^{\dagger}_{i\sigma}$ creates an electron with spin σ in a Wannier state $\phi(\boldsymbol{r} - \boldsymbol{R}_i)$[1] at the lattice site i, whereas $c_{i\sigma}$ is the corresponding destruction operator. Furthermore, $n_{i\sigma} = c^{\dagger}_{i\sigma} c_{i\sigma}$ is the number operator. The Hubbard Hamiltonian in Eq. 2.1 is characterized by the competition of its two parts, the kinetic energy term, $\mathcal{T}$, and the interaction term, $\mathcal{U}$. They contain the relevant parameters (see Chap. 2.1), which are the band filling n, the hopping integral t, and the Coulomb repulsion U, commonly referred to as Hubbard U. Regarding the kinetic part $\mathcal{T}$, it is convenient to switch to momentum space since $\mathcal{T}$ is diagonal in *momentum space* when expressed in terms of Bloch waves. The corresponding $\mathcal{T}$ can be obtained by Fourier transformation, resulting in

$$\mathcal{T} = \sum_{\boldsymbol{k}, \sigma} \varepsilon_{\boldsymbol{k}} n_{\boldsymbol{k}, \sigma} \, , \tag{2.2}$$

where $\varepsilon_{\boldsymbol{k}}$ is the $\boldsymbol{k}$-dependent band energy. In a D-dimensional cubic lattice with lattice constant a (see Fig. 2.1), the band energy is represented by the tight binding energy

$$\varepsilon(\boldsymbol{k}) = -2t \sum_{j=1}^{D} \cos k_j a \, . \tag{2.3}$$

From the tight binding approach the bandwidth, W, is known to be connected with the hopping integral via $W = 4Dt$. If a different form of the band energy $\varepsilon_{\boldsymbol{k}}$ is available from, e.g., band structure calculations, it has to be projected onto a tight binding form by downfolding before it can be applied to the Hubbard model.

[1] Wannier orbitals, $\phi(\boldsymbol{r} - \boldsymbol{R}_i)$, are used as wave functions in order to correctly describe the desired locality of the involved interactions. Note that Wannier orbitals are no real atomic but rather fictive orbitals. Basically, they can be expressed in terms of a linear combination of an orthogonal Bloch wave basis.

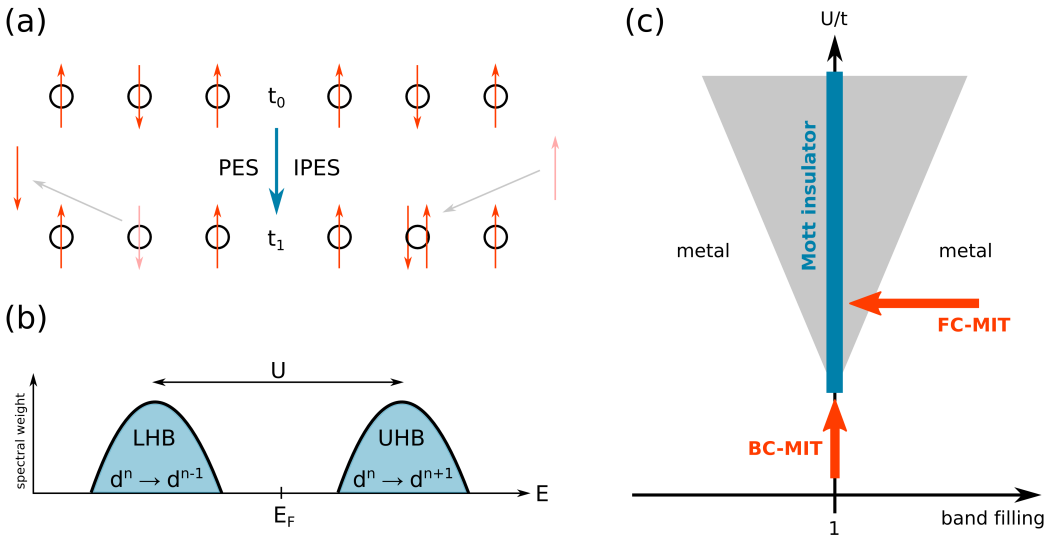

Figure 2.2: *(a) Sketch of the processes in photoemission (PES) and inverse photoemission (IPES) leading to the formation of a lower Hubbard band (LHB) and a upper Hubbard band (UHB). (b) Representation of the electron removal and electron addition spectral function containing LHB and UHB. The peak maxima are separated by the Hubbard U. (c) Schematic phase diagram of the Hubbard model (U/t versus the band filling). The Mott-insulating region (marked in blue) occurs at half filling (n=1). Depicted by the red arrows are the paths of bandwidth-controlled MIT and filling-controlled MIT, respectively.*

In contrast to the kinetic part, the interaction term $\mathcal{U}$ is diagonal in *real space* applying the Wannier orbital description. It accounts for the interaction of electrons sharing the same Wannier orbital due to the Coulomb repulsion. The interaction parameter U is defined as

$$U = \int d\boldsymbol{r}_1 d\boldsymbol{r}_2 \left|\phi(\boldsymbol{r}_1 - \boldsymbol{R}_i)\right|^2 \frac{e^2}{|\boldsymbol{r}_1 - \boldsymbol{r}_2|} \left|\phi(\boldsymbol{r}_2 - \boldsymbol{R}_i)\right|^2 \ . \tag{2.4}$$

Additionally, the Hubbard U can be derived in a more descriptive way considering an electron removal or electron addition experiment, viz., photoemission (PES) or inverse photoemission (IPES). Such an experiment represents the energy difference between removing an electron from a singly occupied site and adding an electron to such a site. U thus reads [32]

$$U(d^n) = E(d^{n-1}) + E(d^{n+1}) - 2E(d^n) \tag{2.5}$$

with $n \geq 1$ (where $n = 1$ means half filling). The situation is illustrated in Fig. 2.2 (a) by the removal and the addition of an electron in the processes of PES and IPES, respectively. Figure 2.2 (b) sketches the resulting spectrum. At this point it is necessary to emphasize that in systems with strongly interacting electrons the density of states (DOS) loses its significance. While in non-interacting systems the DOS reasonably

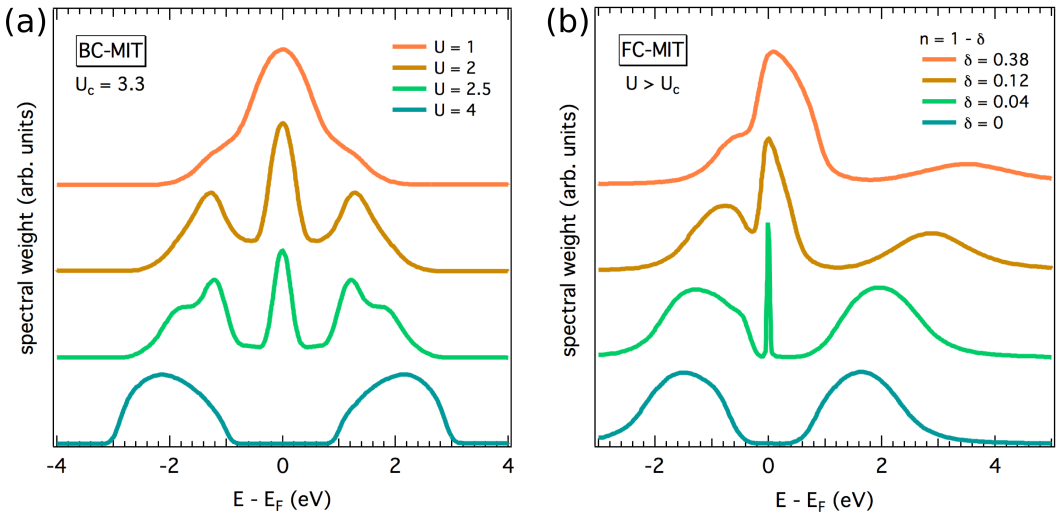

Figure 2.3: *Spectral functions from DMFT for several steps of a metal-to-insulator transition. (a) BC-MIT for varying U. The critical parameter is $U_c \simeq 3.3$. Data from Ref. 35. (b) FC-MIT for different band fillings $n = 1 - \delta$ above U_c ($U = 3.2$ and $U_c \simeq 2.94$). Data taken from R. Bulla [36]. In both cases U is given in the units of $W/2$ with W being the bandwidth.*

describes the energy-dependent occupation of states, this is not valid any longer in interacting systems. In order to correctly reproduce the particle removal or addition spectrum of an interacting system, one has to switch to the spectral function, $A(\boldsymbol{k}, E)$ (see also Chap. 3.1). The spectral function in Fig. 2.2 (b) consists of two 'bands' which are related to the electron removal and addition, respectively. These are named lower Hubbard band (LHB) and upper Hubbard band (UHB) with their maxima separated by the Hubbard U. Opposed to *coherent* quasiparticle bands, they are denoted *incoherent*, explicitly expressing their correlated, local nature (see also Chap. 3.1). Note that the LHB and the UHB are not semiconductor-like bands as known from band theory. As the existence of the UHB, e.g., depends on the population of the LHB, they are no independent bands. In fact, their origin is purely of correlated nature.

Turning back to Mott's original intention of explaining metal-to-insulator transitions (MIT) by the competition between hopping integral t and Coulomb repulsion U now allows the following considerations. In principle, there are two ways to achieve such a MIT: Either one can modify the interaction strength, $U/t \propto U/W$, by changing the bandwidth, e.g., by applying (chemical) pressure. Or one can vary the band filling n away from (or approaching) half filling. The different paths, describing a bandwidth-controlled (BC) and a filling-controlled (FC) MIT, respectively, are indicated by the red arrows in the schematic phase diagram (U/t vs. n) in Fig. 2.2 (c). The Mott insulating phase is restricted to the line of half filling, indicated by the blue mark. Far away from the Mott phase the system is a metal. Furthermore, the gray-shaded region indicates a fluctuation regime where an intermixing of metallic and insulating phases occurs.

In order to follow the evolution of the spectral function by traversing a BC-MIT or a FC-MIT, a powerful calculational method is dynamical mean-field theory (DMFT, see Chap. 2.3.2). Regarding a BC-MIT, corresponding results from Ref. 35 are plotted in Fig. 2.3 (a). The lowest curve represents the Mott insulating state with the incoherent Hubbard bands separated by U. Lowering the correlation strengths U/W leads to the formation of a coherent quasiparticle peak as soon as the correlation strength has dropped below a certain critical value (described by U_c). Here, spectral weight is transferred from the Hubbard bands to the quasiparticle peak. A further decrease of U/W results in a broadening of the quasiparticle peak concomitant with the convergence of LHB and UHB.

For comparison, the evolution of the spectral function from DMFT for the case of a FC-MIT is shown in Fig. 2.3 (b) according to results from R. Bulla [36]. The metallic state is reached via hole-doping, $n = 1 - \delta$. Again the lowest curve depicts the Mott insulating state. Hole-doping is accompanied by the emergence of a quasiparticle peak getting broader for larger δ. Moreover, a shift of the chemical potential is observed. Regarding the FC-MIT, the changes in the Hubbard bands as well as the behavior of the quasiparticle peak appear asymmetric due to the broken electron-hole symmetry.

Concluding this section, a final remark about magnetic properties included in the Hubbard model shall be made. Since double occupation is only allowed for electrons with opposite spin, hopping between two sites will only occur if the spins of neighboring electrons are aligned antiferromagnetically. This implies that an antiferromagnetic coupling is energetically favored in Mott-Hubbard like systems. However, the actual ground state is not *per se* a Néel state. For the limit of high correlations, $U \gg t$, one can rather derive an antiferromagnetic Heisenberg spin Hamiltonian to describe the low-lying excitations [27]. Here, the exchange constant is $J = 4t^2/U$.

2.3 Computational methods

As mentioned in the previous section, dynamical mean-field theory (DMFT) is a powerful calculational method for describing the electronic properties of materials with strongly interacting particles. Using the Hubbard model as an ansatz, the kinetic part in the Hubbard Hamiltonian is usually gained from further calculational methods. One of the most prominent techniques is density functional theory (DFT). A combination of both (DFT+DMFT) has been used for calculations which are part of this thesis. Hence, a short introduction into DFT as well as DMFT will be given in the following.

2.3.1 Density functional theory

Density functional theory facilitates the calculation of, e.g., the total energy of an N electron system. Its major benefit is the ability to compute this energy without requiring an analytical solution of the N particle problem. Instead, the basic quantity of DFT is

the charge carrier density, $n(\boldsymbol{r})$, with a defined spatial dependence. Using a variational principle, the ground state density, $n_0(\boldsymbol{r})$, is calculated. Moreover, from the resulting $n_0(\boldsymbol{r})$ principally all ground state properties of the N electron system can be gained. The basis of density functional theory are the Hohenberg-Kohn theorems [37]:

(1) A universal functional for the energy $E[n(\boldsymbol{r})]$ can be defined in terms of the charge carrier density.

(2) The exact ground state is the global minimum value of the functional $E[n(\boldsymbol{r})]$.

In brief, the message of the theorems is that the ground state energy is given by a functional of the ground state density, $E_0 = E[n_0]$. For any different density the energy is higher, $E[n \neq n_0] \geq E_0$. Note that particle number conservation, $N = \int n(\boldsymbol{r}) d\boldsymbol{r}$, always has to be fulfilled. In the following, the description of the basics of DFT is mainly based on Kotliar *et al.* [38]. The total energy can be written as:

$$E[n(\boldsymbol{r})] = T[n(\boldsymbol{r})] + \int V_{ext}(\boldsymbol{r}) n(\boldsymbol{r}) d^3\boldsymbol{r} + \frac{1}{2} \int \frac{n(\boldsymbol{r}) n(\boldsymbol{r'})}{|\boldsymbol{r} - \boldsymbol{r'}|} d^3\boldsymbol{r} d^3\boldsymbol{r'} + E_{xc}[n(\boldsymbol{r})] \quad (2.6)$$

$$= E_{kin}[n(\boldsymbol{r})] + E_{ext}[n(\boldsymbol{r})] + E_{Hartree}[n(\boldsymbol{r})] + E_{xc}[n(\boldsymbol{r})] \; . \quad (2.7)$$

Altogether, the equation contains three parts: the kinetic energy of a non-interacting system, $E_{kin} = T$; the potential energy of the electrons in the ionic background V_{ext} as well as the Hartree contribution to the Coulomb interaction between the electrons; and all other contributions included in the exchange and correlation energy, E_{xc}. In the Kohn-Sham formalism $n(\boldsymbol{r})$ is assumed to be the density of non-interacting particles moving in an effective potential, i.e., in a *static* mean field [39]. Based thereon, minimizing Eq. 2.6 by the use of the variational principle leads to the Kohn-Sham equations

$$\left[-\frac{\hbar^2 \nabla^2}{2m} + V_{KS}(\boldsymbol{r}) \right] \psi_i = \varepsilon_i \psi_i \; , \quad (2.8)$$

which have the form of one-particle Schrödinger equations with the effective (Kohn-Sham) potential $V_{KS}(\boldsymbol{r})$. ψ_i represent the one-particle wave functions of electrons in the static mean field. ε_i are Lagrange multipliers to ensure that the wave functions are orthonormal. They can be identified as real one-particle energies. The Kohn-Sham potential can be determined from the self-consistency condition

$$V_{KS}[n(\boldsymbol{r})] = V_{ext}(\boldsymbol{r}) + \int \frac{n(\boldsymbol{r'})}{|\boldsymbol{r} - \boldsymbol{r'}|} d^3\boldsymbol{r'} + \frac{\delta E_{xc}[n(\boldsymbol{r})]}{\delta n(\boldsymbol{r})} \; . \quad (2.9)$$

With Eqs. 2.8 and 2.9 the ground state density can be calculated by

$$n(\boldsymbol{r}) = \sum_i f(\varepsilon_i) |\psi_i(\boldsymbol{r})|^2 \; , \quad (2.10)$$

where $f(\varepsilon_i)$ is the Fermi distribution. Finally, from the ground state density one can determine the ground state energy $E[n(\boldsymbol{r})]$.

Since in the above considerations the exchange and correlation energy term E_{xc} is unknown, certain approximations are necessary. A widely used approach is the local density approximation (LDA) which assumes a locally homogeneous electron gas in order to determine E_{xc} [37, 39]. Although this is a very rough approximation, the results from LDA are able to correctly reproduce the ground state energies of various materials. A more exact approach is the generalized gradient approximation (GGA) [40]. It also accounts for local density fluctuations by including the derivative of the density in the determination of E_{xc}. GGA has been used in the calculations which will be presented later in this thesis.

2.3.2 Dynamical mean-field theory

While DFT is a well-established method for the calculation of, e.g., ground state total energies of systems with weakly interacting electrons, further efforts are necessary to correctly describe systems where electron-electron interactions play a crucial role. A powerful tool is dynamical mean-field theory (DMFT), a non-perturbative approach for the treatment of local interactions of electrons, originally developed by Metzner and Vollhardt [41]. Its great advantage is the access to the intermediate range of electronic correlations between the two extreme cases of independent and fully localized electrons. The following introduction into the basics of DMFT is mainly based on Kotliar *et al.* [38]. In general, a mean field theory reduces a many-body lattice problem to a single-site problem with effective parameters. Here, one imagines a local single atom existing in a bath of electrons which can interact with the single atom. Electrons can hop from the bath to the atom and vice versa. Taking the Hubbard model as many-body lattice model, four situations can occur. The local site is empty, it is singly occupied with either spin up or spin down, or it is doubly occupied. All interactions between site and bath are described by the hybridization $V_{\boldsymbol{k}}$ which contains the information given by t and U in the Hubbard model. The quantum impurity model which implements the transition from the Hubbard lattice model to a single-site problem is the Anderson impurity model (AIM). This model yields the exact local Green's function in DMFT if $V_{\boldsymbol{k}}$ fulfills a self-consistency condition. The Green's function describes the probability to create an electron with spin σ ($\uparrow$ or $\downarrow$) at a site i at time τ' and destroy it at the same site at a later time τ.[1] In the AIM, the Hamiltonian reads

$$H_{\mathrm{AIM}} = H_{\mathrm{atom}} + \sum_{\boldsymbol{k},\sigma} \varepsilon_{\boldsymbol{k}}^{\mathrm{bath}} n_{\boldsymbol{k},\sigma}^{\mathrm{bath}} + \sum_{\boldsymbol{k},\sigma} (V_{\boldsymbol{k}} c_{0,\sigma}^{\dagger} a_{\boldsymbol{k},\sigma}^{\mathrm{bath}} + h.c.) \,, \tag{2.11}$$

where H_{atom} describes the single lattice site and $\varepsilon_{\boldsymbol{k}}^{\mathrm{bath}}$ includes all remaining degrees of freedom of the electron bath with the number operator $n_{\boldsymbol{k}}^{\mathrm{bath}}$. $c_0^{\dagger}$ and c_0 allow hopping

[1] The Green's function is defined as $G_{i\sigma}(\tau - \tau') \equiv -\langle c_{i\sigma}(\tau) c_{i\sigma}^{\dagger}(\tau') \rangle$.

from and to the bath via the hybridization $V_{\boldsymbol{k}}$ which accounts for the coupling between the atomic (c_0) and the bath electrons ($a^{\text{bath}}_{\boldsymbol{k},\sigma}$); *h.c.* means the Hermitian conjugate. The parameters $\varepsilon^{\text{bath}}_{\boldsymbol{k}}$ and $V_{\boldsymbol{k}}$ are connected in the hybridization function

$$\Delta(\omega) = \sum_{\boldsymbol{k}} \frac{|V_{\boldsymbol{k}}|^2}{\omega - \varepsilon^{\text{bath}}_{\boldsymbol{k}}} \ , \tag{2.12}$$

which plays the role of the mean field [42]. The frequency dependence makes it a *dynamic* mean field. Since the electrons described by the bath are the same as on the local lattice site, the relevant self-consistency condition in DMFT is to reproduce the local Green's function from the impurity Green's function by applying an effective mean field (given by $\Delta(\omega)$):

$$G[\Delta(\omega)] = \sum_{\boldsymbol{k}} \frac{1}{\omega - \Sigma[\Delta(\omega)] - t_{\boldsymbol{k}}} \ . \tag{2.13}$$

$\Sigma[\Delta(\omega)]$, the self energy, has the meaning of a frequency-dependent potential and $t_{\boldsymbol{k}}$ is the Fourier transform of the hopping parameter t_{ij} in the solid. The self energy is the basic quantity determined by DMFT. By the aid of $\Sigma[\Delta(\omega)]$ the spectral function can be calculated and directly compared to photoemission spectra. Note that an important approximation has been made regarding the lattice self energy by equating it with the impurity's self energy. Spatial fluctuations of the lattice self energy are neglected, which becomes exact for infinite dimensions. This implies that DMFT results are exact if lattice sites with an infinite number of neighbors are considered.

Furthermore, similar to pure DFT, total energies can be computed by

$$\begin{aligned} E[n(\boldsymbol{r}), G] &= T[n(\boldsymbol{r}), G] + \int V_{ext}(\boldsymbol{r}) n(\boldsymbol{r}) d^3\boldsymbol{r} \\ &+ \frac{1}{2} \int \frac{n(\boldsymbol{r}) n(\boldsymbol{r'})}{|\boldsymbol{r} - \boldsymbol{r'}|} d^3\boldsymbol{r} d^3\boldsymbol{r'} + E_{xc}[n(\boldsymbol{r}), G] \ . \end{aligned} \tag{2.14}$$

In the case of DMFT, $T[n, G]$ and $E_{xc}[n, G]$ significantly deviate from their representation in DFT due to the dependence on the Green's function. Owing to the inclusion of electronic correlations, DMFT is able to provide an explicit approximation for E_{xc}.

3 Photoelectron spectroscopy

One of the most powerful tools to study the electronic structure of solids, molecules or atoms is photoelectron spectroscopy (PES) [43]. It is nowadays a well-established and widely used method to explore the occupied electronic states of complex solids [44, 45]. Its main advantages compared to other techniques are the ability to quantify element ratios, providing access to a sample's stoichiometry, and the possibility of identifying the chemical environment of elements present in the sample. Furthermore, PES allows a direct mapping of the valence band electronic structure. Note that, considering the investigation of *molecular* solids, an important shortcoming of PES is its destructive influence on the (electronic) structure of the molecules [46, 47]. Within this thesis this aspect will play a crucial role.

In principle, depending on the energy of the excitation source (E_γ), one can roughly distinguish between (soft) X-ray photoelectron spectroscopy (XPS, $100 < E_\gamma < 1500\,\mathrm{eV}$) and ultraviolet photoelectron spectroscopy (UPS, $E_\gamma < 100\,\mathrm{eV}$). Moreover, using excitation energies $E_\gamma > 1500\,\mathrm{eV}$, one commonly speaks of hard X-ray photoelectron spectroscopy (HAXPES). Due to the element-specific nature of the photoelectrons they can be used in electron spectroscopy for chemical analysis (ESCA), revealing, e.g., the composition and stoichiometry of unidentified samples [48]. However, it is important to keep in mind that PES is a very surface sensitive method. In the following, the basic principles of the photoemission process as well as a description of the spectral function and some important aspects of quantitative analysis will be addressed.

3.1 Basic principles

Photoemission spectroscopy is based on the photoelectric effect, describing the ejection of electrons from a sample irradiated with monochromatic light [49]. An electron in a bound state in the sample absorbs a photon and gets excited into a free state in the vacuum. Depending on the excitation energy, the emitted photoelectrons will possess a certain kinetic energy, E_{kin}, which can be associated with the binding energy of the electron in the solid, E_{bind}, using the Einstein equation [50]:

$$E_{\mathrm{kin}} = h\nu - |E_{\mathrm{bind}}| - \Phi. \tag{3.1}$$

Here, $h\nu$ is the energy of the incident light and Φ is the energy difference between the Fermi energy and the vacuum level, representing the work function (typically of the order of a few eV). According to Eq. 3.1, which complies with energy conservation,

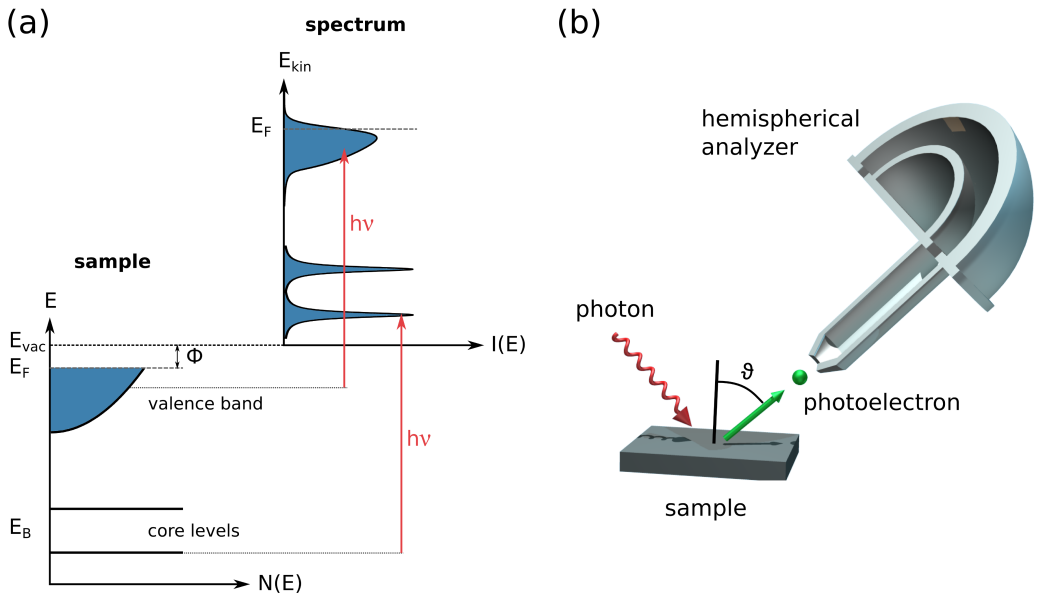

Figure 3.1: *Basics of the photoemission process. (a) Energy schematics in the solid and resulting photoemission spectrum after excitation with light of the energy $h\nu$. (b) Experimental setup. Sketched are the incoming photon and the emitted photoelectron which is collected by a hemispherical photoelectron analyzer. Here, ϑ is the angle between sample surface normal and analyzer.*

the photoemission process is sketched in Fig. 3.1 (a) containing the energetic situation in the sample as well as the resulting photoemission spectrum. The core levels are represented by δ-peaks in the solid where they are located at a defined energy. Due to the finite lifetime of the core holes they correspond to peaks with a finite width in the photoemission spectrum reflected in a Lorentzian peak shape. Besides the lifetime broadening, the core level peaks suffer a resolution broadening expressed by a Gaussian. In total, the core level spectrum is described by a Voigt profile which is generated by the convolution of a Lorentzian and a Gaussian. In most cases the description by a Voigt profile is sufficient. However, depending on the complexity of the investigated system, further line shapes can be involved. One example is the Doniach-Sunjic line shape, accounting for interactions of the photoelectron with the conduction electrons [51]. For an exact treatment more sophisticated theories have to be applied [52]. Turning to the valence band, in a single particle picture the corresponding photoemission spectrum directly reflects the density of states (DOS). Note that this is only valid if matrix-element effects are neglected. The spectrum is cut off by the Fermi function and gets lifetime and resolution broadened. In addition to the considerations in energy phase space, in Fig. 3.1 (b) the real space experimental setup of PES is sketched. It illustrates the incoming photon as well as the ejected photoelectron which is collected by the hemispherical analyzer. The emission angle of the photoelectrons with respect to the

surface normal under which they are detected is denoted ϑ. By varying ϑ at a constant excitation energy, one can gain information about the electronic dispersion $E(\boldsymbol{k})$ of valence band electrons in angle-resolved PES (ARPES).

Depending on the emission angle ϑ, the momentum of an electron in vacuum $\boldsymbol{P} = \hbar\boldsymbol{K}$ parallel and perpendicular to the sample surface can be expressed as

$$\begin{aligned} \hbar\boldsymbol{K}_{\parallel} &= \sqrt{2mE_{kin}}\sin\vartheta \\ \hbar\boldsymbol{K}_{\perp} &= \sqrt{2mE_{kin}}\cos\vartheta \end{aligned} \tag{3.2}$$

where m is the electron mass. In terms of conducting ARPES experiments, $\boldsymbol{K}_{\parallel}$ and $\boldsymbol{K}_{\perp}$ given in Eq. 3.2 are the relevant momenta. In order to learn about the electron momentum in the solid $\boldsymbol{p} = \hbar\boldsymbol{k}$ from the momentum in vacuum, both momenta have to be brought into relation. Since for excitation energies $< 100\,\mathrm{eV}$ the photon momentum can be neglected [53], the electron excitation in the solid corresponds to a vertical transition in a reduced zone scheme with $\boldsymbol{k}_f - \boldsymbol{k}_i = 0$ (f: final state, i: initial state). Note that in a repeated zone scheme the momenta can also differ by an integer multiple of the reciprocal lattice vector $\boldsymbol{G}$ resulting in $\boldsymbol{k}_f - \boldsymbol{k}_i = \boldsymbol{G}$. Considering the transition of the photoelectron from the solid into the vacuum, the momentum parallel to the sample surface is conserved, leading to

$$\hbar\boldsymbol{k}_{\parallel} = \hbar\boldsymbol{K}_{\parallel} = \sqrt{2mE_{kin}}\sin\vartheta. \tag{3.3}$$

On the contrary, this is not the case for the momentum perpendicular to the sample surface. In order to understand this fact in a more descriptive way, one usually splits the photoemission experiment into three distinct and independent processes described in the three-step model [43]. The three involved steps are

(1) the photoexcitation of a bound electron in the bulk,

(2) the transport of the excited electron through the solid to the surface,

(3) and the transition of the photoelectron into the vacuum.

The point of matter is the last step where translational invariance along the surface normal is broken while parallel to the surface it is conserved. Thus, it is advantageous to study one-dimensional and two-dimensional systems by ARPES, since in these cases $\boldsymbol{K}_{\perp}$ can be neglected. Otherwise the change in $\boldsymbol{k}_{\perp}$ has to be taken into account. Since this is not of relevance for the present study, it will not be considered any further.

While the three-step model provides a descriptive way to understand the photoemission process by splitting in into three parts, the one-step model considers the whole process as one part. Its underlying principles will be presented in the following, mainly based on the review article by Damascelli [44]. Usually, the transition rate w between

two states induced by the interaction with a certain perturbation is described by Fermi's Golden rule [43–45], obtained from first-order perturbation theory:

$$w_{fi} = \frac{2\pi}{\hbar} \left| \langle \Psi_f^N | H_{int} | \Psi_i^N \rangle \right|^2 \delta \left(E_f^N - E_i^N - h\nu \right) . \tag{3.4}$$

Here, $E_i^N = E_i^{N-1} - E_{bind}^{\boldsymbol{k}}$ and $E_f^N = E_f^{N-1} + E_{kin}$ represent the energies of the N particle initial and final states Ψ_i^N and Ψ_f^N, respectively, where $i = 0$ defines the ground state. $E_{bind}^{\boldsymbol{k}}$ is the binding energy of an electron with momentum $\boldsymbol{k}$ and $E_{kin} = \hbar^2 \boldsymbol{k}^2 / 2m$ is the kinetic energy of a final state free electron. Moreover, $\langle \Psi_f^N | H_{int} | \Psi_i^N \rangle$ is the N particle transition matrix element. Note that at this point a common simplification comes into play which is the so-called 'sudden approximation'. It assumes that an electron is instantaneously removed from the solid and the effective potential of the system changes discontinuously at that instant. This implies that the created photoelectron does not interact with the $N-1$ particle system. The perturbation included in Eq. 3.4 is represented by the electromagnetic field, $\boldsymbol{A}(\boldsymbol{r}, t)$. It is contained in the perturbation operator H_{int}, given by

$$H_{int} = \frac{e}{2mc} \left(\boldsymbol{A} \cdot \boldsymbol{p} + \boldsymbol{p} \cdot \boldsymbol{A} \right) \approx \frac{e}{mc} \boldsymbol{A} \cdot \boldsymbol{p} \, , \tag{3.5}$$

where $\boldsymbol{p}$ is the electronic momentum operator. Here, two simplifications have been implemented. The quadratic term in $\boldsymbol{A}$ has been dropped, since for the used excitation sources the photon densities are sufficiently low, i.e., two-photon processes can be neglected. Furthermore, the Coulomb gauge, $\nabla \boldsymbol{A} = 0$, has been used, which is fulfilled for small spatial variations of the light wave relative to the atomic scale. Within the sudden approximation, the wave functions of initial and final state can generally be factorized into the wave function of the photoelectron $\varphi^{\boldsymbol{k}}$ and of the remaining $N-1$ particle system. Hence, they can be written as $\Psi_i^N = A \varphi_i^{\boldsymbol{k}} \Psi_i^{N-1}$ and $\Psi_f^N = A \varphi_f^{\boldsymbol{k}} \Psi_f^{N-1}$, where A is an antisymmetric operator accounting for the compliance with Pauli's principle. The final state wave function of the $N-1$ particle system is chosen as an excited state with the eigenfunction Ψ_m^{N-1} and the energy E_m^{N-1} which is no eigenenergy of Ψ_m^{N-1}. In order to obtain the total transition probability, one has to sum over all excited states m. Furthermore, as well-known from the second quantization formalism, the wave function of the $N-1$ particle system can be expressed by the annihilation of one electron in the N particle system using the annihilation operator $c_{\boldsymbol{k}}$:

$$\Psi_i^{N-1} = A c_{\boldsymbol{k}} \Psi_i^N \, . \tag{3.6}$$

Using this, the matrix element from Eq. 3.4 then can be written as

$$\langle \Psi_f^N | H_{int} | \Psi_i^N \rangle = \langle \varphi_f | H_{int} | \varphi_i \rangle \langle \Psi_f^{N-1} | \Psi_i^{N-1} \rangle \, , \tag{3.7}$$

where the first part represents the one electron transition matrix element (commonly in the dipole approximation) and the second term describes the $N-1$ electron overlap

integral. Putting all together, one obtains the total photoemission intensity (depending on $\boldsymbol{k}$ and E_{kin}) by summing w_{fi} over all possible states:

$$I(\boldsymbol{k}, E_{kin}) = \sum_{f,i} w_{fi} \propto \sum_{f,i} \left|M_{fi}^{\boldsymbol{k}}\right|^2 \sum_m |c_{mi}|^2 \, \delta\left(E_{kin} + E_m^{N-1} - E_i^N - h\nu\right), \tag{3.8}$$

with $|c_{mi}|^2 = \left|\langle \Psi_m^{N-1} | \Psi_i^{N-1} \rangle\right|^2$ describing the probability of the $N-1$ particle system resulting in the excited state m upon the removal of an electron from state i. It is convenient to introduce the energy $\epsilon = h\nu - E_{kin}$. Eq. 3.8 can now be rewritten as:

$$\begin{aligned} I(\boldsymbol{k}, E_{kin}) &= \frac{2\pi}{\hbar} \sum_{f,i} \left|M_{fi}^{\boldsymbol{k}}\right|^2 \sum_m \left|\langle \Psi_m^{N-1} | c_i | \Psi_i^N \rangle\right|^2 \delta\left(\epsilon + E_m^{N-1} - E_i^N\right) \\ &= \frac{2\pi}{\hbar} \sum_{f,i} \left|M_{fi}^{\boldsymbol{k}}\right|^2 A^<(\boldsymbol{k}, \epsilon) \, . \end{aligned} \tag{3.9}$$

$A^<(\boldsymbol{k}, \epsilon)$ denotes the one-particle removal spectral function. Particularly for interacting many-body systems it acts as the central quantity to describe electron emission spectra, e.g., in photoelectron spectroscopy. The spectral function is defined by the imaginary part of the one-particle Green's function $G(\boldsymbol{k}, \epsilon)$.[1]

$$\begin{aligned} A^<(\boldsymbol{k}, \epsilon) &= \sum_m \left|\langle \Psi_m^{N-1} | c_i | \Psi_i^N \rangle\right|^2 \delta\left(\epsilon + E_m^{N-1} - E_i^N\right) \\ &= -\frac{1}{\pi} \operatorname{Im} G(\boldsymbol{k}, \epsilon) f(\epsilon, T) \qquad (3.10) \\ G(\boldsymbol{k}, \epsilon) &= \frac{1}{\epsilon - E(\boldsymbol{k}) - \Sigma(\boldsymbol{k}, \epsilon)} \, . \qquad (3.11) \end{aligned}$$

Here, $E(\boldsymbol{k})$ is the electron band dispersion and $\Sigma(\boldsymbol{k}, \epsilon)$ describes the complex self energy which contains all contributions from many-body processes in photoemission (see Chap. 2.3.2), e.g., electron-electron or electron-phonon interaction. While its real part causes a renormalization of the original energy dispersion, the imaginary part includes the finite lifetime of the excitations. Figure 3.2 illustrates how the described behavior is manifested in a photoemission spectrum. Momentum-resolved electron removal and also electron addition spectra are plotted. Regarding the non-interacting case in Fig. 3.2 (a), the self energy vanishes, resulting in a Green's function with a single pole. The spectral function is thus given by a single δ-peak at an energy $E(\boldsymbol{k})$ showing a certain dispersion.

Switching on the interaction, the electrons now have to be considered as so-called quasiparticles (in the Fermi liquid picture), i.e., electrons dressed with a manifold of

[1] The Green's function $G(\boldsymbol{k}, \epsilon)$ is the single-particle propagator.

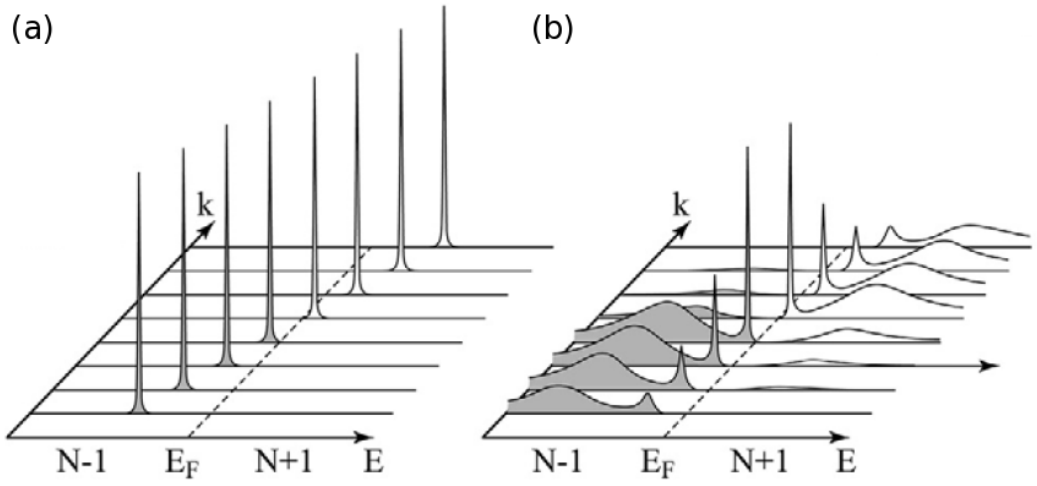

Figure 3.2: *Spectral function of non-interacting and interacting systems. (a) In the non-interacting case the momentum-dependent energy $E(\boldsymbol{k})$ is described by a δ-peak like structure with a certain dispersion. (b) The spectral function of the interacting case consists of an energy-renormalized quasiparticle (coherent) peak and an interaction-induced incoherent structure at a different energy. Figure reprinted from Ref. 44 with permission from A. Damascelli. Copyright (2013) by The American Physical Society.*

excited states. As for the non-interacting system, the excited states are characterized by poles of the Green's function, now with renormalized energy and mass as well as a finite lifetime. This leads to *coherent* peaks which are located at a different energy and exhibit a larger width compared to the non-interacting case. Additionally, *incoherent* spectral weight is found at higher binding energies which can completely be ascribed to the interactions of the particles in the system. This illustrates the characteristic behavior of systems with interacting particles playing a crucial role in this thesis.

3.2 Quantitative aspects

After the short introduction into the basic principles of photoemission, the present section deals with quantitative aspects which will be needed and used later in this thesis. Therefore, shortly the methods XPS, UPS, and PEEM will be introduced. Furthermore, details about relevant corrections, viz., background and satellite corrections, of the recorded photoemission spectra as well as the possibility to use PES for chemical analysis in terms of ESCA will be addressed.

3.2.1 Experimental methods

X-ray photoelectron spectroscopy (XPS)

Photoemission measurements involving the excitation with X-rays have been conducted in the home-laboratory in Würzburg equipped with an Omicron XM1000 X-ray source. Here, the Al K_α radiation is used, monochromatized by a crystal monochromator. The resulting excitation energy is $h\nu = 1486.6\,\mathrm{eV}$ with a line width of $\Delta h\nu = 0.85\,\mathrm{eV}$. Photoemission spectra have been recorded using an Omicron EA125 hemispherical analyzer. The total energy resolution at room temperature was chosen to be $\Delta E_{\mathrm{RT}} = 0.7\,\mathrm{eV}$. Additional measurements presented in this thesis have been performed at $T = 40\,\mathrm{K}$ with an energy resolution of $\Delta E_{40\mathrm{K}} = 0.3\,\mathrm{eV}$.

Ultraviolet photoelectron spectroscopy (UPS)

For the excitation with UV light a ThermoVGScientific He gas discharge lamp was available emitting non-monochromatized He I radiation with an energy of $h\nu = 21.2\,\mathrm{eV}$. In case of UPS the total energy resolution (using the Omicron EA125 analyzer) was chosen to be $\Delta E_{\mathrm{RT}} = 0.1\,\mathrm{eV}$ at room temperature and $\Delta E_{40\mathrm{K}} = 0.04\,\mathrm{eV}$ at $T = 40\,\mathrm{K}$.

Photoemission electron microscopy (PEEM)

Photoemission electron microscopy experiments have been performed at the beamline UE49-PGM-A-SPEEM at the Berliner Elektronensynchrotron (BESSY) providing radiation generated by an insertion device (undulator). The energy could be varied between 90 and 1800 eV. For data acquisition an Elmitec PEEM equipped with a photoelectron analyzer was used. The spatial resolution of the microscope was $\Delta x \approx 15\,\mathrm{nm}$, the total energy resolution regarding the spectroscopic experiments was $\Delta E = 0.3\,\mathrm{eV}$. All measurements were performed at room temperature.

3.2.2 Relevant corrections

The use of photoemission spectra (mainly from XPS) for a quantitative analysis of the sample under investigation requires the implementation of certain corrections. Inherent to the photoemission process is the generation of secondary (inelastically scattered) electrons. Hence, in order to gain information from, e.g., photoemission peak intensities, the spectra have to be corrected for the secondary electron background. A standard method for this correction, which is used in the course of this thesis, has been developed by D. Shirley [54]. Within this method it is assumed that the background at a certain energy, E, is proportional to the total number of electrons at a higher kinetic energy, $E' > E$. Consequently, the background itself is described by the convolution of a constant loss function with the intrinsic core level spectrum. Regarding the photoemission experiment, the measured intensity of a core level spectrum, $I^{\mathrm{meas}}(E)$, is composed of the intrinsic

core level spectrum, $I(E)$, and the background signal. As shown in Eq. 3.12, $I(E)$ can be determined following an iterative procedure which uses the measured spectrum $I^{\mathrm{meas}}(E)$ as a starting point for the unknown intrinsic spectrum [54]:

$$I^{n+1}(E) = I^{\mathrm{meas}}(E) - I^{n}(\epsilon)\frac{\sum_{E'>E} I^{\mathrm{meas}}(E')}{\sum_{E'>\epsilon} I^{\mathrm{meas}}(E')} \; . \tag{3.12}$$

Here, ϵ represents the limit on the lower kinetic energy side for the iteration. Commonly, only a few iteration steps ($n \sim 5$) suffice to generate well-converged results.

Beside the core level spectra, also for the valence band spectra obtained by UPS the secondary electron background has to be taken into account. According to Ref. 43, this background exhibits a strong increase in the energy range between 0 and -15 eV relative to the chemical potential which can be approximated by an exponential slope towards higher binding energies. Low binding energy features in the spectrum are superimposed to the background. For quantitative analysis of valence band spectra, thus, an exponential background has been subtracted prior to further data evaluation.

A further necessary correction to avoid misinterpretations of valence band spectra is the subtraction of $\mathrm{He\,I}_\beta$ and $\mathrm{He\,I}_\gamma$ satellite contributions to the photoemission spectrum. Considering the emission of a He gas discharge lamp, the main contribution is given by $\mathrm{He\,I}_\alpha$ radiation with $h\nu = 21.2\,\mathrm{eV}$. However, also the $\mathrm{He\,I}_\beta$ and $\mathrm{He\,I}_\gamma$ lines at $h\nu = 23.1\,\mathrm{eV}$ and $h\nu = 23.7\,\mathrm{eV}$ contribute $1.2 - 1.8\,\%$ and $0.5\,\%$ to the spectrum, respectively. In a second order approximation the intrinsic spectrum $I(E)$ is obtained by

$$\begin{aligned} I(E) = I^{\mathrm{meas}}(E) \;&+\; (-1)^1 \left(b \cdot I^{\mathrm{meas}}(E + \Delta E_\beta) + c \cdot I^{\mathrm{meas}}(E + \Delta E_\gamma)\right) \\ &+\; (-1)^2 \left(b^2 \cdot I^{\mathrm{meas}}(E + \Delta E_\beta) + c^2 \cdot I^{\mathrm{meas}}(E + \Delta E_\gamma)\right) \; , \end{aligned} \tag{3.13}$$

where b and c are the above given contributions of $\mathrm{He\,I}_\beta$ and $\mathrm{He\,I}_\gamma$, and $\Delta E_\beta = 1.9\,\mathrm{eV}$ and $\Delta E_\gamma = 2.5\,\mathrm{eV}$ are the energy differences of the satellites to the $\mathrm{He\,I}_\alpha$ main line. In most practical cases, already the first order of the approximation yields adequate results.

3.2.3 Inelastic mean free path

An important intrinsic property of photoelectron spectroscopy, which has to be kept in mind, is its surface sensitivity. It is founded in the small inelastic mean free paths (IMFP), λ_e, of the electrons in the solid. The IMFP represents the distance electrons can travel through the solid before being scattered (mainly) by other electrons. Depending on the electron kinetic energy, it is only of the order of a few nm. Remarkably, the energy dependent electron IMFP follows a universal behavior for the most elements and solids, reflected in the so-called 'universal curve' [55], displayed in Fig. 3.3. The dominant scattering process is the excitation of a plasmon which represents the collective oscillation of the electron gas relative to the cationic background of the solid. The corresponding

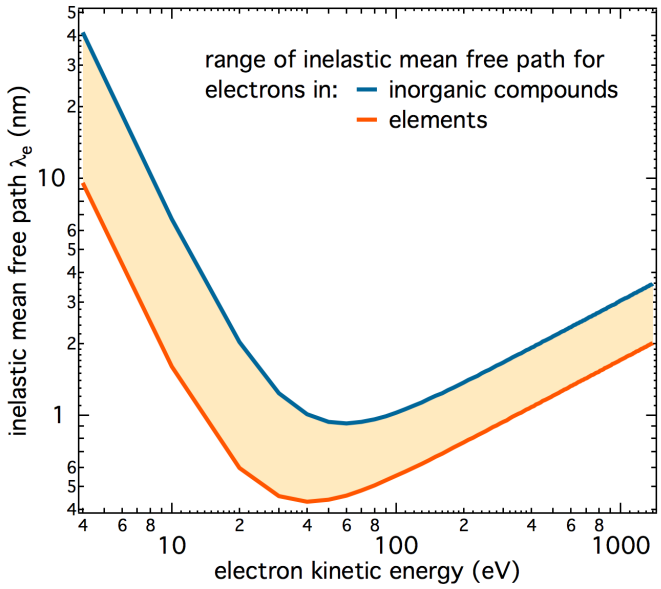

Figure 3.3: *'Universal curve' of the electrons' inelastic mean free path depending on their kinetic energy. Note the $\sqrt{E}$-dependence for energies $> 50\,\mathrm{eV}$. According to Ref. 55.*

energy of the oscillating electron gas, the plasma energy E_p, is proportional to $\sqrt{n}$ (with n being the electron density). n, in turn, shows only marginal variations for different materials, which leads to the observed universal behavior. Regarding typical laboratory light sources as described before (Al K_α, He I), λ_e ranges from $0.1 - 30\,\mathrm{nm}$. While for energies $> 50\,\mathrm{eV}$ the universal curve approximately exhibits a $\sqrt{E}$-dependence, it shows a $E^{-1/2}$ trend for $E < 50\,\mathrm{eV}$.

Since a small IMFP implies that the detected electrons in photoemission only stem from a narrow, surface-near region of the sample, it is crucial to ensure atomically clean surfaces in order to exclude the investigation of only the surface contamination. This fact necessitates an ultra-high vacuum (UHV) environment to perform meaningful photoemission experiments. The investigation of a particular material for which no experimental IMFPs are available calls for the ability to calculate λ_e. While the IMFP cannot be determined from fundamental physical relationships, several empirical approaches exist, which succeed in well reproducing the experimental observations [55–57]. A widely used possibility to calculate λ_e is the empirical equation by Tanuma, Powell, and Penn (TPP-2M) [56, 58]:

$$\lambda_e = \frac{E}{E_p^2 \left[\beta \cdot \ln(\gamma E) - \left(\frac{C}{E}\right) + \left(\frac{D}{E^2}\right)\right]} \,. \tag{3.14}$$

Here, E_p is the plasma energy, β, γ, C, and D are material specific parameters. Necessary input for the calculation of these parameters are the density, the atomic or molecular weight, the number of valence electrons per atom or molecule, and the band-gap energy.

For the case of inorganic solids, the universal behavior from Fig. 3.3 is reproduced by Eq. 3.14. On the contrary, for organic materials the calculated λ_e is significantly larger, due to the comparatively low densities of the organic compounds. To give an example, electrons with $E_{\mathrm{kin}} = 1200\,\mathrm{eV}$ exhibit a λ_e of $3 - 4\,\mathrm{nm}$ in different organics [56]. Nonetheless, the basic energy dependence of Eq. 3.14 is retained.

By the aid of λ_e one can estimate the probing depth for the respective sample under investigation in PES. Assuming exponential damping caused by the scattering processes, the measured photoemission intensity depending on the vertical position in the sample (i.e., regarding the depth) is given by

$$I(z) \propto \exp\left(-\frac{z}{\lambda_e \cos\vartheta}\right), \tag{3.15}$$

where ϑ is the angle between sample surface normal and photoelectron emission again [see Fig. 3.1 (b)]. Defining a particular depth z such that 95% of all emitted photoelectrons stem from the volume between surface and this particular depth reveals the *information depth* $z = 3\lambda_e \cos\vartheta$. From this it becomes obvious that the information depth can be easily varied by either using different excitation energies or changing the angle between sample surface normal and photoelectron analyzer. This procedure represents a widely used technique to perform depth profiling. In order to better compare XPS with corresponding UPS data, valence band measurements have been conducted in normal emission geometry, whereas for core level analysis a photoelectron emission angle of $\vartheta = 50°$ has been chosen. Note that UPS is nonetheless significantly more surface sensitive.

3.2.4 Electron spectroscopy for chemical analysis

Owing to the fact that XPS is a highly element specific technique, it is often used for the identification of a sample's stoichiometry. The possibility to gain quantitative information from XPS is based on the direct proportionality of the background corrected core level intensity from photoemission I and the concentration of the corresponding element within the analyzed sample volume N, $I \propto N$. However, the element's concentration leading to a certain photoemission intensity is renormalized by several parameters. Depending on the specific element, primarily one has to take into account the (excitation energy-dependent) photoionization cross-section, $\sigma(h\nu)$. Further input is the asymmetry function, $L(\gamma) = 1 + \frac{1}{2}\beta(h\nu)\left(\frac{3}{2}\sin^2\gamma - 1\right)$, which accounts for the symmetry of the excited atomic orbital involving the (excitation energy-dependent) asymmetry parameter $\beta(h\nu)$ and the angle γ between light source and photoelectron analyzer. These parameters are tabulated, e.g., in Yeh and Lindau [59] or Trzhaskovskaya *et al.* [60]. Furthermore, the photon flux, $J(h\nu)$, of the utilized light source and the angle δ between light source and sample surface normal as well as the above described (angle-dependent) IMFP, $\lambda_e \cos\vartheta$, contribute to the photoemission intensity. Besides, two analyzer specific parameters influence the photoemission intensity, viz., the detector efficiency, D, and the

analyzer transmission function, T. By operating an analyzer in the constant analyzer energy mode, i.e., with a constant pass energy, the detector efficiency is independent of the electron kinetic energy. The transmission function for the employed analyzer EA125 by Omicron has been determined as $T(E) = E^{-1}$ [61]. In total, the photoemission intensity can be written as [62]:

$$I(E) = \sigma(h\nu)L(\gamma) \cdot J(h\nu) \sec\delta \cdot N \cdot \lambda_e(E) \cos\vartheta \cdot D(E)T(E) \; . \tag{3.16}$$

Since the photon flux and the detector efficiency are unknown, it is not possible to determine absolute values for N from the background corrected photoemission intensity. However, relative atomic concentrations of elements A and B can be calculated using the following equation:

$$\frac{N_A}{N_B} = \frac{I_A}{I_B} \frac{\sigma_B(h\nu)L(\gamma_B)\lambda_e(E_B)T(E_B)}{\sigma_A(h\nu)L(\gamma_A)\lambda_e(E_A)T(E_A)} \tag{3.17}$$

$$\simeq \frac{I_A}{I_B} \frac{\sigma_B(h\nu)L(\gamma_B)\sqrt{E_A}}{\sigma_A(h\nu)L(\gamma_A)\sqrt{E_B}} \; . \tag{3.18}$$

In Eq. 3.18, λ_e has been approximated by a $\sqrt{E}$-dependence, leading together with $T(E) = E^{-1}$ to a $E^{-1/2}$-dependence. Since the IMFPs calculated by Eq. 3.14 only show marginal variations from the $\sqrt{E}$-dependence, as in most cases appearing in this thesis, Eq. 3.18 has been used to determine the relative atomic concentrations. The largest error bars in N_A/N_B originate from σ and β, since these values are computed for isolated atoms. Hence, the error bars are estimated to be at least 20 % but may even exceed this value as can be seen in A.3.

4 The supposedly superconducting $K_x$picene

Picene, an 'old' aromatic molecule, was first synthesized in the early fifties [63]. The structural properties of picene *single crystals* have been determined already in the mid-eighties [64]. *Thin films* of picene got renewed interest in 2008/2009 due to reported high charge carrier mobilities in field effect transistors. Remarkably, mobilities up to $1.1\,\mathrm{cm}^2/\mathrm{Vs}$ have been achieved [65–70]. Due to its properties very similar to those of the well-known molecule pentacene, picene can be considered a new promising candidate for replacing silicon-based devices in future electronics. In 2010, picene gained even more attractiveness when Mitsuhashi *et al.* reported a pronounced Meissner-Ochsenfeld effect in polycrystalline samples of $K_{2.9}$picene. They concluded on superconductivity at transition temperatures as high as 18 K [7]. Very recently, Teranishi *et al.* provided further evidence of superconductivity by the observation of zero resistivity in K_3picene pellets below 7 K [12], supporting the observations from Mitsuhashi *et al.* The original findings triggered a multitude of theoretical studies trying to explain the origin of superconductivity in this polycyclic aromatic hydrocarbon. While several groups performed basic density functional theory (DFT) calculations [71–74], other groups focussed on electron-phonon coupling [75–81] as well as electron-electron interaction [82, 83]. Most of the calculations reveal metallic conduction bands for K_3picene which would host the superconductivity below the critical temperature. However, also insulating behavior due to electronic correlations is proposed implying unconventional superconductivity in terms of a correlated metal close to a metal-to-insulator transition. Also from experimental view, the picture of the electronic structure has remained controversial. A photoemission study reported the appearance of metallic spectral weight at the Fermi level for K_1picene [84]. On the contrary, other authors [85, 86] failed to observe a metallic Fermi edge for a wide potassium concentration range from $x = 0.22$ to 3.6 and speculated about the possible role of correlations and polaronic effects [85].

In the following, an extensive photoemission study of $K_x$picene for potassium concentrations of $x = 0 - 3$ is presented, uncovering a series of interesting properties of this supposedly superconducting molecular material. In particular, X-ray photoelectron spectroscopy (XPS) and ultraviolet photoelectron spectroscopy (UPS) for core level and valence band analysis, respectively, have been conducted. Structural quality was checked by atomic force microscopy (AFM) and X-ray diffraction (XRD).

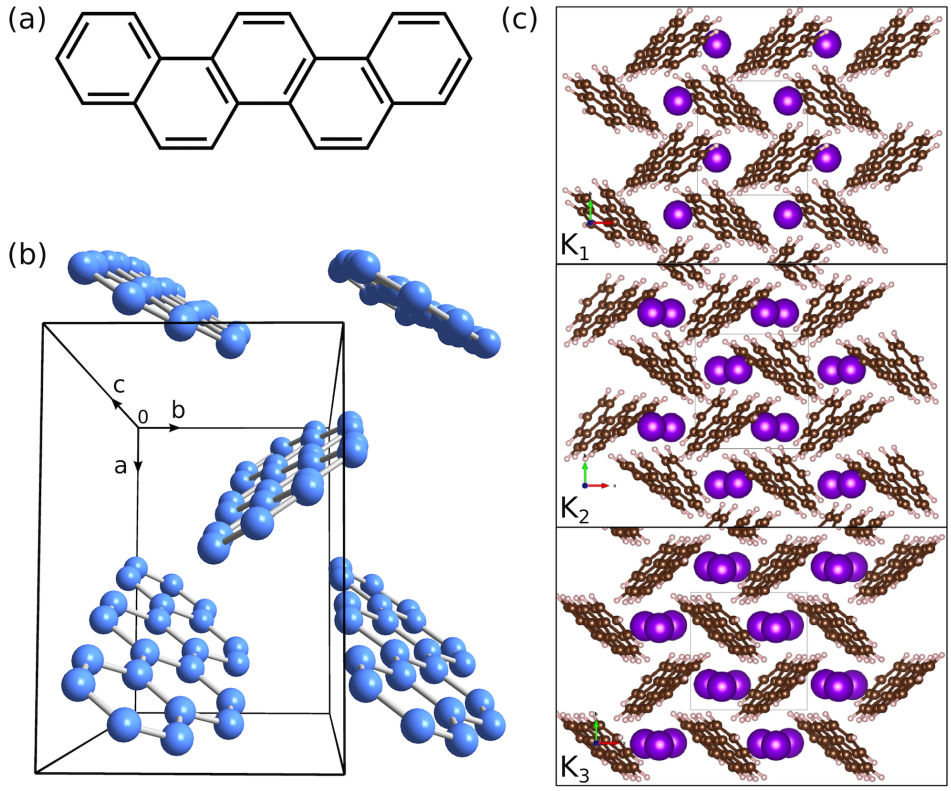

Figure 4.1: *(a) Structural formula of a single picene ($C_{22}H_{14}$) molecule consisting of five benzene rings. (b) Unit cell structure of a pristine picene crystal containing two inequivalent picene molecules. (c) Structure of K-intercalated picene: K_1picene (upper panel), K_2picene (mid panel), and K_3picene (lower panel). Note that the herringbone structure is retained upon dopant atom insertion. Pictures from Jeschke et al. [87].*

4.1 From the parent compound to $K_x$picene

The parent compound picene is a planar, π-conjugated aromatic molecule consisting of five benzene rings arranged in an armchair fashion as sketched in Fig. 4.1 (a). It is often referred to as a cutout of a graphene sheet and thus denominated *nano-graphene*. In the bulk, i.e., in single crystals or thin films, picene crystallizes in a monoclinic structure (space group $P2_1$) with the lattice parameters $a = 8.480\,\text{Å}$, $b = 6.154\,\text{Å}$, $c = 13.515\,\text{Å}$, and $\beta = 90.46°$ [64]. Here, the molecules are arranged in a herringbone manner with two inequivalent molecules per unit cell twisted towards each other by an angle of 58°. Note that the herringbone arrangement is a common packing motif for aromatic molecular crystals [88]. The unit cell is displayed in Fig. 4.1 (b). In the single crystalline form, picene behaves as a wide-gap semiconductor with an energy gap of $E_{\text{gap,opt}} = 3.3\,\text{eV}$ [65]. The given value is the optical gap, which has been confirmed by electron energy loss spectroscopy (EELS) [89]. From the same measurements, the transport gap has been

Table 4.1: *Lattice parameters for doped picene from the literature. A and B denote structures with different positions of the K atoms in the lattice depending on the initial position of the K atoms before relaxation. Lattice constants marked with ‡ are the basis for further calculations within this thesis.*

	a (Å)	b (Å)	c (Å)	β (°)	source
K_1(A)	7.267	7.387	12.698	95.79	[73]
K_1(B)	8.234	6.554	12.807	94.65	[73]
K_2	7.237	7.506	12.624	94.20	[73]
K_2K_1	8.776	6.394	13.346	94.03	[73]
K_3(A)	7.421	7.213	14.028	104.53	[73]
K_3(B)	7.408	7.223	14.116	105.93	[73]
K_4	7.511	7.058	14.230	102.96	[73]
K_3	7.359	7.361	14.018	105.71	[72]
$K_1^‡$	7.248	7.312	13.149	102.3	[87]
$K_2^‡$	7.306	7.348	12.74	92.59	[87]
$K_3^‡$	7.462	7.302	13.975	103.28	[87]

estimated to be $\sim 4\,\text{eV}$, substantiated by calculations in the *GW* approximation[1] revealing a gap energy of 4.08 eV. In contrast to DFT based calculations, *GW* does not underestimate E_{gap} but is able to predict gap energies close to the experimental values.

For K-intercalated picene ($K_x$picene with x = K concentration) only an insufficient structural characterization from experiment is available in the literature. For the particular case of K_3picene, powder X-ray diffraction reveals the lattice parameters $a = 8.707\,\text{Å}$, $b = 5.912\,\text{Å}$, $c = 12.97\,\text{Å}$, and $\beta = 92.77°$ [7], implying a shrinking of the unit cell. In contrast to K-intercalated pentacene, in which the K atoms are inserted between layers of upright standing molecules (see Chap. 5.1), in $K_x$picene the additional atoms are placed within the layers (intralayer insertion). Concerning pentacene, the interlayer insertion is directly reflected in an expansion of the *c*-axis lattice constant, whereas in picene *c* remains largely unaffected or rather gets compressed. In addition to the experimental findings, several theoretical studies provide calculated lattice parameters by structural relaxation within DFT taking into account forces and stress. All results substantiate the assumption of an intralayer insertion. These are summarized in Tab. 4.1. Considering the calculated lattice parameters for K_1 and K_3 by Kosugi *et al.* [73], two different starting points for the relaxation have been chosen. Thus, the resulting structures differ from each other by the exact position of the K atoms in the lattice (denoted A and B, respectively). ‡ mark lattice constants obtained by Jeschke *et al.* [87] which are

[1] In the *GW* approximation, the self energy is approximated by the product of the Green's function G and the screened Coulomb repulsion W.

the basis for more profound calculations presented later in this thesis. For the determination of the crystal structure of $K_x$picene ($x = 1, 2, 3$) by structural relaxation within DFT the generalized gradient approximation (GGA) has been used by Jeschke *et al.*[87]. Here, the projector augmented wave basis was used as implemented in VASP (Vienna *ab initio* simulation package)[90–93] with additional van der Waals corrections included in the relaxation process. A subsequent analysis of the electronic structure was performed with the full potential local orbital code, FPLO [87]. The resulting structure is plotted in Fig. 4.1 (c). It is noticeable that for $x = 1$ and $x = 2$ the molecules exhibit a slight torsion due to the presence of a positive ion in between. This torsion mainly vanishes for $x = 3$, where the cations are more homogeneously distributed in the empty space of the molecular crystal unit cell. Furthermore, the angle between the two inequivalent molecules in the unit cell (herringbone angle) increases upon insertion of foreign atoms as will be discussed in detail in Chap. 4.4.4.

4.2 Growth and structure of pristine picene films

Regarding the analysis of K-intercalated picene by means of photoelectron spectroscopy it is advantageous to use *in vacuo* grown thin films instead of single crystals for two reasons. On the one hand, picene is a very expensive material. The required amount of pure picene powder in order to grow a sufficiently large picene single crystal would cause enormous costs. Moreover, due to the high reactivity of potassium, the growth of K-intercalated picene single crystals proves fairly difficult. So far, only the fabrication of polycrystalline powder was achieved as, e.g., used by Mitsuhashi *et al.* [7]. For photoemission experiments, in turn, usually single crystalline samples are preferred. On the other hand, in ultra high vacuum (UHV) the contact of pure picene films as well as K intercalants to ambient air is avoided between fabrication and investigation. Already small quantities of oxygen in the residual gas may hamper the formation of pure $K_x$picene as will be discussed in Chap. 4.4.3. Due to the high reactivity of potassium, special care has to be taken in handling K-intercalated picene.

In the framework of this thesis picene films have been fabricated on several substrates, namely natively oxidized silicon (denoted $\mathbf{SiO_2}$), the 7×7-reconstructed (111)-surface of silicon (**Si-7×7**), thin bismuth films grown on Si(111)-7×7 (**Bi/Si**) as well as strontium titanate ($\mathbf{SrTiO_3}$) and zinc oxide (**ZnO**). Film growth was carried out by evaporating purified picene powder from a low-temperature effusion cell constructed by MBE Komponenten GmbH (organic material effusion cell, OME). For this purpose, a separate UHV chamber with a base pressure $< 5\times10^{-9}$ mbar was available, not exceeding 3×10^{-8} mbar during evaporation. Intercalation of the films with alkali metal (in particular potassium, but also sodium and cesium) atoms was achieved by subsequent evaporation of the respective material from a current heated commercial SAES getter source onto the films in the analysis chamber. Here, the base pressure was $< 5 \times 10^{-10}$ mbar and did not change during evaporation. Structural characterization of most of the pristine films was

performed by atomic force microscopy (AFM) and X-ray diffraction (XRD), both in ambient atmosphere. For recording the surface images a Veeco AFM was used. It was operated in the non-contact tapping mode. The diffractograms were taken using X-rays from a Cu K_α source with a wavelength of 1.5418 Å in a simple $\theta - 2\theta$ geometry.

Figure 4.2 shows $5 \times 5\,\mu m^2$ AFM images of picene films grown on the different substrates. Nominal film thicknesses are 15 nm (on Si-7×7, $SrTiO_3$), 20 nm (on Bi/Si), and 30 nm (on SiO_2, ZnO). These nominal values are obtained from monitoring the film growth with a quartz crystal microbalance (QCM). They are only a rough estimate of the deposited thickness, since one assumes the same sticking coefficient for all substrates. Moreover, these sticking coefficients are supposed to be equal to the sticking coefficient of the quartz crystal. In the surface morphology images the deviations between nominal and actual thickness become obvious (see below). A major unique feature observed for films on all substrates is that picene obeys the Vollmer-Weber (3D, island) growth mode. This is manifested in the formation of crystallites with their (a, b)-plane perpendicular to the substrate surface normal. Furthermore, the films are composed of rotational domains. The island size varies from 500 nm to more than 1 μm depending on the substrate.

Picene films on **SiO_2** and **ZnO** have a very similar form of appearance. While they differ in island size (on SiO_2: $\sim$ 500 nm, on ZnO: $\sim$ 1 μm), the shape of the islands is dominated by characteristic domain angles of 120° in both cases. Here, the occurrence of rotational domains can be directly observed by the arbitrary distribution of the characteristic domain angles across the substrate plane. The angle can be identified in the AFM images as denoted in Fig. 4.2 (a) and (c). Additionally, corresponding height profiles recorded along the solid lines, indicated in the morphology images, are shown. From the height profiles an average island height of $50 - 60$ nm can be inferred for the picene films on SiO_2 and ZnO. A more detailed analysis of the island heights is given in A.2. Deduced from the AFM images, film coverages of $75 - 79\%$ (SiO_2) and $76 - 88\%$ (ZnO) have been reached. From film coverage and average island height a film thickness corresponding to a homogeneously covered surface can be deduced. It will be termed 'effective' film thickness in the following and can be compared to the nominal thickness obtained by QCM monitoring. Based thereon, the effective thickness of picene films on both substrates, SiO_2 and ZnO, amounts to $\sim$ 40 nm, which is by 30 % larger than the nominal value from QCM monitoring.

Two further substrates on which picene shows similar growth behavior are **Si-7×7** and **Bi/Si**. Corresponding AFM images are displayed in Fig. 4.2 (b) and (e). In both cases the islands have a size of $\sim$ 1 μm or even exceed this value. The surface is more homogeneously covered than on SiO_2 and ZnO and the islands partially coalesce. Note that the bright, washed-out spots distributed over the surface of Bi/Si are not caused by picene but are a remnant of the bismuth film beneath. Ideal Bi growth on Si(111) -7×7, i.e., a homogeneously covered surface, could not be established within the framework of this thesis. The surface of the Bi films always exhibited such bright spots determined by high, tower-like clusters aggregating on the surface during growth. However, also

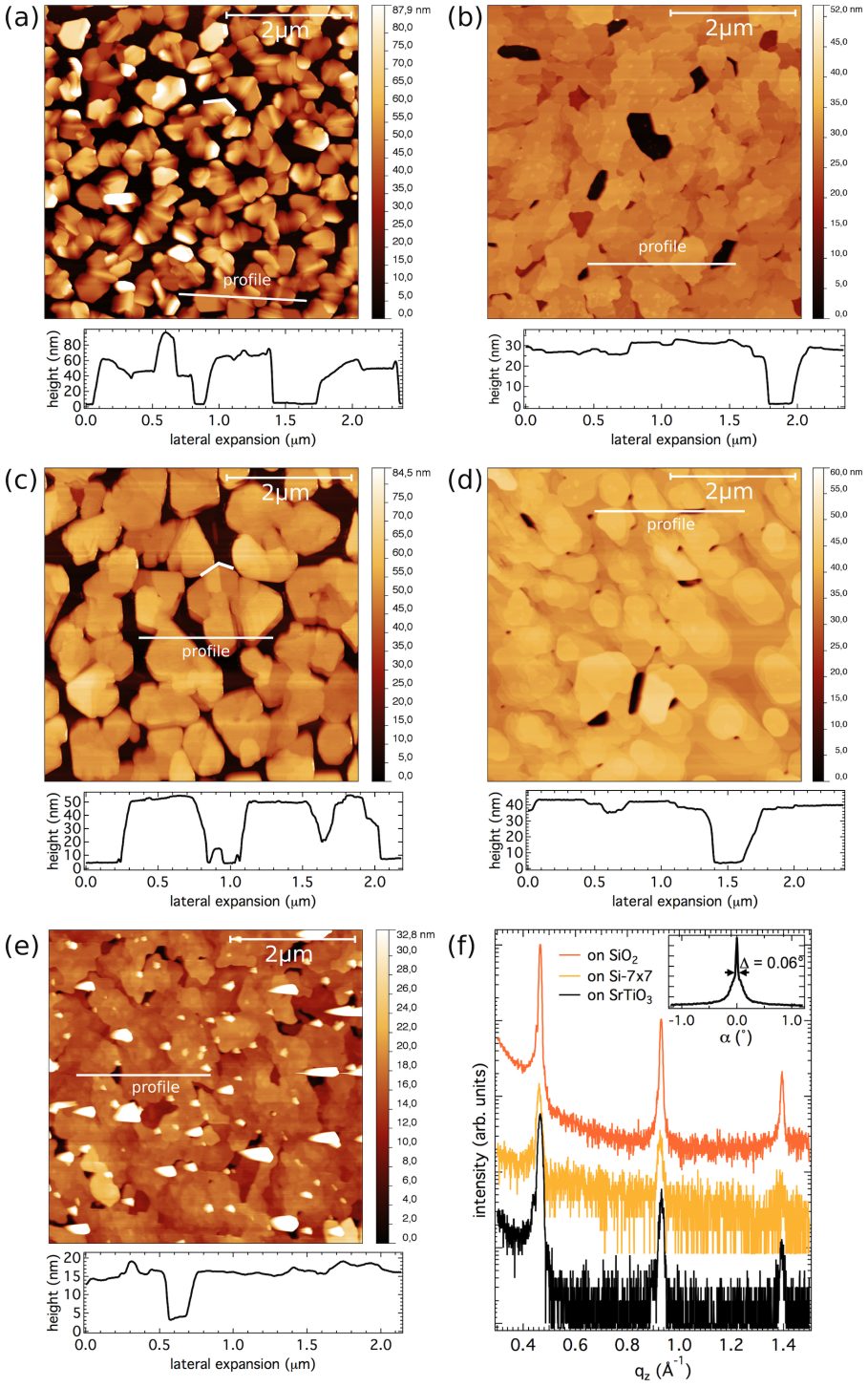

Figure 4.2: $5 \times 5\,\mu m^2$ *AFM images of picene films grown on (a)* SiO_2*, (b) Si-7×7, (c) ZnO, (d)* $SrTiO_3$*, and (e) Bi/Si. Below each surface morphology image a corresponding line profile is plotted, recorded along the solid line in the image. (f) X-ray diffractograms of picene films on* SiO_2*, Si-7×7, and* $SrTiO_3$*. Inset: rocking curve of a picene film on* SiO_2*. Details see text.*

between the clusters the surface is covered with Bi, since in XPS no signal of the Si substrate could be detected. In the area between the clusters the morphology of the picene films is similar to the morphology of films on Si-7×7. In this case, no characteristic domain angles are observable. The islands rather form a dendrite-like structure, whereas the dendrite arms are not as pronounced as, e.g., in pentacene films on $SrTiO_3$ (see Chap. 5.2). The respective height profiles (measured along the solid lines indicated in the AFM images) again allow an estimate of the average island height. It yields $\sim 30\,\text{nm}$ and $\sim 15\,\text{nm}$ for films on Si-7×7 and Bi/Si, respectively, confirmed by the height distributions in A.2. Taking into account the film coverages of $\sim 96\,\%$ (Si-7×7) and $88 - 93\,\%$ (Bi/Si), the effective film thicknesses, comparable to the QCM values, result in $\sim 30\,\text{nm}$ (Si-7×7) and $\sim 15\,\text{nm}$ (Bi/Si). In the case of Si-7×7, the film is twice as thick as estimated by the QCM, the film on Bi/Si is thinner and the thickness deviates by 25 % from the nominal value.

Finally, a slightly differing growth behavior can be observed for picene films on **$SrTiO_3$**. The films on $SrTiO_3$ exhibit the highest coverage of all substrates ($\sim 99\,\%$) and, similar to picene on Si-7×7, the islands partially coalesce. However, the islands have no dendrite-like edges but rather have a round shape. Islands of a size between 500 nm and $1\,\mu\text{m}$ can be found in the morphology image. Deduced from the height profile, the average island height is $\sim 40\,\text{nm}$, corroborated by the height distribution analysis in A.2. Thus, the effective thickness of picene films on $SrTiO_3$ shows the largest deviation from the nominal thickness obtained from the QCM monitoring. 40 nm of effective thickness front a nominal value of 15 nm.

In-plane, the islands are rotated arbitrarily and have no preferred overall orientation. However, along the c-axis the films are highly ordered, demonstrated by the XRD patterns in Fig. 4.2 (f). Diffractograms in the q_z-range of $0.3 - 1.5\,\text{Å}^{-1}$ are displayed for picene films on SiO_2, Si-7×7, and $SrTiO_3$. All observable peaks can be identified as $(00l)$ Bragg peaks, indicating a c-axis lattice spacing of $(13.5 \pm 0.1)\,\text{Å}$. This value perfectly agrees with the lattice spacing of picene single crystals from the literature [64]. Furthermore, the narrow rocking curve [inset in Fig. 4.2 (f)] indicates the well-defined alignment of the crystallites along the surface normal with an average tilting angle of only $\pm 0.03°$. The measurability of only the Bragg reflections of the c-axis lattice spacing indicates a film growth in which the molecules arrange with their long molecular axis parallel to the substrate surface normal (standing mode). For elongated organic molecules this is a common growth mode when the molecule-molecule interaction overweighs the substrate-molecule coupling (see also Chap. 5.2) [94, 95].

In summary, picene forms islands with a size varying from 500 nm to $1\,\mu\text{m}$ for growth on the different utilized substrates. The films differ in the shape of the island edges but on all substrates the islands represent rotational domains with arbitrary in-plane arrangement. Out-of-plane, the films are highly ordered with a c-axis lattice parameter of 13.5 Å, indicating film growth in standing mode. The nominal film thicknesses given in the following have to be handled with care, since they deviate from the effective film thicknesses to a certain extent.

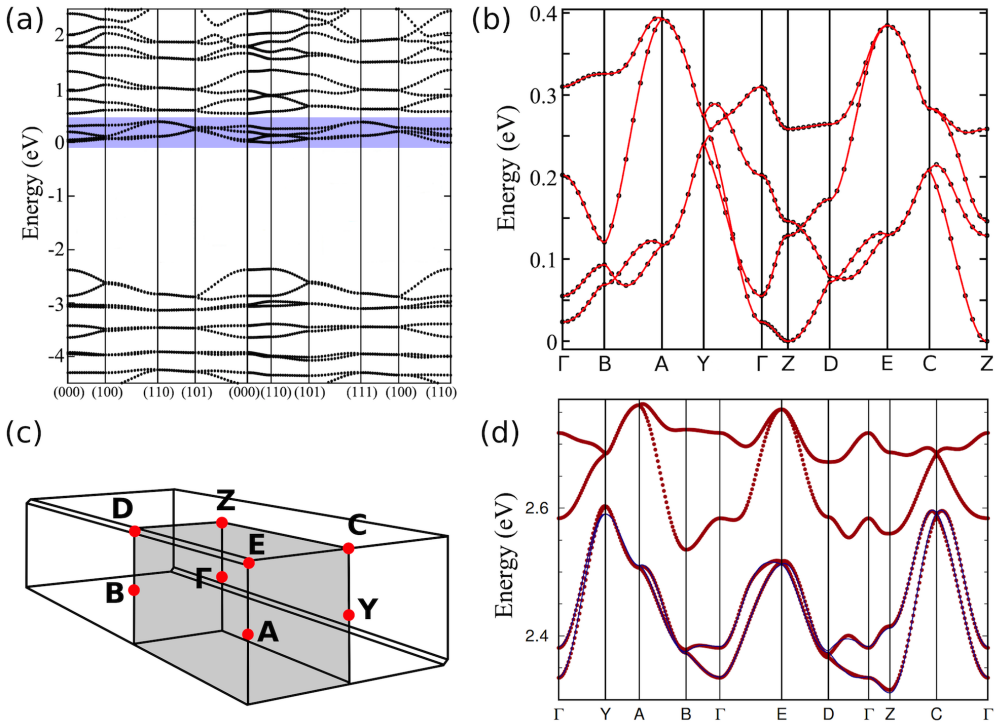

Figure 4.3: *(a) Band structure of undoped picene obtained by DFT (LDA) from Kosugi et al. Zero energy is set to the conduction band minimum. (b) Blow-up of the four lowest unoccupied bands in (a) marked by the shading. Figures (a) and (b) reprinted from Ref. 71, Copyright (2013), with permission from The Physical Society of Japan. The results from DFT (dots) are compared to a tight-binding fit (red solid lines). (c) Picene Brillouin zone: the important high symmetry points are labelled. (d) The four lowest unoccupied molecular orbitals of picene from band structure calculations within DFT (GGA) (red dots) in combination with a tight binding fit (solid blue lines) from Ref. 87.*

4.3 Electronic structure of pristine picene films

In this section, the electronic structure of pristine picene films examined experimentally by means of photoelectron spectroscopy will be reported. For this purpose, core level and valence band analyses have been conducted using monochromatized Al K_α (1486.6 eV) and He I (21.2 eV) radiation, respectively. Most of the measurements have been performed at room temperature with a total energy resolution of 0.7 eV for XPS and 0.1 eV for UPS. Exceptions are described in the corresponding section.

4.3.1 Important aspects from the literature

To get first insight into the electronic structure, or more precisely, the electronic band structure from a theoretical view, density functional theory (DFT) calculations are a helpful tool. Basic *ab initio* calculations in the local density approximation (LDA)

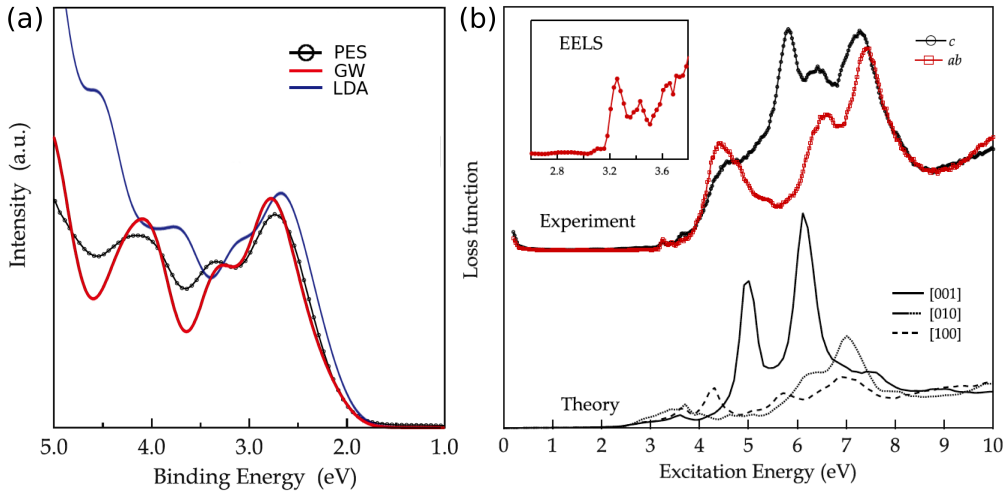

Figure 4.4: *(a) Valence band region of photoemission spectra of a pristine picene film grown on a gold substrate in comparison with the electron DOS calculated from DFT (LDA) as well as the k-integrated spectral function obtained from the GW approximation. (b) EELS spectra (recorded in two different measurement geometries) of a pristine picene film compared to calculations of the loss function within RPA. Figures reprinted from Ref. 89 with permission from F. Roth. Copyright (2013) by IOP Publishing.*

within DFT for pristine picene have been accomplished by Kosugi *et al.* in 2009 [71]. The resulting band structure is shown in Fig. 4.3 (a) for energies ranging from −4.5 to 2.5 eV. The Fermi energy (in this case $E_F = 0$ eV) has been set to the conduction band minimum. Note that for an ideal semiconductor it would be at the middle of the band gap. From the calculations a band gap of 2.36 eV can be extracted, notedly underestimating the real size of the gap, which is a well-known shortcoming of DFT calculations. A small cutout of the band structure, containing the four lowest unoccupied bands, is displayed in Fig. 4.3 (b) together with a *tight binding* fit. Here, an energy region of $\sim$ 0.4 eV is covered. The corresponding high symmetry points are indicated in the sketch of the picene Brillouin zone in Fig. 4.3 (c). For comparison, the same energy region of the picene band structure calculated in the general gradient approximation (GGA) within DFT by Jeschke *et al.* [87] is shown in Fig. 4.3 (d). These results are the basis for more detailed calculations presented later in this thesis. The seeming difference between the two band structure plots is only due to different paths through the Brillouin zone chosen by the authors. In general, both band structures perfectly coincide. Basis of the illustrated calculations is solid picene with the experimental lattice constants determined by De *et al.* [64] and reproduced by Mitsuhashi *et al.* [7]. The atomic positions are relaxed within DFT, retaining the experimental lattice parameters.

Beside the underestimation of the energy gap, another shortcoming of DFT is the correct determination of the electron density of states (DOS) near the Fermi level for molecular systems like picene. A different approach providing a more exact description

of the energy-dependent DOS, or more precisely of the k-integrated spectral function, is the *GW* approximation. The k-integrated spectral function of pristine picene calculated in the *GW* approximation is plotted in Fig. 4.4 (a) together with the DOS resulting from DFT (LDA) and a measured photoemission spectrum [89]. In the range of 1 to 5 eV with respect to the Fermi energy the *GW* results agree very well with the measured data. On the other hand, the LDA DOS is not able to reproduce the exact energetic positions of the peaks in the low binding energy region.

Additional insight in the electronic structure of pristine picene can be obtained by electron energy loss spectroscopy (EELS). Corresponding data from the literature are shown in Fig. 4.4 (b). Again, the experimental results are compared to calculations. Here, the loss function has been calculated within the random phase approximation (RPA). From the experiment a well-structured loss function is attained in which the single peaks are assigned to molecular electronic levels of picene. The electronic levels are also in agreement with the electronic DOS from photoemission in Fig. 4.4 (a). The authors ascribe the peak maxima from EELS to excitations between the energetically close-lying first occupied and unoccupied electronic states of picene [89]. Apart from an underestimation of the band gap and the resulting underestimation of the peak positions, the calculations agree well with the experimental data. The deviations are due to *GW* corrections and excitonic effects not included within the presented calculations. Conclusively, both PES and EELS reveal a gap energy of ~ 4 eV in accordance with the value gained from the *GW* calculations. Considering the photoemission spectrum, the Fermi energy is assumed to lie in the middle of the gap. The small structures appearing at excitation energies lower than 4 eV in the loss function are ascribed to the occurrence of excitons, as the first peak at ~ 3.2 eV matches the optical gap of 3.3 eV from Ref. 65.

4.3.2 Electronic structure from photoemission

Turning to the photoemission spectra recorded on pristine picene films grown on different substrates as described above, the corresponding results are plotted in Fig. 4.5. The inset of Fig. 4.5 (a) shows two spectra of the entire valence band for films on SiO_2 and Si-7×7, respectively, which are in good agreement with the literature [84, 85, 89]. Spectra for films on $SrTiO_3$ and Bi/Si are similar to the present spectra and thus not shown separately. Most interesting is the energy region close to the chemical potential. Hence, spectra of picene films on the utilized substrates are displayed in Fig. 4.5 (a) for an energy interval ranging from 0.5 to -4.5 eV with respect to the experimental chemical potential (μ_{exp}). The experimental chemical potential μ_{exp} of the spectrometer has been determined by measuring the Fermi cut-off of a sputtered gold foil. For all spectra three major structures can be observed and are ascribed to the photoemission from the three highest occupied molecular orbital (HOMO) derived bands. As shown in the topmost curve, for picene on SiO_2 these bands are located at -2.2 (H), -2.8 (H-1), and -3.5 eV (H-2) relative to μ_{exp}. Depending on the substrate, the whole spectrum shifts to higher binding energies such that the exact positions of H, H-1 and H-2 differ from the ones

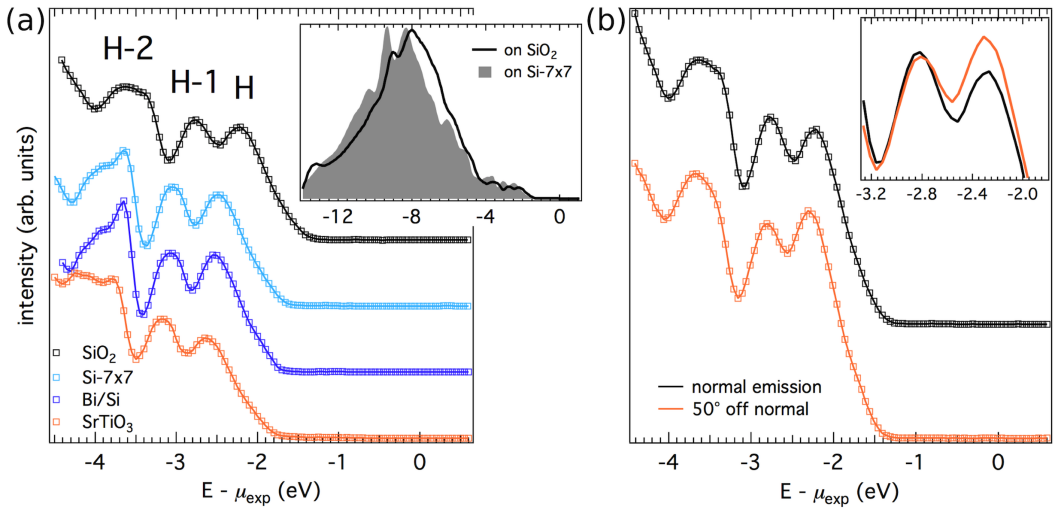

Figure 4.5: *Photoemission spectra of pristine picene. (a) Spectra for films grown on different substrates, viz., SiO_2, Si-7×7, Bi/Si, and $SrTiO_3$. The three highest occupied molecular orbitals are labelled H, H-1, and H-2, respectively. Inset: Valence band spectra over full energy range. (b) HOMO region spectra of pristine picene recorded in normal emission and 50° off normal emission to visualize the angle-dependent changes of the HOMO. Inset: Zoom into the relevant energy range.*

of picene on SiO_2. The origin of this behavior will be shortly discussed at the end of this section. Besides, the substructure of H-2 is considerably better resolved for picene on Si-7×7 and Bi/Si compared to the films on $SrTiO_3$ and SiO_2. Most likely, this is due to a better ordering of the molecules depending on the substrate surface cleanliness influenced by the pre-growth substrate preparation (for details of preparation see A.1). Irrespective of these two points, all spectra have the same shape and coincide with or even outperform the spectra reported in the literature [84, 85, 89, 96].

In Chap. 4.2 it has been shown that the picene films grow in standing mode with their long molecular axis parallel, or at least with a small tilt, to the surface normal. Such a behavior can also be seen in the valence band structure by measuring spectra for different photoelectron emission angles. It is empirically well-known that picene films display the same valence band structure independent of whether the molecules are standing or flat-lying on the substrate [85, 96]. The electronic structures only differ in the relative intensities of H and H-1 due to matrix element effects (angle-dependent cross-sections). Spectra produced by films consisting of standing molecules and recorded with an emission angle far off normal emission in UPS are similar to the corresponding spectra gained from lying molecules in normal emission. Figure 4.5 (b) shows the HOMO region of a picene film on SiO_2 recorded at normal emission and 50° off normal emission. It can be clearly seen that the intensity ratio between H and H-1 changes, implying the same trend as going from standing to lying molecule. The spectra conclusively confirm that the fabricated films grow in an upright standing manner. Hence, the film-substrate

interaction is minimized, permitting a good comparability with picene single crystals.

In order to supplement the information gained from valence band photoemission, a C 1*s* core level spectrum is plotted in Fig. 4.6 (gray curve). The C 1*s* peak with a full width at half maximum (FWHM) of 0.9 eV is located at a binding energy of $E_{\text{bind}} = 284.7\,\text{eV}$, perfectly agreeing with the literature [85]. Since the C 1*s* core level is the only core level accessible with Al K_α radiation, no further information can be deduced from XPS.

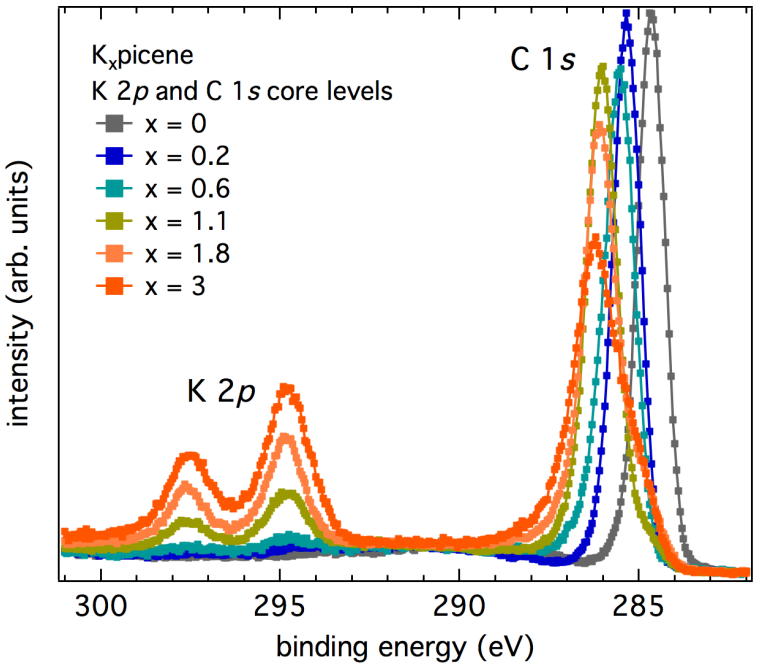

Figure 4.6: *K 2p and C 1s core level photoemission spectra of $K_x$picene for various K-doping concentrations ($0 < x < 3$). K-doping is reflected in a shift of the C 1s and an intensity gain of the K 2p line. Note that the concomitant decrease of the C 1s peak maximum intensity is misleading since the integrated intensity is retained due to the peak broadening.*

Earlier in this section it has been presented that the recorded valence band spectra of picene films grown on different substrates exhibit a certain shift depending on the utilized substrate. This varying HOMO offset (with respect to μ_{exp}) will be mentioned briefly in the following. Many organic materials exhibit only a weak van der Waals-coupling between molecular layers. Regarding the formation of layered structures on any substrate the system is not able to establish a thermodynamical equilibrium which would come along with the alignment of the chemical potential. Instead, similar to the investigation of single molecules the energy level alignment rather takes place via a vacuum level alignment [97, 98]. Thus, depending on the work function of the substrate and the ionization energy of the molecule, the HOMO position relative to μ_{exp} may vary. This fact will play a crucial role in Chap. 4.4.1 and will be discussed in detail there.

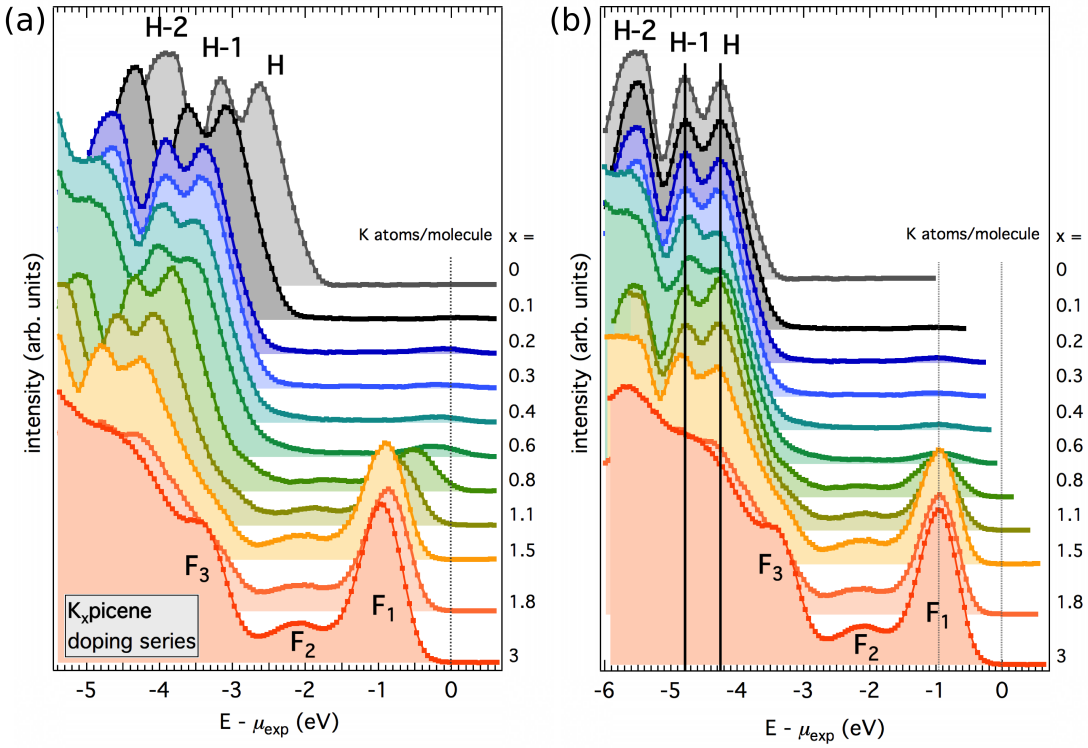

Figure 4.7: *Valence band photoemission spectra of $K_x$picene in a range of $\sim 5\,eV$ of the HOMO region for various K-doping concentrations. Spectra are shown for $x = 0 - 3$. (a) As measured, (b) energetically aligned on the spectral features of the $x = 3$ compound. Details see text.*

4.4 K-doping: Extrinsic vs. intrinsic contributions to the electronic structure

The picene films illustrated in the previous sections are now the basis for further investigations of the influence of potassium-doping on the electronic structure. Doping was achieved by subsequent evaporation of potassium onto the pristine films. The resulting K-doped picene ($K_x$picene) was probed by PES. All but one films of this series were grown on SiO_2, the film with $x = 3$ was grown on Si-7×7. The essential behavior of $K_x$picene films is the same for the substrates SiO_2, Si-7×7 and Bi/Si. Differences come into play for $SrTiO_3$ and ZnO, which will be discussed in detail in Chap. 4.4.3. K concentrations given in the following are obtained from a quantitative analysis of the potassium and carbon core levels. A detailed description of the determination is presented in A.3. Parts of the following contents have been published in Physical Review Letters [99].

Regarding the core level analysis, doping picene with electrons by intercalation of potassium manifests itself in two respects. First, in a shift of the C 1*s* peak. Second, in the appearance of spectral weight originating from the photoemission of the K 2*p* core level (see Fig. 4.6). For low K concentrations the C 1*s* peak progressively shifts to higher

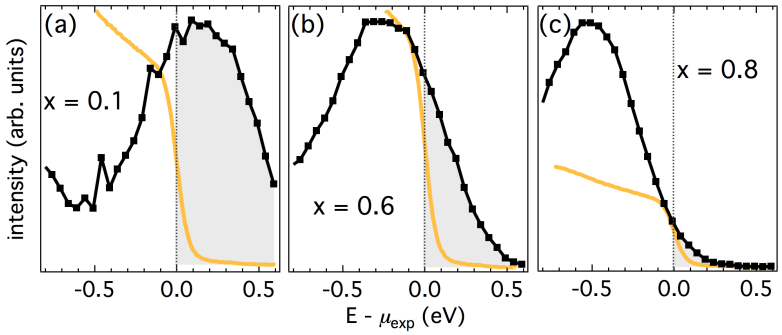

Figure 4.8: *Spectral weight of $K_x$picene in the vicinity of the chemical potential for doping concentrations of (a) $x = 0.1$, (b) $x = 0.6$, and (c) $x = 0.8$. Each spectrum contains the Fermi cut-off of a gold reference sample.*

binding energies saturating for large x at $\Delta E = 1.5\,\mathrm{eV}$. The observed shift is owing to an upshift of the chemical potential upon introducing additional electrons into the system. Furthermore, due to the increasing amount of K, an increasing intensity of the K $2p$ core level is observable. The spin-orbit split components are located at $E_{\mathrm{bind}} = 297.5\,\mathrm{eV}$ (K $2p_{1/2}$) and 294.8 eV (K $2p_{3/2}$).

Turning to the valence band analysis, the influence of K-doping is reflected as follows. In Fig. 4.7 (a) spectra for doping concentrations in the range from $x = 0$ to 3 are plotted from top to bottom. Considering the HOMO peaks H, H-1 , and H-2, one can observe a continuous shift away from the chemical potential towards larger binding energies. Moreover, a diminishment of spectral structuring and a smearing out of the HOMO region occur for larger x. The most prominent feature is a new peak appearing in the vicinity of μ_{exp} (denoted F_1), starting at $x = 0.1$ and progressively increasing upon doping and shifting the same way as the HOMO-related features. Furthermore, two more new peaks (F_2, F_3) arise beginning at $x = 0.8$ and $x \approx 1.5$, respectively. At first glance, the spectral weight at the chemical potential for low doping concentrations might signal a metallic behavior of the films, as anticipated from the calculations or expected intuitively for a slightly doped semiconductor. Though, having a closer look at the corresponding spectra for $x = 0.6$ and 0.8, as depicted in Fig. 4.8 (b) and (c), one can see that the spectral onset is far too broad to account for a sharp Fermi edge, even considering thermal and instrumental broadening. Going further to even lower doping concentrations [$x = 0.1$, see Fig. 4.8 (a)], it becomes evident that spectral weight is not only present at μ_{exp} but apparently also *above*. In a thermodynamical equilibrium situation such curious behavior is not possible. Thus, the occurrence of spectral weight above μ_{exp} must originate in a non-equilibrium scenario.

Altogether, there are four interesting phenomena occurring in the present series of $K_x$picene spectra, namely three new features $\mathbf{F}_1$, $\mathbf{F}_2$, and $\mathbf{F}_3$, as well as indications for **non-equilibrium behavior**. Their origins – either of extrinsic or intrinsic nature – will be clarified in the following sections.

4.4.1 Surface photovoltage vs. van der Waals-interaction

Firstly, the phenomenon of spectral weight above the chemical potential will be clarified. Since in thermodynamical equilibrium such a behavior is not physical, the underlying system obviously resides in a non-equilibrium situation. Non-equilibrium behavior allows deviations of the measured local chemical potential from the fixed Fermi level μ_{exp} of the spectrometer as obtained by a gold reference sample. In principle, there are two mechanisms which can explain the observed behavior: The inefficient electron exchange between substrate and film surface hampering the formation of a homogeneous chemical potential *or* the so-called surface photovoltage (SPV) effect induced by the incident UV-light used for photoemission analysis. While the latter effect has been discovered by Horn *et al.* on thin metal films deposited on semiconducting substrates [100], the former mechanism has been proposed by Koch *et al.* for Cs-doped *para*-sexiphenyl [101]. Essentially, this mechanism is more probably also the cause of the non-equilibrium in K-doped picene. In Ref. 101 the occurrence of a SPV effect has been ruled out by means of Kelvin probe measurements. Since for the studies within this thesis no Kelvin probe was available, the occurrence of a SPV effect has to be ruled out by the aid of the photoemission results. A detailed quantitative analysis will be given in the following assuming the SPV effect as responsible mechanism for the non-equilibrium.

Discovered in the early nineties, the SPV effect is well-known to influence the appearance of surface analysis photoemission spectra. The point of matter is a finite potential at the surface enforced by the separation of afore created electron-hole-pairs [100, 102–104]. Moreover, band bending at the interface plays a crucial role in this scenario. The local Fermi level of the interface is not equal to the reference Fermi level and the measured spectral weight thus may lie above the reference Fermi level. A similar situation can be created by the evaporation of dopants onto organic semiconductors, like for potassium-doped picene. The first prerequisite for the occurrence of a SPV effect is that initially the pristine film is in thermodynamical equilibrium with the substrate.[1] This implies the alignment of the Fermi levels of substrate and molecular film. A second necessary prerequisite is a K concentration gradient at the surface of the films which is naturally given by the intercalation conditions. As potassium is subsequently evaporated onto the deposited pristine films, for typical evaporation times of a few minutes and consequently low K amounts the potassium atoms cannot diffuse sufficiently deep into the film. Thus, they accumulate in the surface region leading to a K concentration gradient as it is sketched in Fig. 4.9 (a). The presence of a K gradient is reflected by the intensity changes of the K $2p$ core level spectra depending on the photoelectron detection angle. Corresponding spectra are shown in Fig. 4.9 (b). The spectra are normalized to the intensity of the neighboring C $1s$ core level and clearly show different intensities for surface and 'bulk' sensitive measurements.

Based on the K concentration gradient, a simple model is developed in the following according to Horn *et al.* to describe the origin of the observed SPV effect. A sketch

[1] In the SPV scenario, the prerequisite of thermodynamical equilibrium is assumed to be fulfilled.

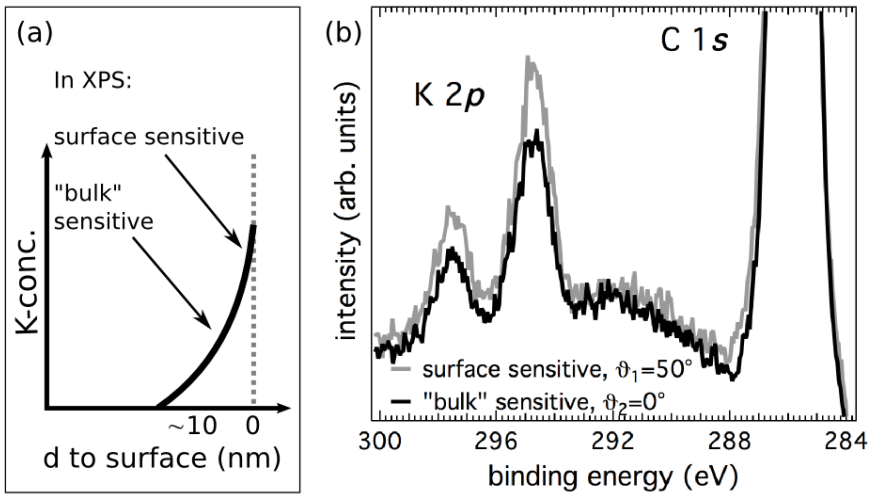

Figure 4.9: *(a) Sketch of the depth-dependent doping concentration in $K_x$picene. The arrows denote the regions for surface and 'bulk' sensitive measurements in XPS. (b) Corresponding K 2p and C 1s core level spectra for surface ($\vartheta_1 = 50°$) and 'bulk' ($\vartheta_2 = 0°$) sensitive measurements which illustrate the K concentration gradient.*

of the corresponding band diagram is plotted in Fig. 4.10 (a). Within the model, the pristine picene films grown on the SiO_2 surface display semiconducting band behavior with the Fermi level lying close to the band gap center. Note that the Si-SiO_2-interface is sketched according to the well-known band alignment of semiconductor-insulator contacts but is not relevant for the present discussion. Approaching the surface region, the bands are bent downwards due to the concentration gradient of positive K ions and are even crossing the Fermi level. Thereby, occupied states at the surface are generated. Already drawn in the sketch are the potential barrier height, Φ_b, and the HOMO offset, Δ_H, which will become important later. The irradiation with light during photoemission now creates not only photoelectrons but, mainly due to multiple scattering of the photoelectrons, also electron-hole-pairs. Due to the internal field gradient, the electron-hole-pairs get and remain separated [Fig. 4.10 (b)]. This is supported by an effectively reduced recombination rate due to asymmetric charge carrier mobilities for holes and electrons in picene [65–68]. Following the potential drop, the holes drift towards the SiO_2 interface, whereas the electrons accumulate at the surface forming a negative potential. The negative potential bends the HOMO- and LUMO-bands upwards and thus counteracts the initial down-bending caused by the K concentration gradient [Fig. 4.10 (c)]. Since the effect is a non-equilibrium effect (dynamical equilibrium), μ_{exp} no longer needs to be constant across the picene layers. One obtains a local dynamical equilibrium chemical potential μ_{dyn} for the thin surface region which is not equal to the reference level but may lie *above*. Increasing the amount of potassium leads to a rise of the spectral feature in the vicinity of μ_{exp} as well as a decrease of the SPV effect. The latter is discernible from the shift of the spectrum to higher binding energies while the relative peak distances

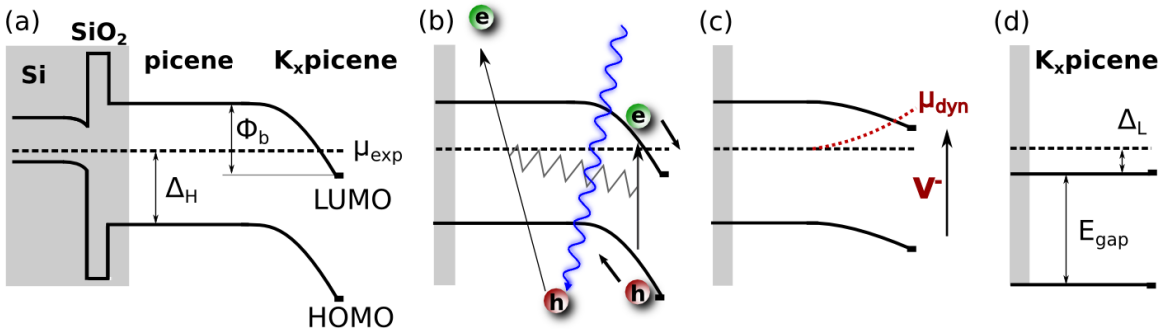

Figure 4.10: *Band diagram for SPV effect, description see text. (a) Band situation for low K concentration. (b) Electron-hole-pair creation by incident light in the photoemission experiments and subsequent electron-hole separation. (c) Modification of the initial situation by a negative potential due to charge accumulation at the surface leading to a local non-equilibrium chemical potential. (d) Equilibrium situation for the highest K concentration.*

remain unchanged. For an increasing x and concomitant longer diffusion times, the K atoms are allowed to distribute more homogeneously throughout the entire film. Due to the more shallow concentration gradient and the related band bending taking place over a larger film depth, the barrier height is reduced. The reduction of Φ_b, in turn, causes the decrease of the SPV effect. Finally, a near-equilibrium situation is reached for the highest K concentrations achieved as sketched in Fig. 4.10 (d). The relative shift of the spectral feature at μ_{exp} is a measure of the size of the associated photovoltage where the $x = 3$ spectrum is assumed to correspond to equilibrium, i.e., zero photovoltage. Extracted from Fig. 4.7 (a), the positions of peak maxima are plotted with respect to the intercalation level in Fig. 4.11. For the highest K concentration the feature at lowest binding energy is located at $-1.05\,\mathrm{eV}$, as can be extracted from the PES data. Assuming this energy to be the position of the peak for an equilibrium situation, the photovoltage is obtained to be $\mathrm{V}_{ph} = 1.22\,\mathrm{eV}$ from the experiment for $x = 0.1$.

In a simple model, this value for the photovoltage can be determined as it was proposed by Horn *et al.* for metal-semiconductor junctions (see above) [100, 102]. Considering a photocurrent $\boldsymbol{j}_{pc}$ induced by the incident light opposed to a thermionic current $\boldsymbol{j}_{th}$, which contains the photovoltage V_{ph}, as well as a recombination current $\boldsymbol{j}_{rec}$, one can calculate V_{ph} by solving $j_{pc} = j_{th} + j_{rec}$. Tunneling and leakage currents are assumed to be negligible. The respective currents are described in detail by Eqs.(4.1)-(4.3):

$$j_{pc} = \Phi_{phot} \cdot \frac{h\nu \cdot e}{E_{gap}} \cdot (1 - e^{-\alpha \cdot \lambda(n)}) \,, \tag{4.1}$$

$$j_{th} = A^* \cdot T^2 \cdot e^{-\frac{\Phi_b}{kT}} \cdot (e^{\frac{eV_{ph}}{kT}} - 1) \,, \tag{4.2}$$

$$j_{rec} = \frac{n_i}{\tau} \cdot e \cdot \lambda(n) \,. \tag{4.3}$$

Here, $\lambda(n)$ is the width of the depletion layer depending on the charge carrier concentration, n. It can be calculated with adequate formulas taken from textbook semiconductor physics [105]. The absorption coefficient α is estimated to be in the range of $8 \cdot 10^5\,\mathrm{cm}^{-1}$[106, 107], A^* is the effective Richardson constant of the films, calculated according to Scott and Malliaras [108]. $\frac{1}{\tau}$ is the recombination rate of electron-hole-pairs where the lifetime is typically in the range of pico- to nanoseconds for organic semiconductors [109]. n_i is the intrinsic carrier concentration of the organic semiconductor which is negligibly small for pure compounds. Due to the vanishing n_i, j_{rec} can be neglected in total. The most important parameters in this model are the effective charge carrier concentration n, defined by the K intercalation concentration and the potential barrier height Φ_b, given by the K concentration gradient induced band bending. The barrier height is calculated from the position of the HOMO with respect to μ_{exp} regarding a pristine film, Δ_H [see Fig. 4.10(a)] and from the position of the new feature in the vicinity of μ_{exp} in the final equilibrium situation at maximum K concentration, Δ_L [see Fig. 4.10(d)]. Taking into account the size of the band gap, E_{gap}, the barrier height yields $\Phi_b = 1.8\,\mathrm{eV}$. For the starting point of the intercalation series, viz., a concentration of 0.1 potassium atoms per picene molecule, a photovoltage of $V_{phot} = 1.20\,\mathrm{eV}$ can be obtained from the model. This value perfectly agrees with the one extracted from the photoemission measurements. Considering the assumption of a decreasing barrier height as well as the increasing carrier concentration, the model results in the progression of the photovoltage plotted as solid line in Fig. 4.11. At first glance, the model output agrees well with the measured evolution of the photovoltage and confirms the suggestion of a surface photovoltage effect in K-intercalated picene films. However, a further parameter with strong influence on the SPV effect was not mentioned yet: the temperature. According to the model, cooling the sample to 100 K should increase the photovoltage by 0.4 eV. In fact, cooling experiments did not show any variations. Hence, despite the remarkable agreement of model and experiment at room temperature the explanation of the observed non-equilibrium in terms of a SPV effect has to be ruled out based on this quantitative analysis. Instead, the responsible mechanism is the first one introduced at the beginning of this section.

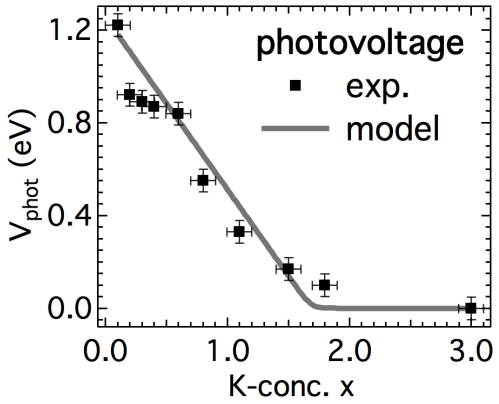

Figure 4.11: *Measured values for the photovoltage from UPS [markers, cf. Fig. 4.7 (a)] and curve obtained by the model calculations (solid line).*

It is as striking as simple. The point of matter is a lack of thermodynamical equilibrium due to an inefficient electron exchange between substrate and film surface. As the picene films consist of layers of standing molecules, as sketched in Fig. 4.12 (a), they experience a

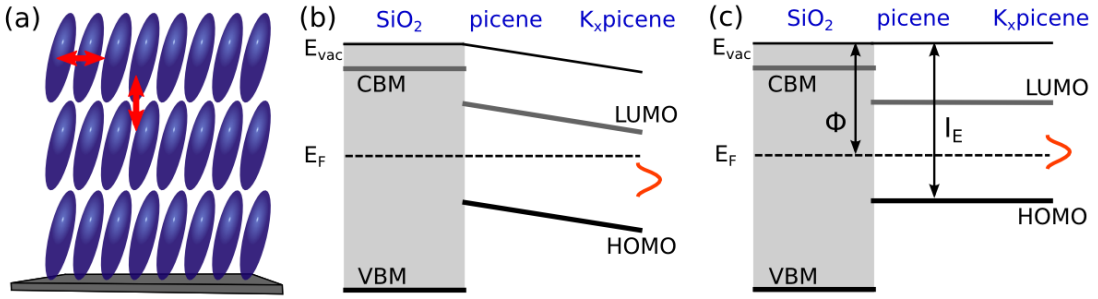

Figure 4.12: *(a) Interactions between molecules in layered films within the layers (horizontal arrow) and between the layers (vertical arrow). (b) Energy diagram of $K_x$picene on SiO_2. Scenario with equilibrated chemical potential. (c) Non-equilibrium situation and corresponding vacuum level alignment. Valence band maximum (VBM) and conduction band minimum (CBM) of SiO_2 as well as the highest occupied and lowest unoccupied molecular orbitals (HOMO, LUMO) of picene are labelled. Likewise, the Fermi energy (E_F) and the vacuum level (E_{vac}) are marked. The doping-induced spectral feature F_1 is sketched by the red peak. Adapted from Ref. 101.*

large π-orbital overlap of adjacent molecules *within* the layers (denoted by the horizontal arrow). However, perpendicular to the substrate surface (vertical arrow) the layers are only weakly van der Waals-coupled. Hence, in such a situation, charge fluctuations are strongly suppressed, thereby preventing the formation of a well-defined chemical potential. Similar behavior has earlier been found for alkali metal-doped *para*-sexiphenyl films by Koch *et al.* [101]. In Fig. 4.12 (b) and (c), the band situation for an equilibrium as well as a non-equilibrium scenario is schematically sketched according to Ref. 101. The thick solid black and gray lines symbolize the HOMO and LUMO of the picene overlayer and accordingly the valence band maximum (VBM) and conduction band minimum (CBM) in the case of the SiO_2 substrate. Furthermore, the vacuum level (E_{vac}) is represented by the thin black line, the Fermi energy (E_F) of the reference system is depicted by the dashed line. For a film consisting of covalently bond atomic or molecular layers, a homogeneous chemical potential would build up between substrate and film surface. By introducing a doped surface layer a bending of all corresponding bands, i.e., HOMO, LUMO bands and vacuum level would occur as displayed in Fig 4.12 (b) due to the Fermi level alignment. The doping-induced spectral feature F_1 is sketched by the red peak. The exact kind of band bending, e.g., curved or simply slanted, is not relevant for the present discussion. Hence, the sketch is kept as simple as possible. For the weakly van der Waals-coupled films, in particular picene and $K_x$picene, the setting is completely different. Here, the energy alignment does not refer to the chemical potential but rather to the vacuum level. It thus strongly depends on the work function of the substrate, Φ, and the ionization energy of the molecular overlayer, I_E. In addition, the subsequent potassium deposition results in a concentration gradient which decays from the surface into the film. Low K dosage then leads to a doped $K_x$picene surface layer with little or even no K present deeper in the film, maintaining the non-equilibrium situation. The combination of the SiO_2 work function ($\Phi = 4.5\,\text{eV}$ [110]) and the picene

ionization energy ($I_E = 6.4$eV [89]) results in a situation with a doping-induced feature in the HOMO-LUMO gap seemingly above the chemical potential in photoemission. Note that this is the chemical potential of the spectrometer, indicated by the dashed line in Fig. 4.12 (c). Upon further alkali metal-doping, charge fluctuations induced by doped electrons will now drive the system into a thermodynamical equilibrium. For higher K concentrations, the film will become doped throughout, hence establishing a well-defined chemical potential. In the presented films, the equilibrium situation is reached not later than for a doping concentration of $x = 3$. Here, the energetic position of F_1 exhibits no further shift. In supplemental measurements (not shown here) the equilibrium position of F_1 could be approved in low-doped films with considerably longer diffusion times. Further confirmation was obtained by the use of thinner films where the occurrence of a non-equilibrium is less pronounced [85]. With this knowledge, the spectra are now realigned on the positions of H and H-1 for the $x = 3$ spectrum, which incidentally fixes also the doping-induced features at constant energies showing gapped behavior for all K concentrations. The corresponding series of spectra is plotted in Fig. 4.7 (b). Based on these realigned spectra, the origin of F_1, F_2, and F_3 will be discussed in the following.

Note that the observation of spectral weight at the Fermi level reported by Okazaki *et al.* [84] for a nominal doping of $x = 1$ is probably due to the non-equilibrium behavior of peak F_1 described above. This also explains, why a clear Fermi edge could not be identified in that study.

4.4.2 Electronic correlations do the job

After realignment of the spectra it becomes clear that all spectra show similar behavior upon K intercalation. The most remarkable point is the absence of spectral weight at the chemical potential for all probed K concentrations together with the formation of the spectral feature F_1. In a simple picture the K atoms donate their $4\,s$-electron to a neighboring molecule in the molecular solid. An electron transfer implies the filling of unoccupied bands in the organic semiconductor. For odd or non-integer numbers of K atoms – and thus electrons – the doped semiconductor then is expected to show metallic behavior. Indeed, a filling of formerly unoccupied bands can be observed, however, metallicity is never achieved. Most surprising is the observation that even the $x = 3$ phase, for which superconductivity has been claimed, remains gapped. Nonetheless, this is in agreement with two previous PES studies [85, 86]. As one possible explanation polaronic effects have been suggested [85], which may cause a pseudogap at the Fermi level as has been observed, e.g., in oxides [111]. However, such a pseudogap exhibits an exponential decay towards the Fermi energy [112], which is not consistent with the present observation. Alternatively, the gap may originate from strong electronic correlations. In fact, in a Hubbard model-type description the intramolecular Coulomb energy U in organic solids is often comparable or even larger than the bandwidth from intermolecular hopping [74, 113], which can drive half-filled bands into a Mott insulating state. Electronic correlations have been claimed to play a crucial role in, e.g., K-doped

pentacene [15] and Alq_3 [114] as well as C_{60} [115]. For the particular case of picene, several theoretical groups report a LUMO bandwidth of $0.3 - 0.8\,\text{eV}$ from calculations [71–73, 82, 83, 89]. Additionally, a bandwidth of $0.5\,\text{eV}$ has been obtained from angle-resolved photoemission [96]. On the other hand, also the Coulomb repulsion has been determined from calculations (second-order Møller-Plesset) yielding a U of $0.85 - 1.7\,\text{eV}$ [82, 83] in good agreement with $U = 0.85\,\text{eV}$ from EELS [116].

In order to further explore the scenario of electronic correlations, the electronic properties of the DFT-relaxed crystal structures of $K_x$picene ($x = 1, 2, 3$) have been studied by a combination of DFT with dynamical mean-field theory calculations (DFT+DMFT), which include correlation effects beyond the GGA approximation in DFT [117]. Starting with the electronic structure for pristine and $K_x$picene obtained within GGA, the corresponding DOSs are plotted in Fig. 4.13 (a), (b), (d) and (f). A metallic state can be observed for odd x as well as a semiconductor band gap for $x = 2$, as has also been found in previous DFT calculations.

In DFT+DMFT the kinetic part of the Hamiltonian, H_K, in Eq. 4.4 is obtained from the DFT calculations by considering the tight-binding approach. Since the DFT results indicate some hybridization between the bands derived from LUMO and LUMO+1 of the pristine picene molecules, for the DMFT calculations a two-orbital Hubbard model with a Coulomb interaction U and Hund's coupling J_z as well as an on-site hopping parameter $t_\perp$ between molecular orbitals on the same site is considered. The Hamiltonian which is solved is $H = H_K + H_I$ where

$$\begin{aligned} H_K &= -\sum_{\langle ij\rangle m\sigma} t_m c^+_{jm\sigma} c_{im\sigma} - t_\perp \sum_{i\sigma} c^+_{i1\sigma} c_{i2\sigma} \\ H_I &= U \sum_{mi} n_{mi\uparrow} n_{mi\downarrow} + \sum_{\sigma} \big[(U - 2J_z) n_{1i\sigma} n_{2i\bar{\sigma}} + \\ &\quad + (U - 3J_z) n_{1i\sigma} n_{2i\sigma} \big]. \end{aligned} \tag{4.4}$$

Bands which are away from the Fermi level are not expected to be significantly renormalized by correlations and to save on computational effort they are ignored in the DMFT calculations. As an impurity solver for the DMFT equations the weak-coupling continuous time quantum Monte Carlo method was employed. The shown results are obtained for $T = 0.025\,\text{eV}$, $U = 1.6\,\text{eV}$ and $J_z = U/8$. This choice of interaction parameters was guided by recent quantum chemistry [83] and constrained random phase approximation (cRPA) estimates [74]. Note that for K_3picene, the metal-insulator transition was found to be between $U = 0.6\,\text{eV}$ (metallic) and $U = 0.8\,\text{eV}$ (insulating). The analytic continuation of the converged impurity Green's function to real frequencies was performed with the maximum entropy method. The resulting spectral function for these two orbitals is shown in Fig. 4.13 (c),(e) and (g), embedded into the DFT-DOS of the non-interacting bands.

For better comparison with the experimental data, the two correlated orbitals calculated by DFT+DMFT are plotted besides the spectra from UPS in Fig. 4.14 (a) and (b).

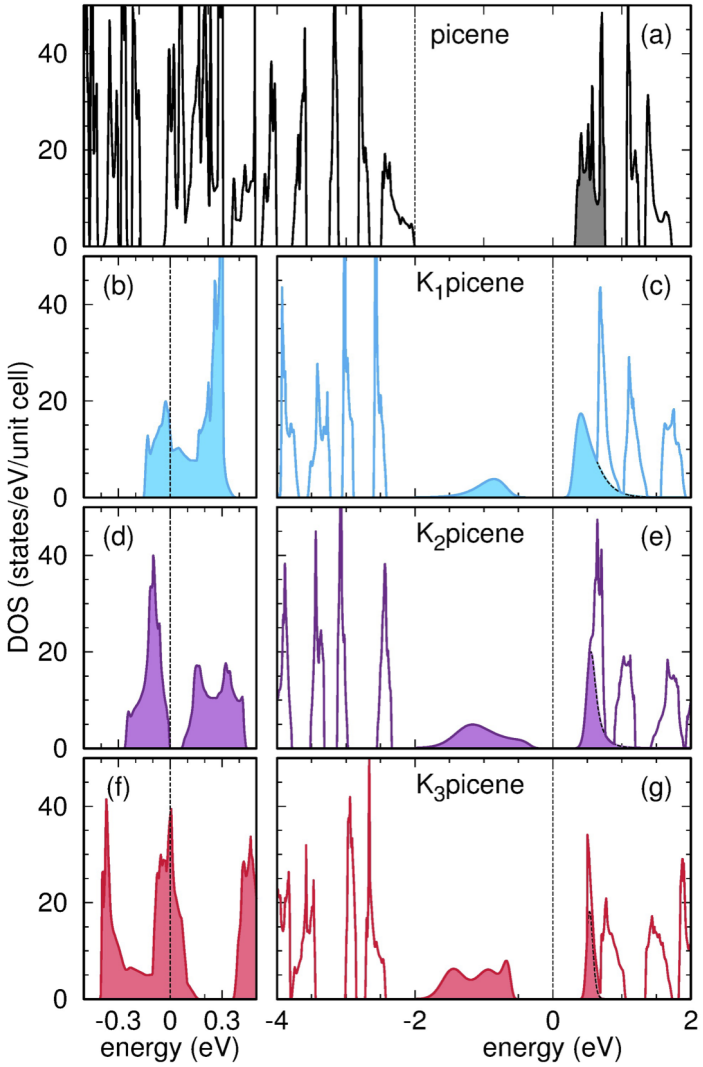

Figure 4.13: *Density of states of pristine and K-doped picene. (a) DFT DOS for pristine picene with the part of the spectrum arising from LUMO and LUMO+1 levels of picene marked by gray-shading. (b), (d), (f) DFT DOS of the region close to the Fermi level for K_1picene, K_2picene and K_3picene, respectively. (c), (e) and (g) DFT+DMFT DOS of the same compounds. For details see text. Figure from Ref. 99.*

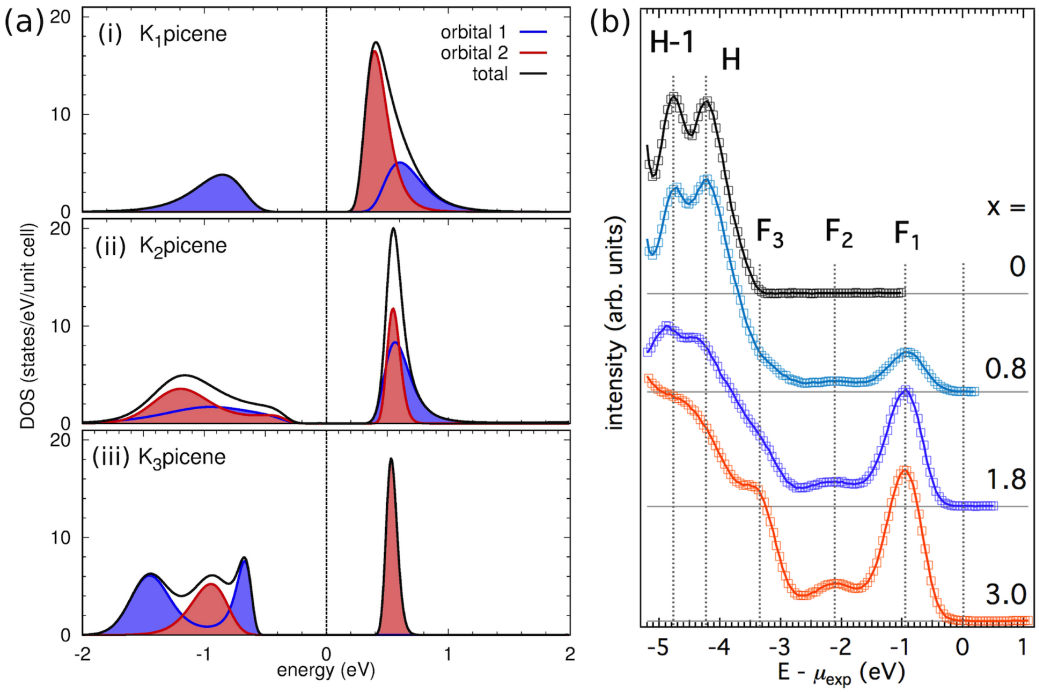

Figure 4.14: *(a) Orbital resolved and total DMFT spectral functions of (i) K_1picene, (ii) K_2picene and (iii) K_3picene. In each case both involved orbitals have Mott insulating character. (b) Valence band photoemission spectra showing the evolution with K-doping for various near-integer concentrations. The doping-induced features in the former bandgap are assigned by F_1, F_2, and F_3. All spectra are energetically aligned at the spectral features of the $x = 3$ spectrum, for which the existence of an equilibrium chemical potential can safely be assumed (see Chap. 4.4.1). Figures from Ref. 99.*

The DMFT spectral functions show a clear Mott gap not only for doping levels of $x = 1$ and $x = 3$ but also for $x = 2$ which in bare DFT is a band insulator with a small gap. A closer look at the DOS of K_2picene [Fig. 4.14 (a)(ii)] shows that – contrary to the expectation of a filled picene LUMO derived band and an empty picene LUMO+1 derived band – a Mott gap opens in *both* orbitals. Interestingly, energy positions and gap size do not seem to depend much on the actual doping level, except for the spectral weight transfer from upper to lower Hubbard bands. They correspond favorably with the experimental spectra, except for some fine structure at higher x not resolved in photoemission. The origin of the Mott gap for $K_x$picene with $x = 1, 2, 3$ lies not only in the on-site Coulomb interaction U and the Hund's coupling J_z but also in the interorbital hybridization $t_\perp$.

The good qualitative agreement between photoemission and DFT+DMFT is also illustrated in Fig. 4.15. It is evident that the fine structure of the spectral function from theory is not seen in the experiment. However, the important aspect of a gapped behavior is well reproduced by the calculations. Furthermore, regarding the first order

moment of the DMFT spectral function, also the peak positions of photoemission and theory are in good agreement. Both, experiment and theory thus arrive at the same conclusion that $K_x$picene films are (Mott-)insulating for all compositions with integer x, including the nominally superconducting phase $x = 3$. This leaves two open questions:

(1) What is the electronic groundstate for non-integer x, and

(2) how can the insulating behavior of the $x = 3$ phase be reconciled with the observation of a Meissner-Ochsenfeld effect as well as zero resistivity?

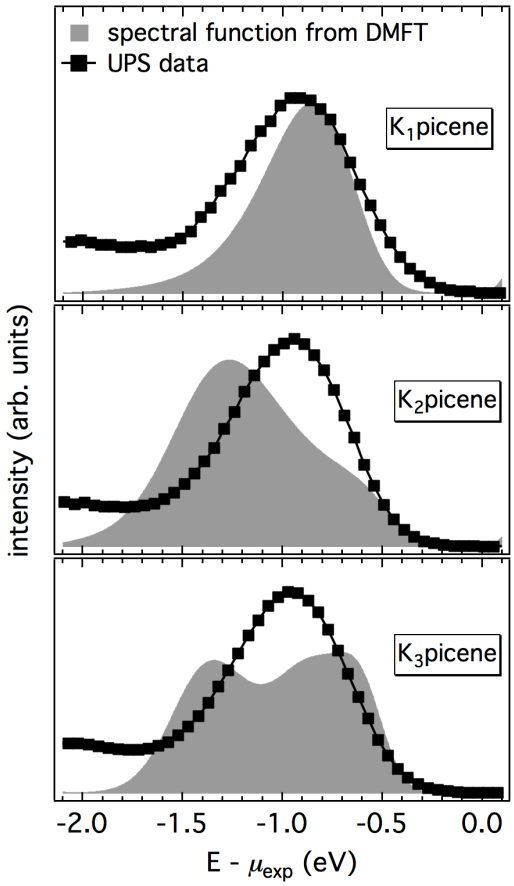

Figure 4.15: *Spectral functions for K_1picene, K_2picene, and K_3picene from DMFT in direct comparison with the photoemission spectra from UPS.*

Concerning the first question, it must be noted that in a Mott-insulator deviations from integer band-filling are normally expected to lead to a metallic phase with electron- or hole-type carriers [118]. Note, however, that the doping concentration determined in the photoemission experiments is a macroscopic quantity, averaged over the extension of the photon spot ($\sim$ 1 mm) and may be composed of phase-separated integer-filled domains. In fact, a recent Raman study [119] has observed that $K_x$picene decomposes into $x = 0$, 2 and 3 phases, while a defined $x = 1$ signal could not be detected, indicating that this phase is not stable. One can thus understand the photoemission spectra as a superposition of different integer x phases. Because the shape and gapped behavior of the corresponding theoretical spectra is very similar, the main doping effect will consist in the appearance and increasing spectral weight of the LUMO and LUMO+1 derived lower Hubbard band, as indeed reflected by the behavior of feature F_1 in the experimental spectra.

The second question is more puzzling. The present results are in line with the general observation that alkali metal-doped organic semiconductors are mostly insulating [24, 101], with K-doped fullerene (K_3C_{60}) being one of the rare exceptions [120]. On the other hand, in the original paper by Mitsuhashi *et al.* it has been reported that in $K_{2.9}$picene the diamagnetic (i.e., superconducting) phase is reached from a Pauli paramagnetic, hence

metallic phase [7]. This is supported by the observation of zero resistivity from transport measurements [12]. Reconciling the room-temperature results with these observations would require an insulator-to-metal transition somewhere between 300 and 25 K (the highest measured temperature in Ref. 7). The Mott-Hubbard scenario derived from our DFT+DMFT calculations does not provide any mechanism for such a transition but would rather stabilize the gap towards low temperatures. A confirmation of this assumption is given in Fig. 4.16 where a spectrum of K_3picene recorded at a temperature of 40 K is shown in comparison with a room temperature spectrum. Except for a small shift (0.1 eV) of the low temperature spectrum to higher binding energies both spectra are similar. The occurring shift might be due to slight charging effects of the insulating film at low temperatures. However, no significant changes in the spectrum are observable which would point to an insulator-to-metal transition as described above.

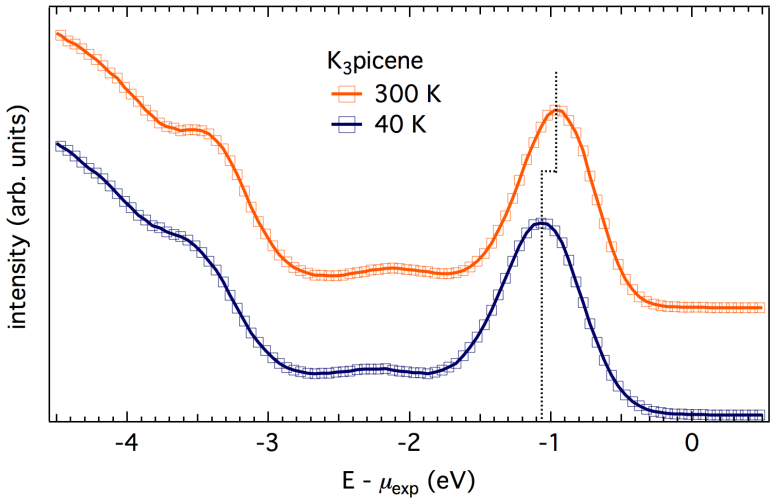

Figure 4.16: *Valence band spectrum of K_3picene at 40 K in comparison with a spectrum at room temperature. Apart from a slight shift due to charging, the spectra show no temperature-dependent variations. Both spectra exhibit a clear gap.*

Another important aspect is that so far all evidences for superconductivity have been obtained from intercalated compact picene powder [7, 12, 119], in contrast to the *in vacuo* grown thin films used in the framework of this thesis. It is possible that both sets of samples differ in subtle structural details accounting for the conflicting findings. On the other hand, the DFT+DMFT calculations are based on a DFT-relaxed *bulk* structure which one would expect to be relevant for the polycrystalline powder, at least for the interior of the powder grains. It is thus tempting to speculate about the possibility of the superconducting phase actually being located at the grain boundaries, which may have structural and/or electronic properties different from the bulk. Certainly more clarifying work needs to be done in this direction. Note that Kim *et al.* also report on Mott insulating behavior in K-doped picene from a very recent DFT+DMFT study, confirming the results presented in this thesis [121].

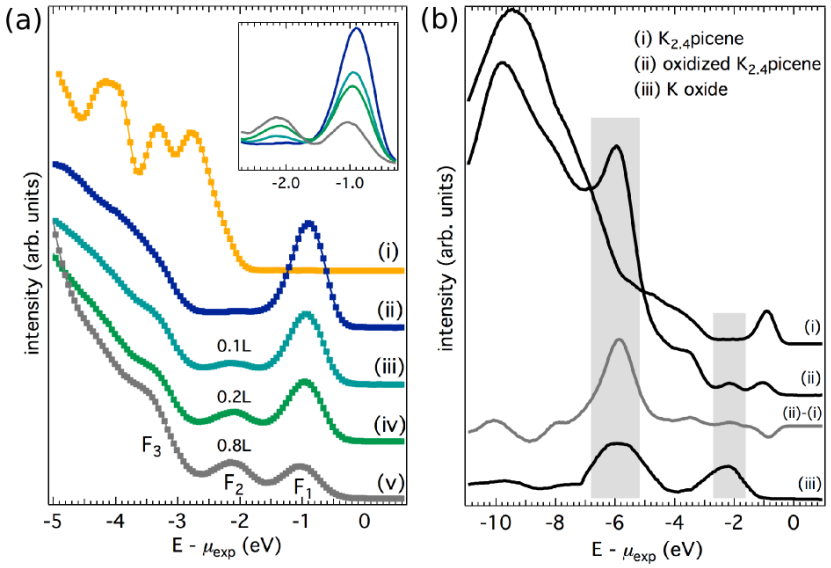

Figure 4.17: *(a) Evolution of the HOMO region of a picene film grown on SiO_2 upon K-doping and exposure to oxygen. In the inset a cutout of the relevant energy range is plotted. It is clearly visible that F_2 increases while F_1 decreases. For details see text. (b) Spectra in a wider energy range of $K_{2.4}$picene (i) and oxidized $K_{2.4}$picene (ii). The difference spectrum (ii)-(i) is compared with literature data of potassium oxide taken from Ref. 122.*

4.4.3 The delicate role of oxygen

The next step is unraveling the occurrence of F_2 in the former HOMO-LUMO gap. While only and exclusively F_1 is of correlated nature, F_2 does not result from the occupation of a molecular orbital upon doping but is the consequence of a reaction of the K atoms with oxygen. Oxygen is still existent also in the residual gas of a UHV system at a base pressure of $< 5 \cdot 10^{-10}$ mbar. A distinct correlation between oxidation and F_2 becomes evident from Fig. 4.17.

Figure 4.17 (a) shows the HOMO region of a picene film grown on SiO_2 as characterized above [curve (i)], which has been doped to $K_{2.4}$picene (ii) and subsequently exposed to different amounts [(iii): 0.1, (iv): 0.2, (v): 0.8 L] of pure molecular oxygen (purity > 0.999). Additionally, in the highest oxidized case the film was stored in UHV for 12 hours before exposure to oxygen and subsequent measurement to allow for a better structural relaxation. An increase in intensity of F_2 is obvious upon the controlled oxidation. The growing amount of oxygen in the films has been monitored by XPS as shown in Fig. 4.18 where the O 1*s* (a) as well as both the K 2*p* and the C 1*s* (b) core level spectra are plotted. In Fig. 4.18 (b) the spectra are normalized to the C 1*s* peak height to better compare the changes in the K 2*p* core level photoemission. The pristine picene film displays a typical C 1*s* line shape known from the literature [85, 86] as well as O 1*s* emission induced by the substrate surface. For the initially doped film the K 2*p* and C 1*s* core levels again agree well with the literature [85, 86]. Furthermore, at a binding

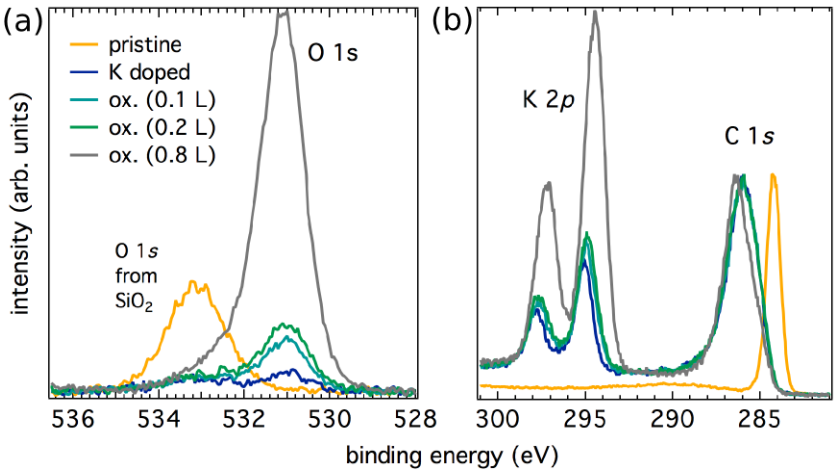

Figure 4.18: *(a) O 1s core level spectra of a pristine and K-doped picene films before and after exposure to different amounts of oxygen. The substrate is SiO_2. (b) Corresponding K 2p and C 1s core level spectra. The spectra are normalized to the C 1s peak height to illustrate the significant changes in the K 2p spectrum.*

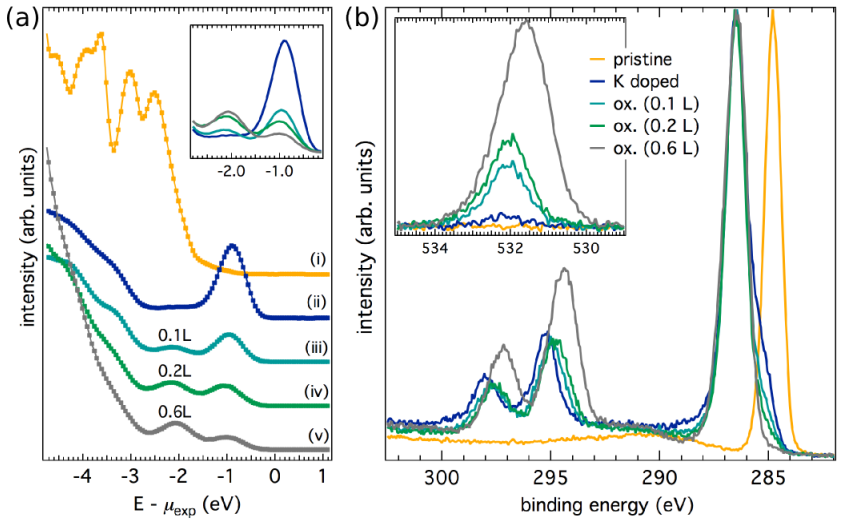

Figure 4.19: *(a) Valence band photoemission series of controlled oxidation for a picene film grown on Si-7×7. In the inset the spectra are plotted in a range close to μ_{exp}. (b) Corresponding K 2p and C 1s core level spectra. Again the spectra are normalized to the C 1s peak height. The inset shows O 1s core level spectra.*

energy of 531 eV already a tiny amount of oxygen is measurable, which considerably increases upon providing oxygen. According to Qiu *et al.* this can be attributed to the formation of potassium peroxide (K_2O_2) [122]. Details concerning different oxidation states of potassium can be found in A.4. Simultaneously, a shift of the K 2*p* core level peaks to lower binding energies is observable which can be ascribed to a chemical shift upon oxidation [123], confirming the presence of potassium oxide.

A further striking aspect is a strong increase of the K 2*p* intensity for the highest oxidized case [see Figs. 4.18 (b) and 4.19 (b)]. This points to an accumulation of K_2O_2 clusters at the surface or a K_2O_2 surface layer. An assumption of the underlying picture is that K atoms first diffuse into the film and donate their 4*s*-electron to the neighboring picene molecule. Under strong oxidation conditions, they segregate to the surface where they react with the oxygen which is present in the immediate vicinity of the surface. This requires that a reaction with oxygen forming potassium oxide is energetically more favorable than being placed in the lattice transferring the outer *s*-electron to a molecule.

In order to strengthen the information gained from XPS, a larger energy region of the valence band is displayed in Fig. 4.17 (b). Here, the spectra of the initially doped (i) and the maximally oxidized film (ii) are shown. Not only F_2 evolves upon oxidation but also a feature at an energy of −6 eV relative to the chemical potential arises which can be clearly seen in the difference spectrum (ii)-(i). A comparison with a reference spectrum obtained from measurements on pure potassium oxide from Ref. 122 shows that both features can definitely be attributed to the formation of potassium oxide.

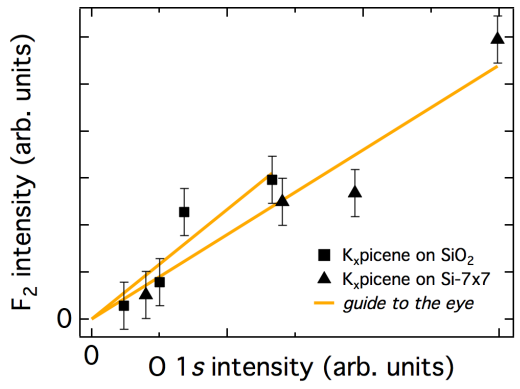

Figure 4.20: *Quantitative relation between oxygen amount and spectral weight of F_2. It clearly illustrates the connection between F_2 and oxygen. The straight yellow lines serve as a guide to the eye.*

Beside films grown on SiO_2, a similar study has been conducted on films grown on Si-7×7 with essentially identical results. The corresponding HOMO region series is displayed in Fig. 4.19 (a). Again, spectra are plotted for the pristine (i) and K-doped film (ii) as well as for the K-doped film exposed to a varying amount of oxygen [(iii): 0.1, (iv): 0.2, (v): 0.6 L]. As in case of the film on SiO_2, the sample was stored in UHV for 12 hours before the final oxidation step to allow again for a better structural relaxation. Also the core level spectra [Fig. 4.19 (b)] exhibit essentially identical behavior, i.e., the growing intensity of the O 1*s* core level peak reflects the increasing amount of oxygen. However, one distinction can be seen in the O 1*s* spectra. Initially, for the pristine film no peak is observable since the film is grown on completely oxygen-free Si-7×7. Furthermore, similar to the primarily described film, a shift of the K 2*p* core level peaks to lower binding energies originates from

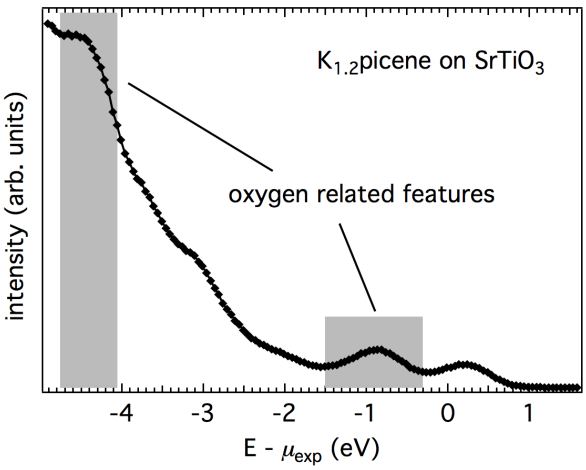

Figure 4.21: *Valence band spectrum of a $K_{1.2}$picene film on $SrTiO_3$ with pronounced features originating from the formation of potassium oxide. Note that the observable behavior occurs without intentional oxidation.*

a chemical shift owing to the oxidation of potassium.

To get a more quantitative view, the amount of spectral weight residing in F_2 is plotted against the amount of oxygen in the surface-near layers in Fig. 4.20. For this purpose, the area below the O 1*s* core level peaks as well as below F_2 has been determined. The spectra have been normalized to equal acquisition time for UPS and XPS, respectively. In each case a Shirley background has been subtracted to account for the secondary electrons in the further analysis. Also the effect of surface segregation of K atoms has been taken into account. From Fig. 4.20 it becomes obvious that an increasing amount of oxygen leads to an increase of F_2. The straight yellow lines serve as a *guide to the eye*. Consequently, the formation of F_2 is directly connected to the presence of oxygen. It is thus a purely extrinsic feature and is not related to the occupation of a molecular orbital of the picene molecules.

The discussion of the influence of oxygen on the electronic structure of $K_x$picene was based on the substrates SiO_2 and Si-7×7 so far. For Si-7×7 initially no oxygen is involved, for SiO_2 the oxygen is strongly bound to the surface and thus only marginally affects the formation of $K_x$picene. However, using $SrTiO_3$ (or ZnO) as a substrate is not suitable for investigating organic films upon K doping. In $SrTiO_3$ oxygen can easily diffuse through and leave the solid [124] and is then available for the oxidation of K. The actual strength of this effect is illustrated in Fig. 4.21. It shows a valence band spectrum of $K_{1.2}$picene fabricated on $SrTiO_3$ measured directly after preparation. Although no controlled oxidation has been applied, the spectrum strongly resembles the spectrum of a heavily oxidized sample. Both characteristic features which stem from the formation of potassium oxide are observable (gray shaded areas). Moreover, the whole spectrum is shifted to lower binding energies displaying spectral weight above μ_{exp}. As described in

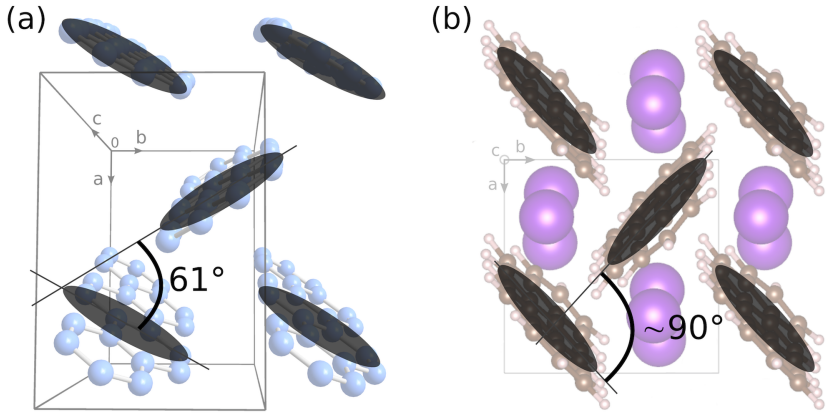

Figure 4.22: *Unit cells of pristine picene and K_3picene illustrating the reorientation of the two inequivalent molecules in the unit cell upon K intercalation. The herringbone angle changes from initially* 61° *in (a) to* ∼ 90° *in (b).*

Chap. 4.4.1 this can be attributed to the absence of a homogeneous chemical potential throughout the entire film. Since the effect of K oxidation already occurs for freshly prepared films, $SrTiO_3$ is not an appropriate substrate for investigations of $K_x$picene.

To shortly summarize, in the valence band spectrum of $K_x$picene F_2 gains intensity upon oxidation with a concomitant decrease of F_1 due to the electron transfer from the molecules to the oxygen. Since F_2 does not evolve from the filling of a molecular orbital its origin is completely of extrinsic nature. Note that already without controlled exposure to oxygen the K-doped picene films show a similar behavior owing to the oxygen in the residual gas of the UHV system and the high reactivity of potassium. Hence, special care has to be taken to work as oxygen-free as possible.

4.4.4 Structural relaxation

Besides the features F_1 and F_2, which have been extensively discussed in the previous sections, a third feature, F_3, develops in close proximity of the unreacted HOMO of pristine films. It shall only shortly be covered here. In analogy to other alkali metal-doped organic semiconductors [101, 125] F_3 is assigned to what is called relaxed HOMO, induced by the reorientation of the molecules upon the insertion of K atoms. As proposed by structural calculations [71] the herringbone angle between the two inequivalent molecules in the unit cell opens from the initial 61° to 114° leading to a renormalization of the HOMO energy. In a more recent theoretical study the same authors report a herringbone angle of ∼ 90° upon K insertion [73] which is in perfect agreement with the calculations of Jeschke *et al.* [87]. A sketch of the unit cells of pristine picene and K_3picene is displayed in Fig. 4.22 illustrating the reorientation of the two inequivalent molecules in the unit cell upon K intercalation. The intensity of F_3 increases with doping, while the decreasing (but still visible) contribution of the H and H-1 peaks in Fig. 4.7

reflects the diminishing fraction of uncharged molecules upon doping.

With that, the four major effects occurring in the electronic structure of picene films upon potassium-doping can be unambiguously assigned and are summarized in Tab. 4.2.

Table 4.2: *Major effects appearing in the electronic structure of picene upon K-doping.*

effect	**origin**
spectral weight *above* μ_{exp}	non-equilibrium behavior
x-dependent F_1, but no metallicity	filling of LUMO, electronic correlations
slightly visible F_2	oxidation of K atoms
F_3 for large x	relaxed HOMO

4.5 Lateral homogeneity of K-doping

In Chap. 4.4.1 it became clear that in $K_x$picene the concentration of K atoms is not distributed homogeneously throughout the entire picene film. Instead, it gradually decreases from surface to substrate due to the subsequent evaporation of dopant atoms onto the film. A corresponding sketch and angle-dependent K $2p$ and C $1s$ core level spectra are shown in Fig. 4.9. Besides, it is known from Kambe *et al.* that $K_x$picene only occurs in phases with integer x and that observing the K_1picene phase is unlikely [119]. In this regard, it is of interest to investigate if such kind of phase separation is present in the samples studied here, and if it is a local effect or if larger domains of a fixed phase are formed. From the reported Raman investigations on polycrystalline powder samples by Kambe *et al.* this question can not be solved [119].

Information about the lateral distribution of K atoms can be obtained by photoemission electron microscopy (PEEM) where a core level analysis of the film composition is possible with a spatial resolution in the nanometer regime. The corresponding experiments have been performed at the beamline UE49-PGM-A-SPEEM at the Berliner Elektronensynchrotron (BESSY). For data acquisition an Elmitec PEEM equipped with a photoelectron analyzer was used. For the microscope the spatial resolution was $\Delta x \approx 15\,\mathrm{nm}$, the total energy resolution regarding the spectroscopic experiments was chosen to be $\Delta E = 0.3\,\mathrm{eV}$. All measurements were performed at room temperature.

Besides measuring in photoemission mode, X-ray absorption spectroscopy (XAS) can be used to obtain spatially resolved element specific information. In order to create the XA images shown in this section, the total electron yield was measured with spatial resolution at a fixed excitation energy. Two XA images of a $K_x$picene film ($x \simeq 2$) on SiO_2 for different excitation energies are displayed in Fig. 4.23. Both images cover a field of view of $20\,\mu\mathrm{m}$ in diameter. The applied excitation energies are 270 and

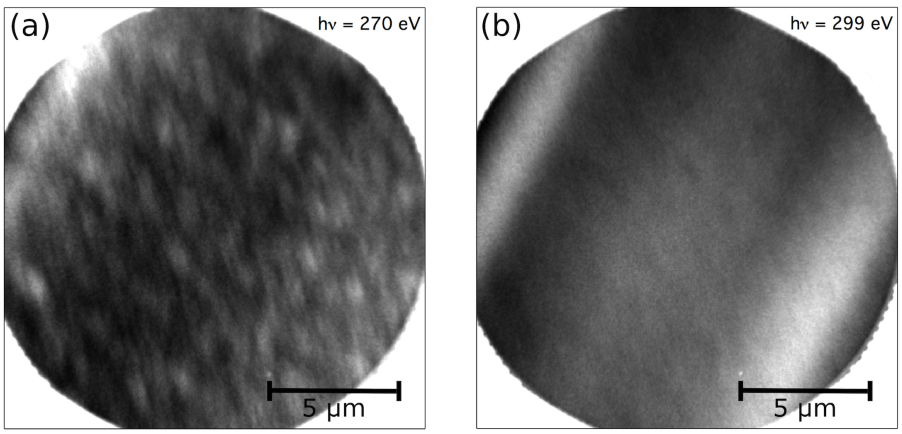

Figure 4.23: *(a) X-ray absorption image of a $K_x$picene film ($x \simeq 2$) on SiO_2 recorded with an excitation energy of 270 eV. The structuring on the picene film is observable. (b) Corresponding image measured at $h\nu = 299$ eV. No structuring is discernable. Bright areas in the images imply high intensity of detected electrons.*

299 eV for (a) and (b), respectively. In Fig. 4.23 (a) a pronounced structuring is observable which directly reflects the 3D growth morphology also observed by AFM (see Chap. 4.2). Since the excitation energy of 270 eV is considerably lower than the binding energy of the C $1s$ ($\sim$ 284 eV) and K $2p$ ($\sim$ 295 and $\sim$ 297 eV for K $2p_{3/2}$ and K $2p_{1/2}$, respectively) core levels, the detected total electron yield originates from the silicon substrate (binding energies of, e.g., Si $2p$ $\sim$ 99 and $\sim$ 100 eV for Si $2p_{3/2}$ and Si $2p_{1/2}$). The signal is attenuated at positions where picene is present on the substrate surface. Thus, the high intensity (bright) areas represent uncovered or sparsely covered parts of the substrate and the dark regions of the image stand for picene islands. This can also be observed in pristine picene films as displayed in Fig. 4.24. It shows a 10 μm field of view XA image measured with an excitation energy of 280 eV, i.e., also below the binding energy of C $1s$. Again, the dark regions in the image reflect the picene islands. In this case, the islands are smaller compared to the doped film owing to a higher deposition rate during growth.

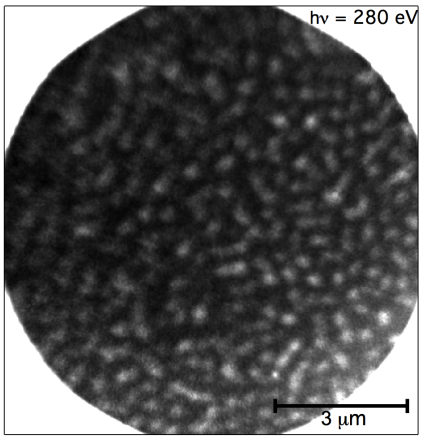

Figure 4.24: *X-ray absorption spectrum of a pristine picene film on SiO_2 measured with an excitation energy of 280 eV.*

Changing the excitation energy to $h\nu = 299$ eV produces the XA image given in Fig. 4.23 (b). Apart from a few exceptions, the structure which was observable for $h\nu = 270$ eV is no longer visible. Since the excitation energy is now equal to the binding energy of potassium, the measured inten-

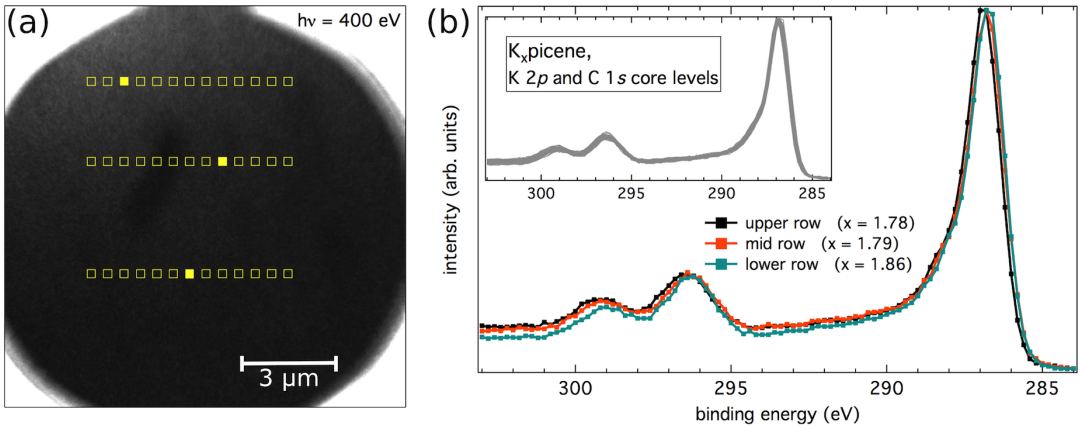

Figure 4.25: *(a) Photoemission electron microscopy image of $K_x$picene recorded for electrons with a kinetic energy of 97 eV (excitation energy 400 eV). The yellow squares indicate areas, for which the spectra are shown in (b). (b) K 2p and C 1s core level spectra for one selected square of each row in (a) indicated by the filled square. In the inset spectra for all squares are plotted.*

sity mainly results from the potassium and carbon core levels. Homogeneous intensity thus implies a basically homogeneous lateral distribution of K atoms. Note that the bright streaks in Fig. 4.23 (b) are not intrinsic but caused by the apertures of the microscope.

The evidence of a laterally homogeneous K concentration from XAS can be strengthened by the use of spatially resolved photoemission. Figure 4.25 (a) shows a 15 μm field of view PEEM image measured with an excitation energy of 400 eV (the image has been taken for electrons with a kinetic energy of 97 eV). For the following analysis the electron kinetic energy range $97 - 116$ eV has been scanned. For each energy step one image as shown in Fig. 4.25 (a) has been recorded. To learn about the composition of the films depending on the position on the sample, the images have been fractionalized into small squares with an area of $\sim 300 \times 300\,\mathrm{nm}^2$. For each square a spectrum has been generated to determine x from the K 2p and C 1s core levels. To give a few examples, the spectra obtained for the yellow squares in Fig. 4.25 (a) are plotted in the inset of panel (b) in the same figure. All spectra yield a similar K concentration with small deviations of $< 10\,\%$. The average x adds up to (1.81 ± 0.16). Representative for all analyzed positions on the sample, one spectrum of each row of yellow squares depicted in the PEEM image is plotted in Fig. 4.25 (b). Here, the similarity of the spectra becomes obvious. Conclusively, the results from PEEM also point towards a homogeneous *lateral* distribution of K atoms over the film.

At first glance, a homogenous K concentration contradicts the effect of phase separation as observed by Kambe *et al.* and discussed in Chap. 4.4.2. However, the phase separation in the films studied here is assumed to occur on a microscopic scale – only in the range of one or a few molecules – and cannot be resolved by the PEEM instrument.

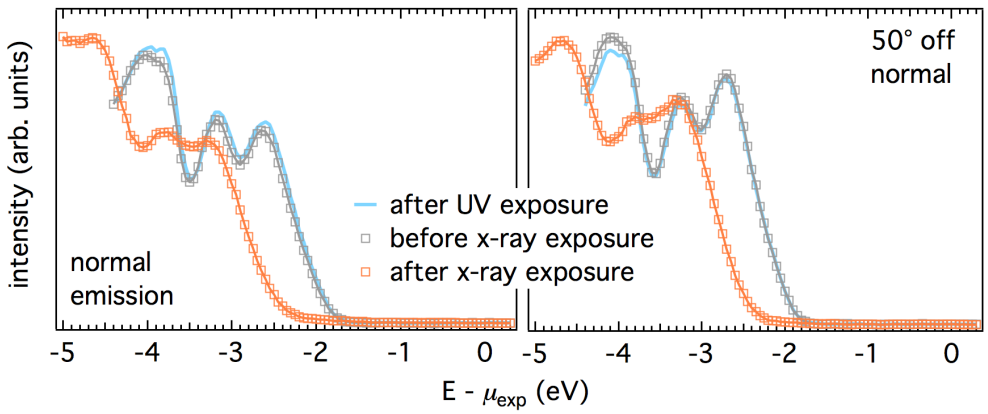

Figure 4.26: *HOMO region photoemission spectra of pristine picene in normal emission and 50° off normal emission measurement geometry before and after 60-minute exposure to X-ray radiation ($h\nu = 1486.6\,eV$). Furthermore, spectra of pristine picene only irradiated by UV light are shown for comparison.*

In any case, one should handle the results of the PEEM measurements with care. Two effects could play a crucial role leading to a misinterpretation of the data. Firstly, the base pressure in the UHV system hosting the microscope was only $\sim 1 \cdot 10^{-8}$ mbar and the films showed a high peak intensity of the O 1*s* core level in a XPS survey spectrum recorded before finishing the measurements. Hence, it is conceivable that a homogeneous potassium oxide film formed on the sample surface during the measurements leading to the observed PEEM images. The importance of oxygen in the residual gas has been discussed in detail in Chap. 4.4.3. Secondly, the exposure to the highly brilliant synchrotron radiation turned out to strongly influence the appearance of the investigated samples. This poses the question to which extent also the electronic structure changes upon exposure to irradiation in the X-ray regime and how large this effect is using a home lab X-ray source. Thus, it will be discussed in the next section.

4.6 Influence of irradiation

The subject of this section is the influence of photon irradiation on pristine and K-doped picene films. Contrary to the brilliant synchrotron radiation used for the experiments illustrated in Chap. 4.5, here, radiation generated by standard lab sources, i.e., X-ray tube and UV-lamp, is considered.

In the case of pristine picene, no noteworthy modifications in the electronic structure could be observed upon irradiation with UV light from a He gas discharge lamp (see Fig. 4.26). The spectra remain unchanged, also over long measurement periods (> 60 min). The situation is different for the exposure of the samples to X-rays. Its influence on the shape of the photoemission spectrum is displayed in Fig. 4.26 for mea-

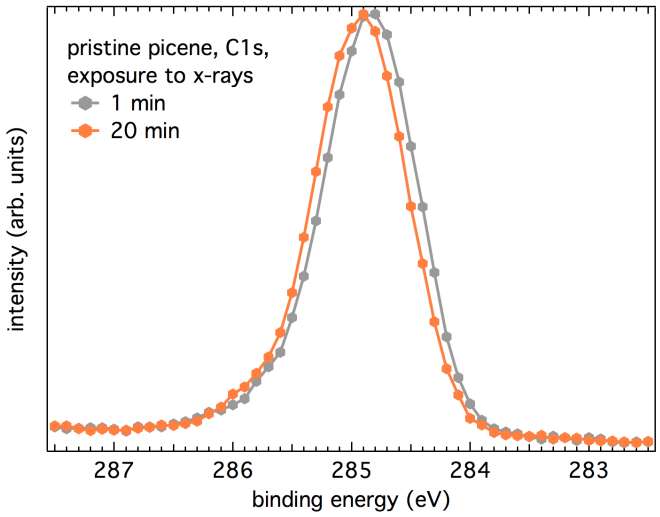

Figure 4.27: *C 1s core level spectrum of pristine picene at the beginning (gray curve) and the end of a 20 min measurement (orange curve). The spectrum exhibits a shift of* ~ 0.1 *eV to higher binding energies.*

surements in normal emission and 50° off normal emission, respectively. For each measurement geometry, one spectrum of freshly prepared picene is plotted in gray and a spectrum for picene irradiated with X-rays for ~ 60 min in orange. The main observations are a shift of the whole spectrum by 0.65 eV to higher binding energies as well as a broadening of the HOMO features, getting smeared out and losing the pronounced structure of the initially measured spectra. Furthermore, a slight increase of the background owing to inelastically scattered photoelectrons can be observed. The origin of the latter two effects cannot be completely fixed but is most probably given by the occurrence of chemical reactions like cross-linking or breaking of bonds in picene, leading to a loss of π-conjugated character of the molecules and a modification of the chemical nature of the sample [46, 47]. Although these effects are photon-induced, scattered photoelectrons and electrons from the secondary electron background are responsible for damaging the molecules [126, 127]. The cause of the occurring shift in the spectra might be either a change in the work function or ionization potential or just charging of the films due to the ejection of electrons [47].

Not only the valence band is affected by the irradiation, also in the C 1*s* core level non-negligible effects can be noticed. As shown in Fig. 4.27, the exposure of a pristine picene film to X-rays for 20 min leads to a slight shift of the C 1*s* core level by ~ 0.1 eV. However, the FWHM remains constant at $\Delta E = 1$eV. Thus, also for the core level, the shift can be ascribed to possible changes in the work function or ionization potential or positive charging of the film [47]. The difference in the shift between valence band and core level (0.65 eV vs. 0.1 eV) might have two different causes. Either it is due to the different probing depths given by the excitation energies of the respective measurement method.

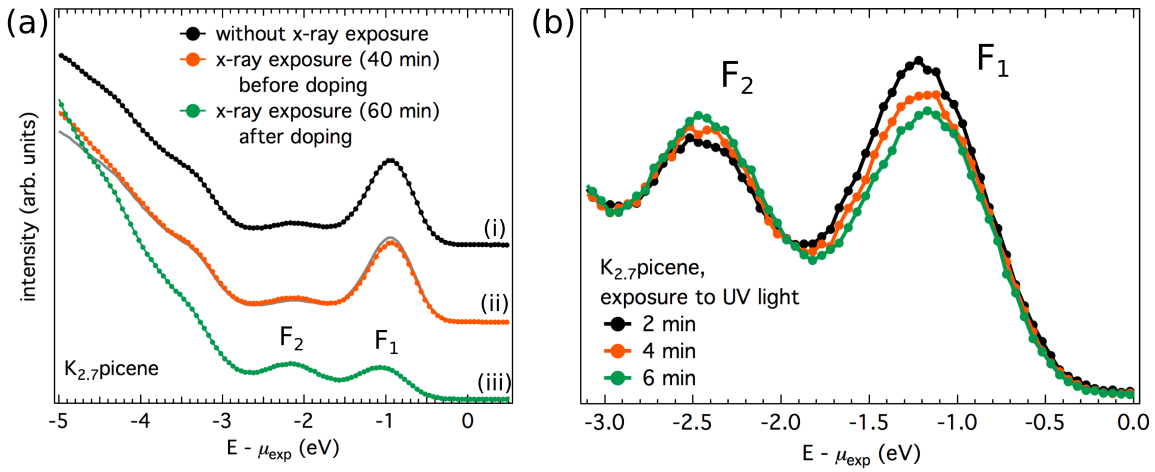

Figure 4.28: *(a) Valence band spectra of $K_{2.7}$picene recorded on different spots on the sample illustrating the influence of X-ray radiation on the electronic structure. (b) Time dependent changes in the electronic structure upon exposure to UV radiation. In both cases the influence of irradiation is manifested in the redistribution of spectral weight from F_1 to F_2.*

In XPS, more layers can contribute to a charge balance and thus counteract a stronger charging. Or, exposure to X-rays during the measurement of the first spectrum has sufficient influence such that most of the damaging process already happened. Note that these photon-induced changes are irreversible. The observed photoemission spectrum of the pristine film does not recover when the sample is shielded from the X-rays for a certain time.

Turning to $K_x$picene, the observed influence of irradiation is even stronger. Both, X-rays and UV light now visibly affect the electronic structure. The impact of X-rays on the valence band structure is illustrated in Fig. 4.28 (a). Typical valence band spectra are shown, each measured on a different spot of the same sample. Curve (i) represents the spectrum of a freshly grown picene film subsequently doped with potassium. All common features can be observed, i.e., in particular, already a small amount of potassium has been oxidized. In case of curve (ii) the pristine film has been irradiated with X-rays for 40 min prior to doping. Apart from small deviations both spectra are very similar. For a better comparison the topmost spectrum is again plotted behind curve (ii). The inelastic background is larger and also the film is slightly more oxidized at this position which can be seen by the redistribution of spectral weight from F_1 to F_2. If the film gets exposed to X-ray radiation for 60 min after the doping process, the corresponding valence band spectrum is shaped like curve (iii) in Fig. 4.28 (a). Here, the two main effects become obvious. While F_1 loses the majority of its spectral weight, F_2 gains in intensity implying a strongly oxidized spot of the film. Furthermore, the secondary electron background dramatically increases.

Similar behavior, i.e., a redistribution of spectral weight from F_1 to F_2 can be observed

upon irradiation of the $K_x$picene samples with UV light. Figure 4.28 (b) displays three spectra recorded in a time-dependent experiment. It is clearly visible that *during* the measurement the spectra change on a timescale of minutes in terms of a decrease of the intensity of F_1 with a concomitant increase of the intensity of F_2, again reflecting the partial oxidation of K atoms. In contrast to pristine picene the exposure to X-rays has no visible effect on the core levels for $K_x$picene.

In summary, with regard to the irradiation of $K_x$picene with X-ray or UV light the electronic structure discernibly depends on the sample history. X-rays already influence the electronic structure of pristine picene whereas UV light has no appreciable effect. For the case of previously irradiated samples doped with potassium, the consequence of radiation damage is also visible in the electronic structure of K-intercalated picene. Furthermore, X-rays as well as UV light directly affect the valence band of $K_x$picene in terms of expediting the oxidation of K atoms (photon-assisted oxidation). Hence, utmost caution is necessary in interpreting photoemission spectra if not the complete sample history is known. The K concentration is no longer a measure of the filling of F_1, since the assumption of the transfer of each K 4*s* electron to the adjacent picene molecule loses its justification. Besides, long and non-essential exposure to X-ray and UV radiation should be avoided. To exclude radiation damage and photon-assisted oxidation in the samples which are the basis for discussion in the previous chapters, all valence band spectra have been recorded from freshly prepared and subsequently doped films using UV light.

4.7 Na_xpicene and Cs_xpicene

In the major part of this thesis, potassium has been used to achieve doping in picene films. However, also sodium and cesium, which are further alkali metals, easily donate their outer *s*-electron to a neighboring molecule and are thus suitable for doping. Images of the unit cell of Na_xpicene and Cs_xpicene for $x = 1, 2, 3$ are shown in Fig. 4.29 obtained by relaxation within DFT [87]. In general, both structures are similar and essentially do not differ from the $K_x$picene structure introduced in Fig. 4.1 (c). The observed torsion of the molecules for K_1picene and K_2picene is even more distinct for the case of cesium owing to the larger size of the Cs atoms. In Na_xpicene ($x = 1, 2$) the effect is less pronounced. However, here the molecules are slightly bent for $x = 3$ which decreases with increasing atomic mass of the intercalants. The resulting electronic structures from DFT, based on these real space structures are similar to the electronic structures gained from the calculations for $K_x$picene. Again, metallic and semiconducting behavior is expected for $x = 1, 3$ and $x = 2$, respectively.

As elaborately discussed in Chap. 4.4.2 the DFT calculations cannot reveal the true electronic structure of K-doped picene due to the importance of electronic correlations. A similar situation is found here for doping with Na and Cs. As for K-doping, the photoemission spectra of $(Na,Cs)_x$picene films with a concentration x in the range of 1 show

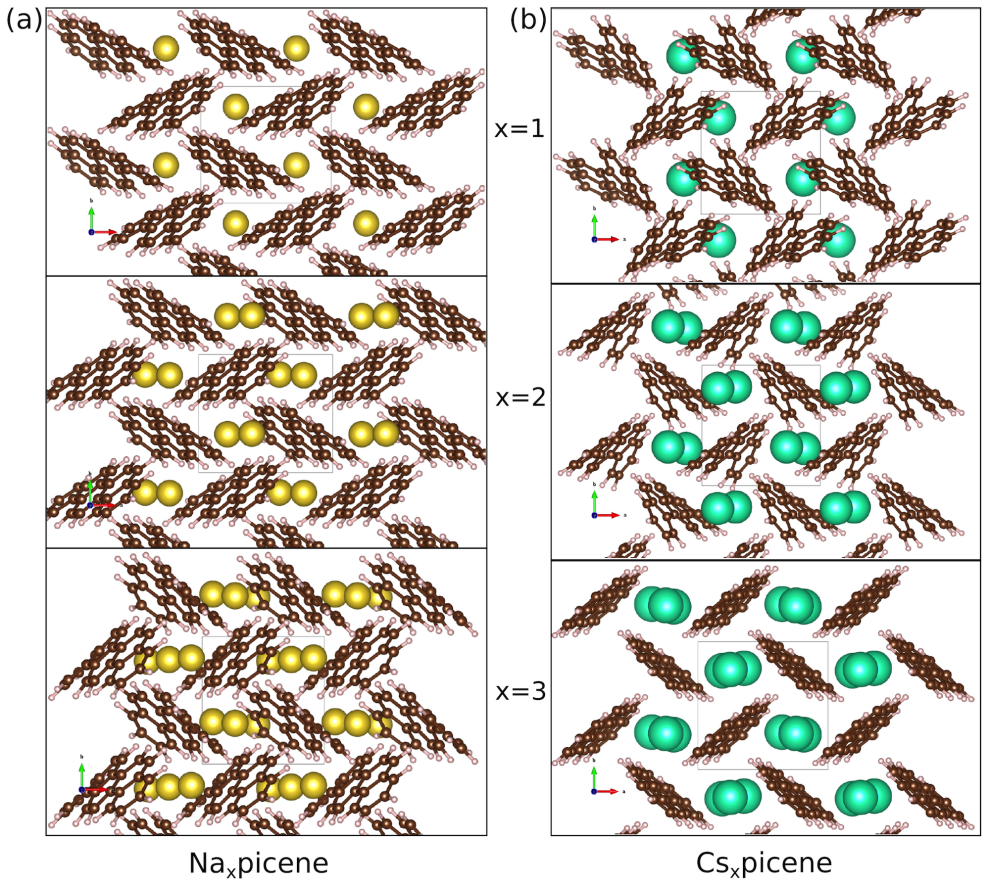

Figure 4.29: *Structures of Na_xpicene (a) and Cs_xpicene (b) for $x = 1, 2, 3$ each. Images from Jeschke et al. [87].*

no metallic Fermi cut-off. Figure 4.30 shows the corresponding valence band spectra. The observable effects in the spectra are essentially similar to all effects reported for $K_x$picene in the previous chapters. Starting with the lowest (red) curve in Fig. 4.30, it represents the spectrum of a $Cs_{0.5}$picene film compared to a spectrum of $Cs_{0.8}$picene (orange curve). Similar to $K_x$picene a new feature appears upon Cs intercalation located at an energy of ~ -1 eV which is ascribed to the filling of the LUMO renormalized by the influence of electronic correlations (denoted F_1 according to the $K_x$picene spectra). The shift of the $Cs_{0.5}$picene spectrum to lower binding energies originates in the formation of a non-equilibrium situation as described in Chap. 4.4.1. Like potassium, also cesium diffuses slowly into the picene films leading to a Cs concentration gradient. Due to the interplay of non-equilibrium and concentration gradient the chemical potential at the surface of the doped film cannot be identified. Thus, the observed peak apparently has a different energy position. For a higher Cs concentration of $x = 1.4$ (blue curves) F_1 gains in intensity. Besides, the relaxed HOMO, reflected by the formation of F_3, can be identified. Upon storage in the UHV system the appearance and increase of F_2 can

be followed owing to the oxidation of Cs atoms supported by oxygen in the residual gas [122].

Regarding the intercalation with sodium, Na_xpicene behaves slightly different. The corresponding photoemission spectrum is shown in Fig. 4.30 (topmost, black curve). Again, F_1 and F_2 occur in the spectrum whereas the fraction of oxidized Na_xpicene initially is already higher for a low Na concentration compared to $(K,Cs)_x$picene. This points to a stronger oxidation of the Na atoms, which is expected due to the lower oxidation potential of Na [128]. Furthermore, F_3 is less pronounced in the case of Na_xpicene since the molecular reorientation in the unit cell is weaker for smaller intercalant atoms and the HOMO energy gets less renormalized.

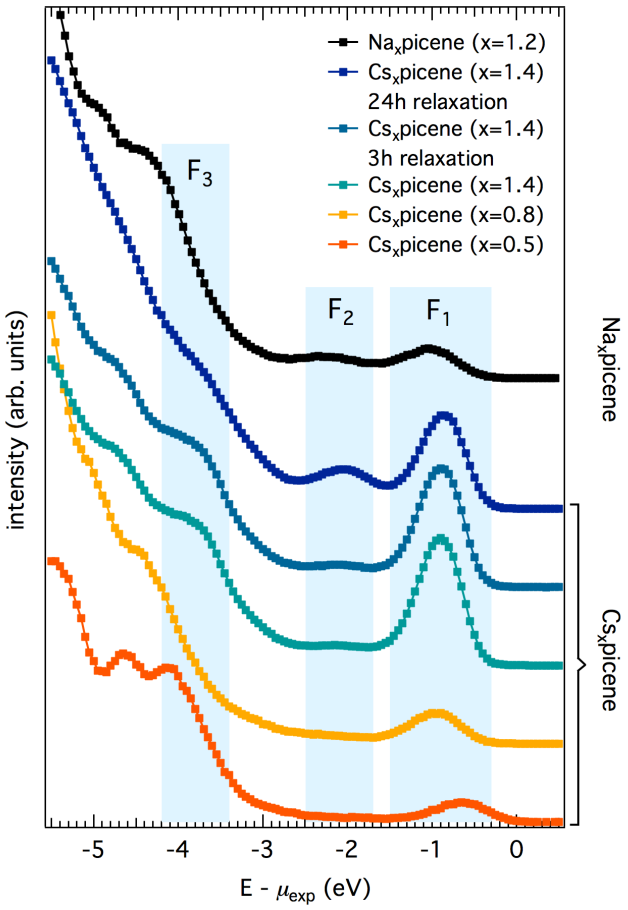

Figure 4.30: *Valence band spectra of picene films doped with Na and Cs, respectively, for various doping concentrations. The topmost curve corresponds to Na_xpicene whereas the other spectra correspond to Cs_xpicene.*

In summary, picene films doped with K, Na, or Cs behave very similar. All interpretations and explanations given in the previous chapters for $K_x$picene can savely be applied for $(Na,Cs)_x$picene.

4.8 Short summary

In order to summarize the chapter about picene, its doped compounds, and the resulting electronic structure, the major outcomes shall be listed here again. As a basis of the investigations, picene films of high structural quality have been fabricated on various substrates. Regarding the electronic structure of the pristine films, the valence band and core level photoemission spectra agree well with what is reported in the literature up to now. Upon doping the pristine picene films with potassium, four interesting phenomena occur in the electronic structure whose origins have been elucidated in the framework of this thesis. Remarkably, not all phenomena stem from intrinsic properties of K-doped picene. However, intrinsic effects are the emergence of a doping-induced photoemission feature in the vicinity of the chemical potential (F_1) and the appearance of a further new feature close to the HOMO (F_3). F_1 can be ascribed to the filling of the LUMO, though, not involving metallicity. Electronic correlations in $K_x$picene lead to the formation of a Mott insulating state for $x = 1, 2, 3$. Owing to phase separation, the insulating behavior is retained for all K concentrations. On the other hand, due to the reorientation of the picene molecules in the lattice upon insertion of dopant atoms, a renormalization of the binding energy of the HOMO is observed. This manifests itself in the incidence of F_3. A third feature appearing in the former HOMO-LUMO gap (F_2) is of purely extrinsic nature. It originates from K oxide, which is formed by the reaction of the K dopants with molecular oxygen in the residual gas of the UHV system. A further extrinsic effect leads to the apparent presence of spectral weight above the reference chemical potential. Considering weakly van der Waals-coupled systems no Fermi level alignment can be established. The interplay between vacuum level alignment and a K concentration gradient then allows the appearance of spectral weight above the chemical potential of the reference system.

Besides, it has been observed that, on the one hand, subsequent K-intercalation leads to a vertical K concentration gradient in picene films. On the other hand, laterally, the doping concentration appears homogeneously distributed over the entire film on a mesoscopic scale, as deduced from spatially resolved photoemission. However, this does not refute the occurrence of phase separation in $K_x$picene which takes place on a microscopic scale. Finally, the utilized UV and particularly X-ray radiation turned out to considerably influence the electronic structure of pristine as well as K-doped picene. Hence, special care has to be taken in conducting photoemission experiments.

5 $K_x$pentacene: An exemplary Mott insulator?

Pentacene, a molecule very similar to the molecule picene introduced in Chap. 4, is one of the favorite materials in the field of flexible electronics. This is owing to the fact that, at low charge carrier density, the *organic* semiconductor pentacene largely behaves like its *inorganic* counterparts like silicon or gallium arsenide [129–131]. Mobilities in the range of 0.3 to 1.6 cm^2/Vs or even higher [132, 133], which are impressive values for an organic semiconductor, make it a promising candidate to replace Si-based devices like, e.g., transistors in future electronics [134, 135]. But not only potential applications attract the interest on pentacene, also in basic research it represents a debated topic. One important aspect is the electronic structure. For organic crystals, in the low charge carrier density regime the electrons are considered as non-interacting particles. However, electron-electron interaction can play a crucial role in organic semiconductors, particularly upon electron doping. Due to the very narrow band width, W, of $\sim 0.5\,\mathrm{eV}$ already small on-molecule Coulomb repulsion energies, U, of $1 - 1.5\,\mathrm{eV}$ suffice to generate the base for electronic correlations [136, 137]. Charge transfer salts and alkali metal fullerides are only two examples for which the role of electronic correlations has been lively discussed [113, 138]. In 2009, Craciun *et al.* reported transport measurements revealing a metal-to-insulator transition in potassium-intercalated pentacene films depending on the amount of intercalated K atoms [15]. Conductivity first increases with increasing potassium amount and then suffers a sudden drop at a K concentration of exactly one K atom per pentacene molecule. According to their interpretation, for this particular composition half filling is achieved and the system is driven into a Mott-insulating state.

The goal of this chapter is to elucidate the electronic structure of potassium-intercalated pentacene films in a wide range of K concentrations. First, the films have been structurally characterized using AFM and XRD to prove their high quality. The next part deals with the investigation of pristine pentacene films by means of XPS and UPS. In the main section the impact of K-doping on the electronic structure is investigated.

5.1 From the parent compound to $K_x$pentacene

All investigations following in the next sections of this thesis are based on the parent compound pentacene. Pentacene ($C_{22}H_{14}$, abbreviated Pn in the following) is a further type of *nano-graphene* and very similar to picene. Likewise, it is a planar π-conjugated,

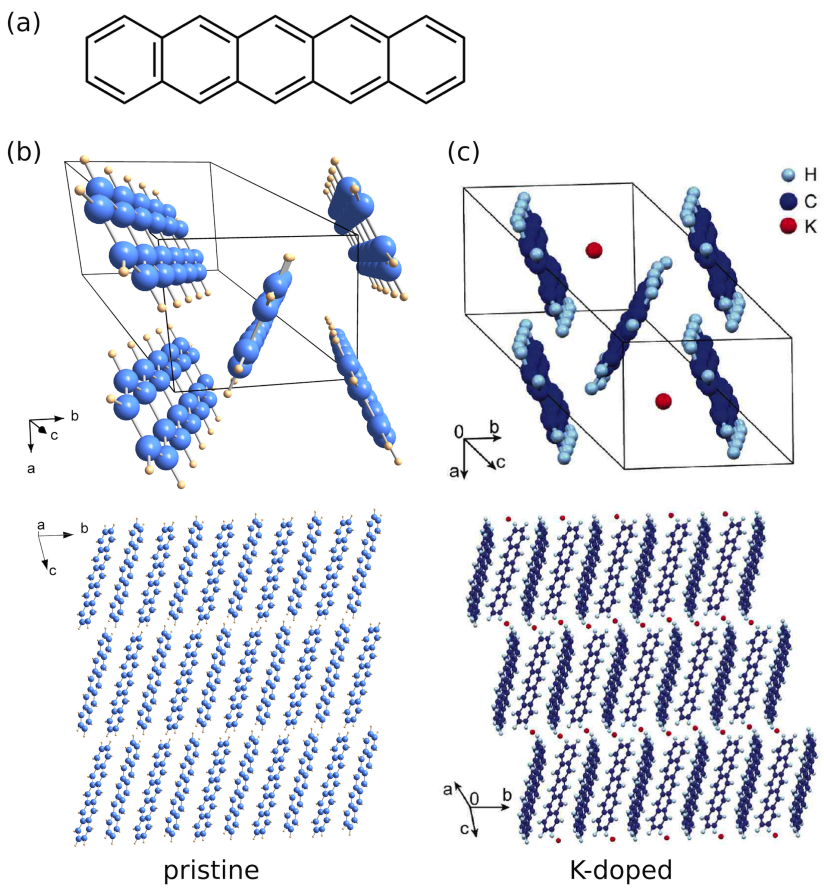

Figure 5.1: *(a) Structural formula of a single pentacene molecule. (b) Unit cell structure and layer formation of pristine pentacene crystals or thin films. (c) Corresponding unit cell structure and layer formation of K-intercalated pentacene. In thin films, the molecules grow along the unit cell c-axis. The images in the lower panels are thus considered as side view. Images in (c) are reprinted from Ref. 15 with permission from M. Craciun. Copyright (2013) by The American Physical Society.*

aromatic molecule composed of five benzene rings as sketched in Fig. 5.1 (a). Contrary to picene, in Pn the rings are arranged linearly forming a zig-zag edge. Building up a single crystal, the molecules crystallize in a triclinic structure (space group $P\bar{1}$) with the lattice parameters $a = 6.266\,\text{Å}$, $b = 7.775\,\text{Å}$, and $c = 14.530\,\text{Å}$ as well as $\alpha = 76.475°$, $\beta = 87.682°$, and $\gamma = 84.684°$ [139]. Like most of the aromatic molecules, Pn arranges in a herringbone fashion resulting in a unit cell containing two inequivalent Pn molecules [88]. A sketch of the unit cell is shown in Fig. 5.1 (b) together with a side view of the packing motif of Pn. The displayed structure is, however, only valid for single crystals and thin films grown in standing mode, i.e., in the case when the molecule-molecule interaction overweighs the molecule-substrate interaction. For, e.g., metal substrates the molecules lay down and get covalently bond to the surface [140].

The resulting structure drastically deviates from the structure shown here. Note that, exceeding a certain number of layers, the molecules continue growing in standing mode also on metals [141]. Since all films studied within this thesis have been grown on substrates which fulfill the above condition for growth in standing mode (see next chapter), only the case of upright standing molecules shall be considered here.

In contrast to picene, different structural phases exist for Pn single crystals and Pn thin films. They can basically be distinguished by the tilting angle of the long molecular axis with respect to the substrate surface normal, reflected in different c-axis lattice parameters [142]. In general, Pn films growing in standing mode can mainly be composed of two phases. (i) The bulk phase (α-phase), which is similar to Pn single crystals, but also occurs in thin film growth, and (ii) the thin film phase (β-phase). The latter has a lower density ($\rho_{\text{bulk}} = 1.3\,\text{g/cm}^3$ vs. $\rho_{\text{film}} = 1.0\,\text{g/cm}^3$) and the molecules are less tilted with respect to the surface normal. For the different phases the unit cell c-axis parameters are $c_\alpha = 14.5\,\text{Å}$ and $c_\beta = 15.4\,\text{Å}$, reflecting the different tilting angles of the $\sim 16\,\text{Å}$ long Pn molecules [143]. Crystallized Pn forms an organic semiconductor with an optical gap of $E_{\text{opt}} = 1.8\,\text{eV}$ [144] and a transport gap of $E_{\text{gap}} = 2.2\,\text{eV}$ [21, 145, 146].

For K-intercalated Pn (K_xPn, x = K concentration) no structural data have been reported so far. However, it is well known that, upon intercalation with various alkali metals, the herringbone arrangement of the Pn molecules is preserved and the additional atoms are placed between the molecular layers (interlayer insertion) [15, 147–150]. This results in an expansion of the c-axis lattice parameter of the order of the intercalated ion radii [15]. The a and b lattice constants are only marginally affected. DFT-based calculations provide the following lattice parameters for K_1Pn: $a = 6.239\,\text{Å}$, $b = 7.636\,\text{Å}$, and $c = 15.682\,\text{Å}$ as well as $\alpha = 76.98°$, $\beta = 88.14°$, and $\gamma = 84.42°$ [15]. As expected, except for the c-axis parameter, the lattice constants remain largely unaffected. The corresponding unit cell as well as the side view of the molecular layers are displayed in Fig. 5.1 (c).

5.2 Growth and structure of pristine pentacene films

Concerning the film growth, all growth details of picene described in Chap. 4.2 are also valid for Pn. For Pn, the main motivation for using *in vacuo* grown thin films is the interest in improving the film quality in view of the application in thin film transistors. Moreover, the difficulty of K_xPn single crystal growth due to the high reactivity of potassium again make the use of thin films preferable. In vacuum, any contact to ambient air can be avoided between the film growth, the intercalation process, and the investigation by means of photoelectron spectroscopy.

Hence, Pn films have been fabricated on various substrates, which are natively oxidized silicon (denoted **SiO_2**), the hydrogen-terminated surface of silicon (**Si-H**), strontium titanate (**$SrTiO_3$**) and zinc oxide (**ZnO**) (for details of substrate preparation see A.1). Furthermore, Pn films have been prepared on Bismuth-templates on Si(111)-7 × 7, for

which no detailed characterization data are available. For thin film growth purified Pn powder was evaporated from a commercial effusion cell (Tectra) in a separated chamber at UHV conditions. Here, the pressure was kept below 5×10^{-9} mbar. Deposition was carried out at room temperature. Subsequently, potassium was evaporated onto the films from a current heated commercial SAES getter source in UHV at a base pressure of $\leq 5 \times 10^{-10}$ mbar to intercalate the films with potassium. For imaging the surface morphology of the pristine Pn films two types of scanning probe microscopes were used. On the one hand, it was an *ex situ* Veeco AFM operated in non-contact tapping mode was. On the other hand, it was an *in situ* Omicron VT SPM (variable temperature scanning probe microscope) with an oscillating needle sensor. Furthermore, diffractograms were recorded by means of XRD in ambient atmosphere using X-rays from a Cu K_α source with a wavelength of 1.5418 Å in a simple $\theta - 2\theta$ geometry. Additionally, low energy electron diffraction (LEED) was employed using an Omicron LEED optics in UHV.

Beginning with the surface morphology, Figs. 5.2 (a)-(d) show AFM images of pristine Pn films grown on SiO_2 (a), Si-H (b), $SrTiO_3$ (c), and ZnO (d). The displayed cutouts have a size of $1.5 \times 1.5\,\mu m^2$, $2 \times 2\,\mu m^2$, $5 \times 5\,\mu m^2$, and $1.5 \times 1.5\,\mu m^2$, respectively. All films have a nominal thickness of $25 - 30$ nm, deduced from monitoring the film growth with a quartz crystal microbalance (QCM), and exhibit a coverage of $\sim 95\,\%$ each. It is clearly visible that the growth behavior of Pn on SiO_2, Si-H, and ZnO is very similar. As expected for inert substrates, Pn nucleates in islands, which partially coalesce resulting in grain boundaries between different domains. The observed surface morphology agrees well with data reported in the literature [151–155]. On all substrates the islands have a size ranging from 500 nm to 1 μm showing a slight trend to a rhombical shape. While this points to crystalline ordering of the molecules *within* the islands, the overall film appears to be azimuthally disordered. The arbitrary rotation of the islands in the (a, b)-plane is directly reflected in the LEED pattern in case of a Pn film grown on ZnO. Two diffractograms recorded at electron energies of $E = 16.4$ eV and 26.1 eV are displayed in Fig. 5.2 (f). Instead of diffraction spots, as observed for crystalline samples with high symmetry, rings appear in the patterns. This is owing to the superposition of diffraction spots of all arbitrarily rotated islands within the area of the electron beam ($\varnothing \approx 1$ mm). Quantitative inspection allows the assumption that the circles with high intensity in each image may be attributed to the (2,2) diffraction spot and the low intensity circle in the $E = 26.1$ eV image might originate from the (0,2) diffraction spot. Note that, in general, electron diffraction experiments on organic systems are very delicate to handle, since the incoming electron beam strongly influences the electronic structure. Origin of the occurring damages are chemical reactions like cross-linking or breaking of bonds, leading to a loss of π-conjugated character of the molecules and a modification of the chemical nature of the sample [46, 47] (see discussion for picene in Chap. 4.6).

For Pn films grown on $SrTiO_3$, the film properties are basically similar to the previously presented films. However, on $SrTiO_3$, Pn tends to form larger, dendrite-like islands with island sizes exceeding a few microns. Altogether, on all films the roughness on the

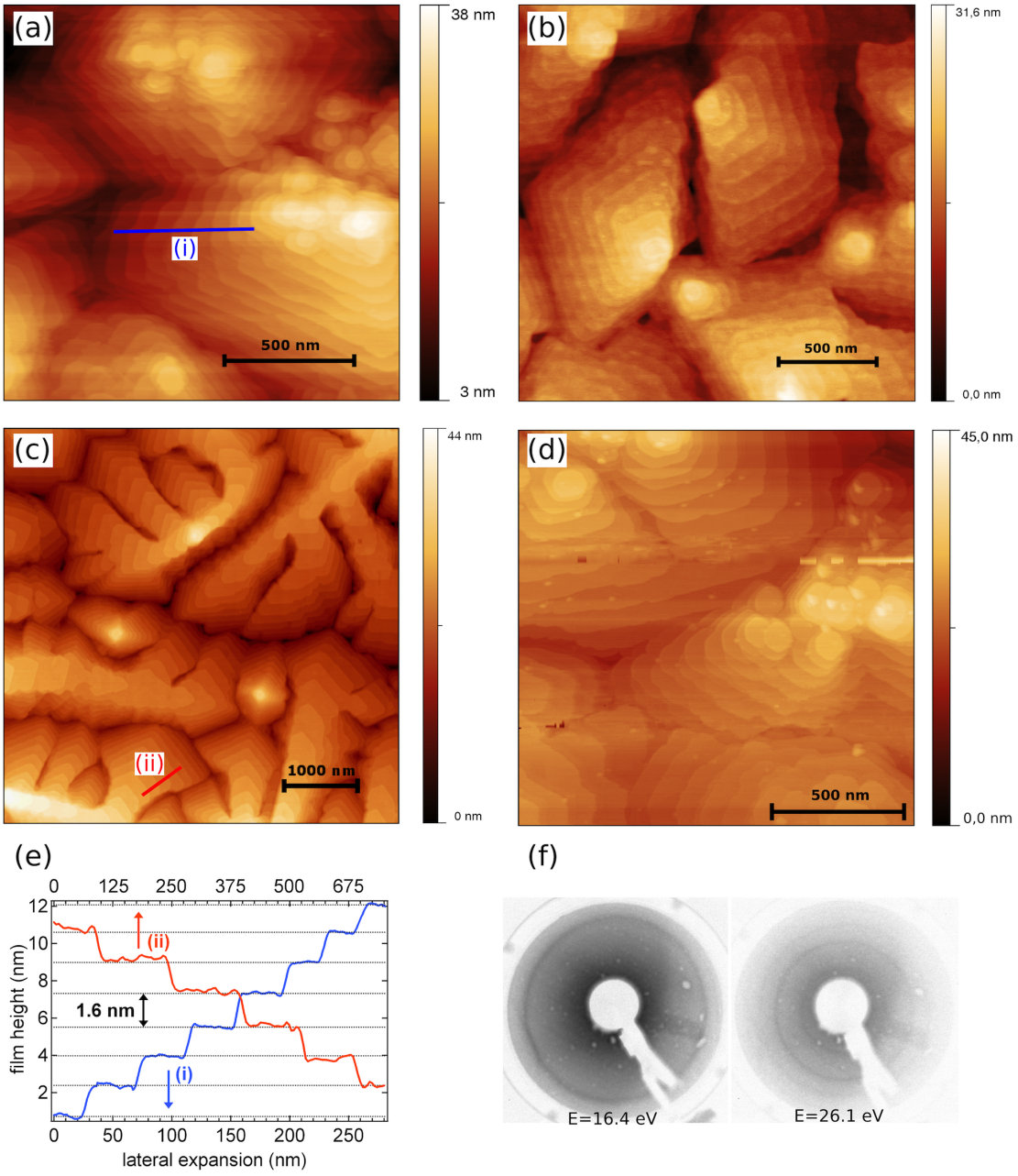

Figure 5.2: *Surface morphology images from AFM and diffractograms from LEED of pristine Pn films grown on different substrates. (a) $1.5 \times 1.5\,\mu m^2$ AFM image of Pn on SiO_2. (b) $2 \times 2\,\mu m^2$ AFM image of Pn on Si-H. (c) $5 \times 5\,\mu m^2$ AFM image of Pn on $SrTiO_3$. (d) $1.5 \times 1.5\,\mu m^2$ AFM image of Pn on ZnO. (e) Corresponding line profiles indicated by the lines in (a) and (c). (f) LEED patterns of a Pn film on ZnO. For details see text.*

terraces remains below 0.1 nm, thus one can assume that the terraces are molecularly flat. Considering the surface morphology images of the Pn films grown on the different substrates combined with the film coverage leads to effective average film thicknesses of $\sim$ 20, 15, 15, and 25 nm for SiO_2, Si-H, $SrTiO_3$, and ZnO, respectively. To do so, in particular the height distributions in the films have been taken into account (find details of the height distributions in A.2). Similar to picene, the average film thickness of Pn partially drastically deviates from the nominal value obtained from QCM moni-toring depending on the substrates. Again, this may be due to the different sticking coefficients for different substrates not included in the considerations. Thus, the nominal QCM values have to be handled with care. Usually, they only give a rough estimate of the film thickness.

Along the *c*-axis, on all substrates the molecules aggregate in standing mode, reflected in the line profiles (i) and (ii) in Fig. 5.2 (e). The line profiles trace the surfaces of the Pn films on SiO_2 and $SrTiO_3$ along the blue and red line, respectively, as indicated in (a) and (c). The well-resolved single steps have a height of $\sim$ 16 Å, which, within the accuracy of the utilized AFM, corresponds to the *c*-axis lattice parameter of Pn thin films. Growth in standing mode can also be deduced from X-ray diffraction. Figure 5.3 (a) displays the diffraction data of three Pn films on Si-H (1), SiO_2 (2), and $SrTiO_3$ (3). For each film the (001) and (002) Bragg peaks are shown. Using the Bragg relation one obtains a lattice spacing of (15.4 ± 0.1) Å for each film from the (002) peak, in perfect agreement with the value for the β-phase. Additional features can be observed in the $\theta - 2\theta$-scan of the film grown on Si-H, corresponding to the Bragg reflection of a film component with a lattice spacing of (14.4 ± 0.1) Å. Thus, it can be assigned to the α-phase, which partially occurs in thicker films. Besides Bragg reflectivity, rocking curves were measured, yielding a narrow rocking width in the range of $\Delta = 0.04°$. A rocking curve recorded from Pn on Si-H is plotted in Fig. 5.3 (b). The narrow rocking width manifests

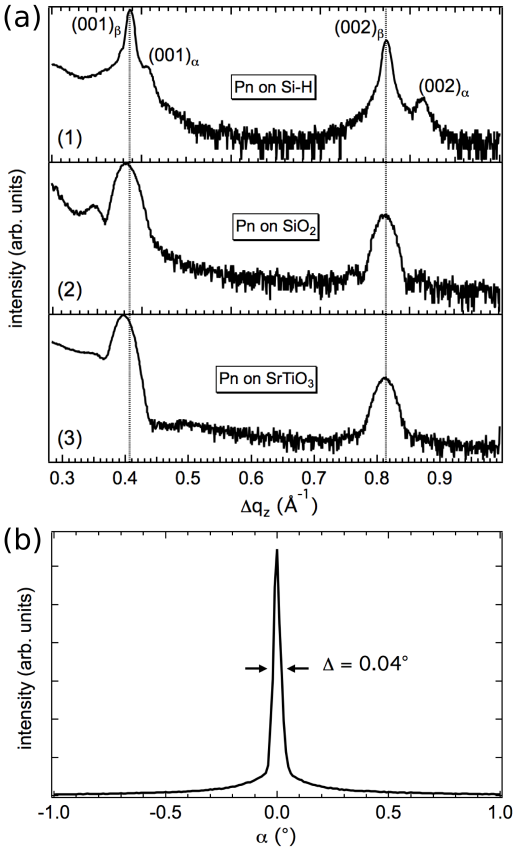

Figure 5.3: *(a) X-ray diffractograms of Pn films on Si-H (1), SiO_2 (2), and $SrTiO_3$ (3). Each diffractogram shows the (001) and (002) Bragg peaks. (b) Rocking curve of a Pn film on Si-H. Note the narrow rocking width of only 0.04°.*

high order along the c-direction with only a small tilting of $\pm 0.02°$. The non-negligible background in the rocking curve arises from diffuse scattering due to screw dislocations [156].

Conclusively, pentacene essentially behaves the same on all used substrates, forming stepped islands of 500 nm to 1 μm in size, which are azimuthally rotated with respect to the other islands. Out of plane, the films are highly ordered with a step height of ~ 16 Å, corresponding to the length of an upright standing Pn molecule. The films are in good agreement with the literature and, thus, are appropriate for investigations using photoelectron spectroscopy.

5.3 Electronic structure of pristine pentacene films

The following sections will cover the investigations on the electronic structure of Pn and the evolution of this electronic structure upon intercalation with potassium by means of photoelectron spectroscopy. To this end, home-laboratory equipment containing a monochromatized X-ray source (Al K_α,1486.6 eV) and a He gas discharge lamp (He I, 21.2 eV) were used for core level and valence band analysis, respectively. Before discussing the influence of K-intercalation on the electronic structure of Pn, it is helpful to start with a look at the electronic structure of the pristine system. Hence, firstly, a short insight into previous valence band photoemission studies from the literature will be given, followed by the results gained within the framework of this thesis. Topping off this section, the relevant photoemission core levels will be considered.

5.3.1 Aspects from the literature

In order to learn about the electronic structure of a certain system, it can be helpful to have predictive calculations from, e.g., DFT revealing the band structure. From this band structure, the DOS can be obtained which, in turn, is comparable to angle-integrated photoemission data. Exemplary calculations of the band structure of Pn in the thin film phase are displayed in Fig. 5.4 (a). Here, Γ, X, Y, Z, M, and M' are the respective high symmetry points of the triclinic lattice. In contrast to an ideal semiconductor for which the Fermi energy E_F is located in the middle of the band gap, in this case E_F has been set to the valence band maximum with $E = 0$ eV. Moving away from the Γ-point, the calculations reveal a considerable dispersion in most of the directions in k-space. Note that in Γ-Z direction no dispersion is observable. Γ-Z corresponds to the direction of molecular stacking in real space where only van der Waals-interactions play a role. Each pair of bands is derived from one molecular orbital reflecting the existence of two inequivalent Pn molecules in the unit cell. In the defined energy range one can identify the HOMO-1, HOMO, LUMO, and LUMO+1 derived bands with the two bands in the vicinity of the Fermi energy representing the HOMO bands. Note that the calculated band gap is strongly underestimated, which is a well-

known shortcoming of DFT. Contrary to the experimental value of $E_{\mathrm{gap}} = 2.2\,\mathrm{eV}$ the calculations provide a band gap of $< 1\,\mathrm{eV}$ [157, 158].

For a better comparison with the experiment, the k-integrated DOS (convolved with a 0.2 eV Gaussian) of Pn in the thin film phase is plotted in panel (i) of Fig. 5.4 (b). Besides, the k-integrated DOS of Pn in the bulk phase is displayed in (ii). The large splitting of the two contributing bands manifests itself in a broad two-peak structure with an energy separation of $\Delta E \simeq 0.4\,\mathrm{eV}$ between the two peaks. In the band structure of bulk phase Pn the dispersion is much less pronounced, reflected in a smaller energy separation between the single peaks of only $\Delta E \simeq 0.2\,\mathrm{eV}$.

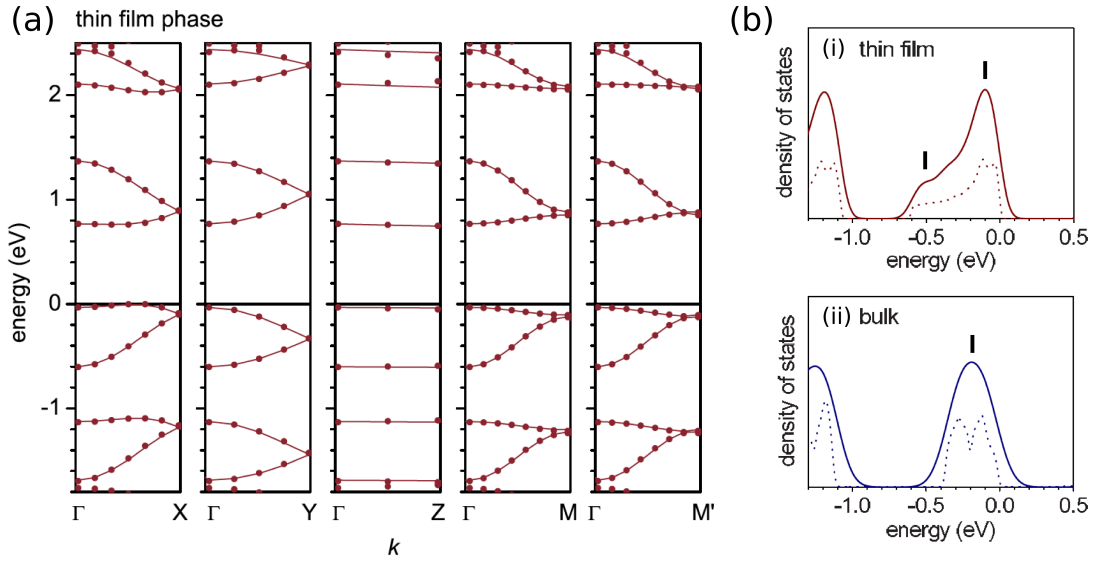

Figure 5.4: *(a) Calculated band structure of Pn in the thin film phase from DFT (in GGA with PBE functional). (b) Resulting DOS (i) of the thin film phase and (ii) of the bulk phase for comparison. The calculated points (dotted lines) are convolved with a Gaussian function of 0.2 eV FWHM (solid lines). The energy separation between the two contributing bands is indicated by the marks. Figures reprinted from Ref. 157 with permission from H. Yoshida. Copyright (2013) by The American Physical Society.*

In order to get a first impression of the photoemission spectra of pristine Pn, Fig. 5.5 shows two examples from the literature [159, 160]. Both illustrate the valence band of pristine Pn grown on oxidized silicon. While Fig. 5.5 (a) displays spectra for different oxygen treatments, in (b) spectra have been recorded for various film thicknesses. Most relevant are in each case the topmost spectra, representing pristine Pn films of 12 nm and 6.4 nm thickness, respectively. Both spectra are in good agreement with the experimental spectra given earlier by Yoshida *et al.* [157] and cover a larger energy interval. The superposition of two peaks claimed by theory can be identified. Additionally, in the bottom curve of the inset in (a) a larger energy range is covered, providing a survey of the whole valence band.

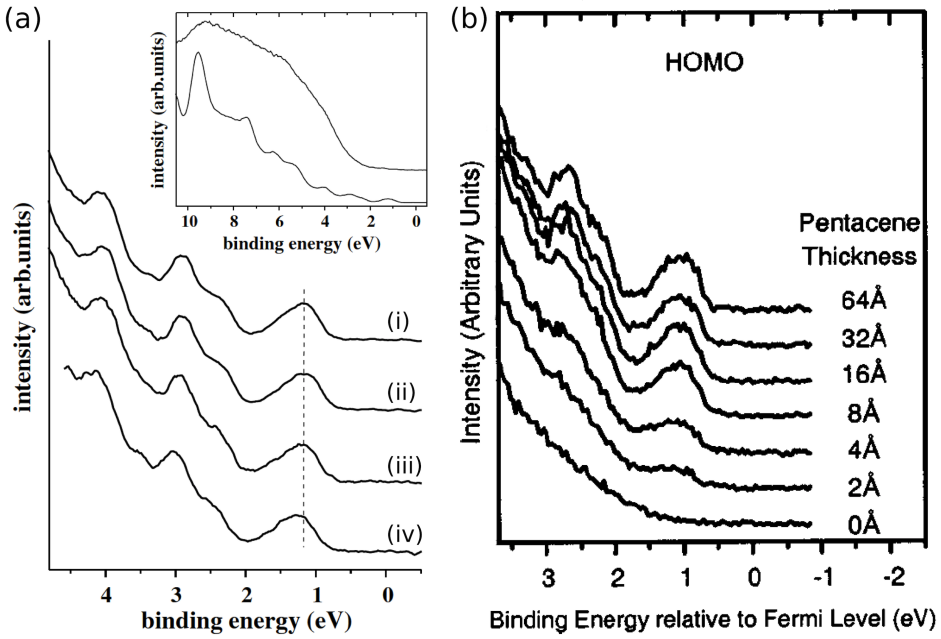

Figure 5.5: *Valence band photoemission spectra of pristine Pn films: (a) Spectra for different oxygen treatment. The relevant spectrum is curve (i) representing a pristine Pn film on SiO_2, the bottom curve in the inset shows a corresponding valence band survey spectrum. Figure reprinted from Ref. 159, Copyright (2013), with permission from Elsevier. (b) Thickness-dependent spectra of pristine Pn on SiO_2. Figure reprinted from Ref. 160, Copyright (2013), with permission from AIP Publishing.*

5.3.2 Valence band photoemission

In the light of the above, this section is dedicated to the photoemission results of pristine Pn films grown on various substrates. Figure 5.6 shows four valence band photoemission spectra (as measured) of Pn films fabricated on Si-H, $SrTiO_3$, ZnO and Bi/Si, respectively. All films have a thickness of $\sim 25 - 30\,\text{nm}$, as described in Chap. 5.2. Note that spectra of films for which SiO_2 was used as a substrate, appear to be identical to the spectra of Pn on Si-H. Concerning the spectral shape, all spectra are in perfect agreement with reported data from the literature [26, 157, 159–163]. Moreover, partly the quality of the spectra even exceeds the quality of previously measured data in terms of statistics and shape. In addition, the valence band survey spectrum displayed in the inset of Fig. 5.6 (a) also agrees well with the literature [see Fig. 5.5 (a)]. Immediately noticeable in Fig. 5.6 (a) is a variation of the exact peak positions depending on the substrate, reflected in a shift of the entire spectrum. This behavior originates from the fact that by deposition of several layers of weakly van der Waals-coupled molecules on any substrate no equilibration of the chemical potential can be established. Instead, the energy level alignment is determined by the vacuum level (see end of Chap. 4.3.2). Hence, depending on the molecular ionization energy and the substrate work function,

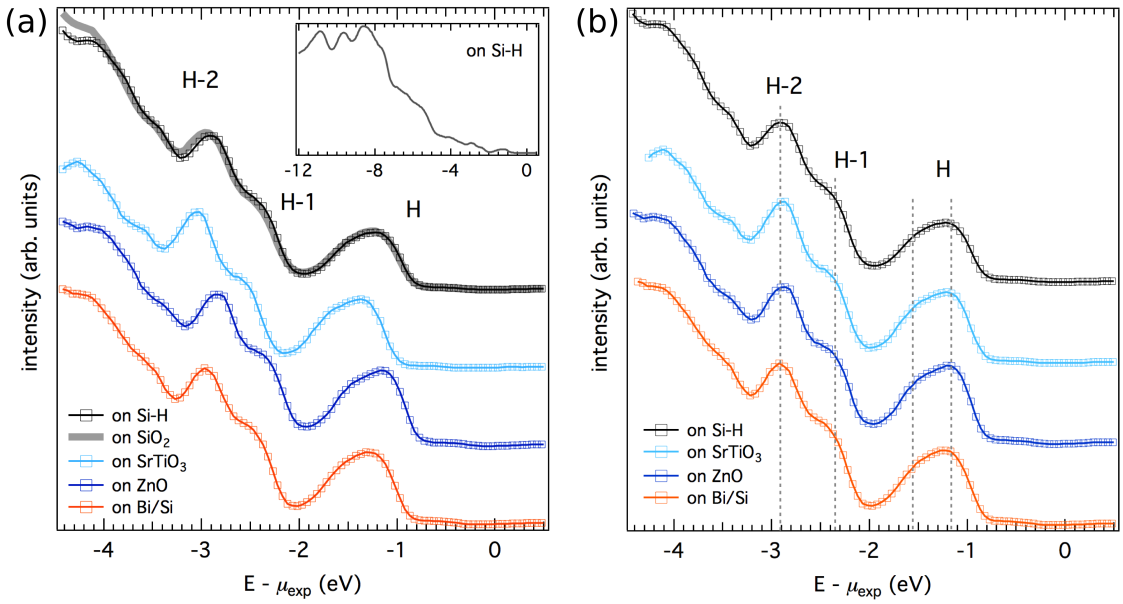

Figure 5.6: *Valence band photoemission spectra of Pn thin films on the substrates Si-H, SiO_2, $SrTiO_3$, ZnO, and Bi/Si. (a) Data as measured. Spectra for Pn on Si-H and SiO_2 are basically identical and plotted on top of each other. The inset shows a valence band survey spectrum of Pn on Si-H over a larger energy range. (b) Data aligned on the peak positions of the Pn on Si-H spectrum (black curve) for better comparison.*

the energetic positions of the molecular orbitals may vary with respect to the chemical potential of the reference system (determined by the Fermi cut-off of a gold foil).

For better comparison, the spectra have been aligned to the peak positions determined by the spectrum of Pn on Si-H [see Fig. 5.6 (b)]. The splitting of the HOMO can be clearly observed even though it cannot be completely resolved. Referring to the spectrum of Pn on Si-H, the peak positions of the HOMO (H) are $-1.15\,\mathrm{eV}$ and $-1.55\,\mathrm{eV}$ with respect to μ_{exp}. Besides, two further pronounced structures appear in the spectrum at $-2.35\,\mathrm{eV}$ and $-2.9\,\mathrm{eV}$ which are assigned to the HOMO-1 (H-1) and HOMO-2 (H-2), respectively. Additional orbitals can be localized at $-3.4\,\mathrm{eV}$ and $-4.1\,\mathrm{eV}$ which gradually vanish in the secondary electron background.

5.3.3 Core level photoemission

Concluding the section about pristine Pn, the relevant core levels recorded by XPS are addressed. In the case of simple molecules like Pn, this is only a single core level, viz., C $1s$. A respective spectrum of a pristine Pn film in standing mode grown on Si-H, as characterized in Chap. 5.2, is displayed in Fig. 5.7. The peak maximum is located at a binding energy of $E_{\mathrm{bind}} = 284.75\,\mathrm{eV}$, agreeing perfectly with the literature [164, 165]. As one Pn molecule is composed of six inequivalent carbon atoms, indicated by positions $1-6$ in the inset in Fig. 5.7, the C $1s$ core level spectrum contains contributions of six

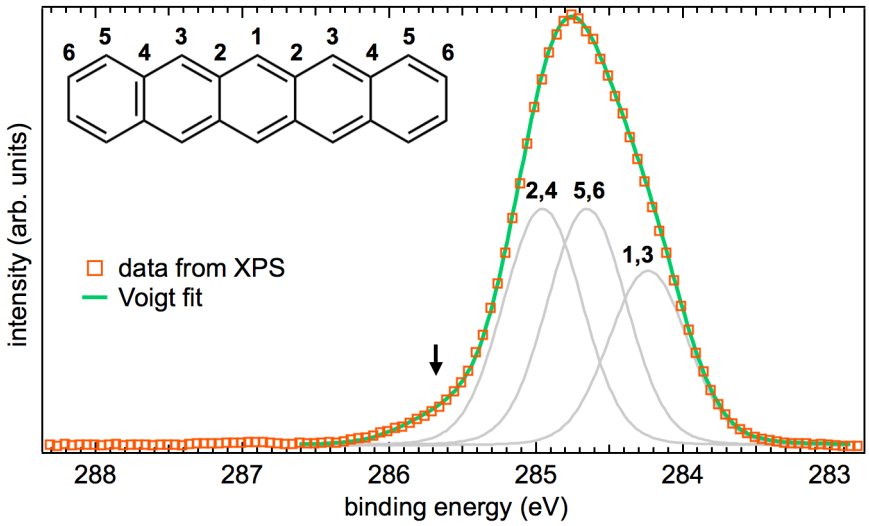

Figure 5.7: *C 1s photoemission core level spectrum of a pristine Pn film on Si-H together with a Voigt fit curve consisting of three single Voigt profiles for different binding energies. The inset sketches a Pn molecule for which the inequivalent atoms are labelled by the numbers* $1-6$.

different electron binding energies. Here, the binding energies of atoms 1 and 3, 2 and 4, as well as 5 and 6 are almost equivalent [164]. In order to fit the spectrum it is sufficient to use a combination of three Voigt profiles accounting for the different binding energies. The three peaks then have to exhibit an intensity ratio of 3:4:4.[1] A corresponding fit profile is illustrated in Fig. 5.7. The peak positions and relative energy differences are in very good agreement with theoretical calculations for gas phase Pn as well as previous experimental observations of gas phase and thin film Pn [164–166].

From the similarity of the film spectrum to a gas phase spectrum – except for a certain broadening due to the embedding of the single molecules in a solid – it can be assumed that the molecules are only affected by the π-orbital overlap of adjacent molecules *within* the layers and the weak van der Waals-interaction *between* the layers. Moreover, this indicates that the molecule-substrate coupling is almost negligible also in the sparsely covered regions between the islands. Molecules which show a certain interaction with the substrate, e.g., Pn lying on a Cu surface, display a significantly different C 1*s* core level peak shape [164]. Both facts point to a growth in standing mode confirming the results from the structural analysis. A small amount of molecules interacting with the substrate is reflected by the shoulder in the C 1*s* spectrum at a binding energy of 285.7 eV denoted by the arrow in Fig. 5.7. Alternatively, the shoulder can be attributed to the contamination of the surface by other carbon compounds like CO_2 [165].

[1] The ratio of 3:4:4 is easily obtained by counting the number of inequivalent atomic positions of carbon atoms in the molecule.

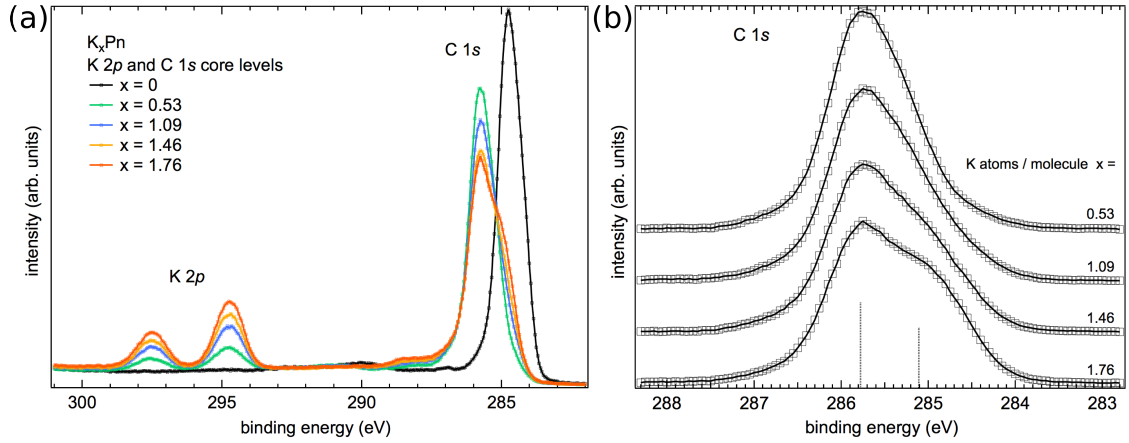

Figure 5.8: *K 2p and C 1s photoemission core level spectra of a K-intercalated Pn film on Si-H for* $0 < x < 1.76$. *(a) Energy range covering both core levels illustrating the increase of K amount. (b) Zoom into the C 1s core level revealing changes in the line shape upon intercalation.*

5.4 K-doping: Inducing a Mott transition?

Pristine Pn is, in principle, well-examined up to now, since it plays a crucial role in the research on organic transistors. The Pn films grown for this thesis are state of the art and offer a good basis for further investigations. Particularly with regard to the observations of Craciun *et al.* in 2009, reporting a Mott metal-to-insulator transition in K-intercalated Pn [15], it is of great interest to learn about the electronic structure of Pn being electron-doped, e.g., by the intercalation with alkali metals. Besides the mentioned study, several other groups report conducting behavior of Pn films doped by alkali metal-intercalation [147, 148, 150]. In the following, the focus is on probing the electronic structure of potassium-intercalated Pn by means of photoelectron spectroscopy and, in particular, having a look at the evolution of the spectral function upon doping.

5.4.1 Core level photoemission: impact of K-doping

First, the relevant core levels shall be addressed. For K_xPn, these are the core levels of carbon and potassium. In the accessible energy range limited by the Al K_α radiation, it is advantageous to consider the K 2p and C 1s core levels. Both are located in an energy window of only 20 eV where the electron IMFP and the analyzer transmission only differ marginally. As for picene, also in the case of Pn these core levels have been used to determine the K concentration x, calibrated as described in A.3. A representation of the above mentioned energy window is given in Fig. 5.8 (a) containing the K 2p and C 1s core levels for several steps of K intercalation ($0 < x < 1.76$) for a Pn film on Si-H. Most obvious from the spectra is that, for the first doping step, the C 1s peak is shifted by ~ 1 eV to a higher binding energy of $E_{\mathrm{bind}} = 285.8$ eV. This is directly related to a shift of the chemical potential caused by the additional electrons inserted into the

system. Furthermore, K intercalation is accompanied by the occurrence of the spin-orbit split K $2p$ core levels at 297.6 eV (K $2p_{1/2}$) and 294.8 eV (K $2p_{3/2}$), respectively. Initially, for low K concentrations the C $1s$ line shape remains largely unmodified. For higher amounts of dopant atoms, reflected by the intensity increase of the K $2p$ core level, a distinct change can be observed. A closer look at the C $1s$ level is taken in Fig. 5.8 (b) for which the change in the line shape is clearly visible. Considering the highest reached K concentration the asymmetry in the C $1s$ line shape is most pronounced, even resembling a two-peak structure with the second peak being located at 285.1 eV. Comparable changes in the line shape of the C $1s$ core levels have been observed in the past for different organic molecular systems upon K intercalation [20, 22].

On the one hand, this can be explained by a spectral redistribution due to screening of the core holes by itinerant electrons now hosted in the former LUMO (fLUMO). For the case of Pn on metal surfaces where screening plays a crucial role, several groups have reported such a behavior [164, 167]. Moreover, one has to consider that the positive charge of K ions in the vicinity of Pn molecules can have a significant influence on the C $1s$ electrons (e.g., change of the Madelung potential) [22]. Owing to the placing of K atoms in the lattice via interlayer insertion the electrons of atoms 5 and 6 (see inset of Fig. 5.7) are strongly affected.

5.4.2 Evolution of the spectral function

While in the previous section the influence of K doping mainly on the C $1s$ core level has been discussed, now the impact of the inserted dopant atoms on the valence band electronic structure in the vicinity of the chemical potential will be examined. The spectral evolution of the valence band upon doping is illustrated in Fig. 5.9 for Pn films grown on Si-H (a) and $SrTiO_3$ (b). In principle, the behavior of Pn films upon K doping does only differ marginally depending on the substrate. Figure 5.9 (a) shows a series of spectra for K concentrations in the range of $0 < x < 1.76$ covering an energy region down to -3.4 eV relative to μ_{exp}. In Fig. 5.9 (b) a larger energy cutout to a maximum binding energy of 5 eV is displayed for a K concentration varying from $0 < x < 1.44$. The topmost curve in each panel represents the spectrum of the pristine Pn film, as described in detail in Chap. 5.3.2. Doping the system with potassium manifests itself in three respects:

(1) For low K concentrations the HOMO peak exhibits a slight shift to higher binding energies.

(2) A new doping-induced feature appears in the former gap, which increases in intensity until saturation sets in at a certain K concentration.

(3) No spectral weight is detectable at μ_{exp} for any doping step, implying insulating behavior for any composition of K_xPn.

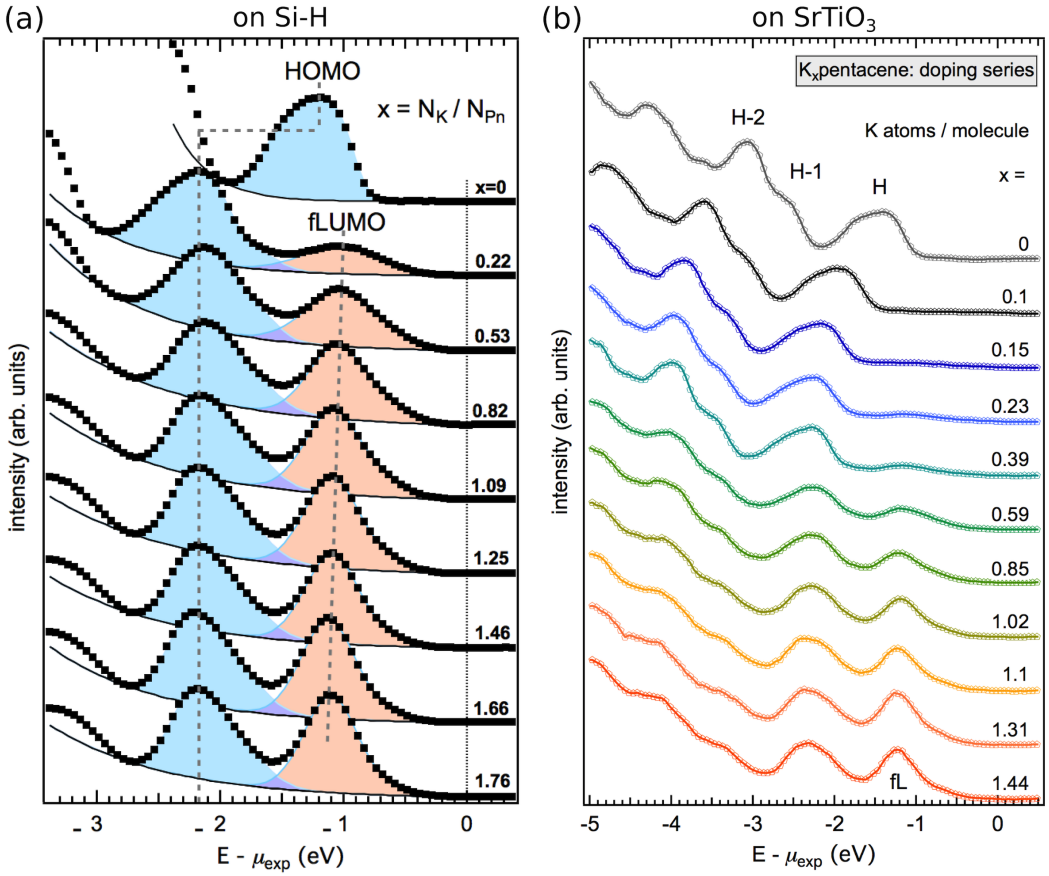

Figure 5.9: *Series of valence band spectra illustrating the influence of K doping on the electronic structure of Pn films. (a) K_xPn on Si-H with $0 < x < 1.76$. (b) K_xPn on $SrTiO_3$ with $0 < x < 1.44$. Details see text.*

Besides these major effects caused by doping, it is noticeable that up to large K concentrations H, H-1, and H-2 still appear fairly pronounced in the spectra. This points to a only weak reorientation of the Pn molecules upon insertion of the K atoms leaving the molecular orbitals largely unaffected. As presented in Chap. 5.1 the well-established structure model of K_xPn assumes interlayer insertion of K atoms and, thus, an unmodified (a, b)-plane [15, 158]. In turn, the measured photoemission spectra are derived by the π-orbital overlap *in* the (a, b)-plane and are not influenced by a c-axis modification. Hence, the obtained results confirm of the mentioned structure model. On that base, the three doping-induced effects will be discussed in the following.

HOMO energy shift

The first effect takes place for low K concentrations between $x = 0$ and 0.2 in terms of an initial shift of the spectra by $0.9 - 1\,\mathrm{eV}$. In the previous section it has been shown that the C $1s$ core level gets shifted by the same amount. While in Pn on Si-H the spectrum instantaneously jumps to the final position [Fig. 5.9 (a)], in Pn on $SrTiO_3$ for very low K concentrations ($0 < x < 0.2$) the spectra progressively shift to the given value where they saturate [see Fig. 5.9 (b)]. However, this is not a contradiction, since the first doping step in Fig. 5.9 (a) corresponds to a K concentration for which the shift already has reached saturation in (b). Moreover, the observed behavior is fully consistent with the report of Bussolotti *et al.* [26].

A comparison of the data obtained within the framework of this thesis and data from the literature is given in Fig. 5.10. It displays the shift of the HOMO peak position plotted against the K concentration x. Additionally, the data points from Ref. 26 have been renormalized according to the applied determination of the K concentration described in A.3 based on experimental photoionization cross-sections, since Bussolotti *et al.* used only the calculated cross-sections from Ref. 59 for the determination of x. The renormalized data points are also included in Fig. 5.10. Except a steeper slope of the data points, the HOMO energy shifts observed for the films under investigation in this thesis exhibit similar behavior as the shifts reported in the literature. Saturation is reached for $x \simeq 0.2$, while the data from Ref. 26 approach the maximum value more slowly and finally reach it for $x \simeq 0.3$ (renormalized value).

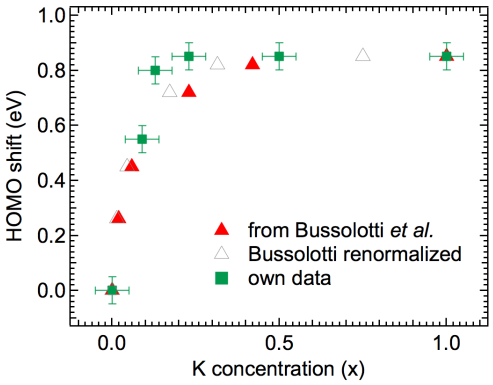

Figure 5.10: *Shifts of the HOMO energy position from photoemission. Shown are the own data points extracted from Fig. 5.9 (a) in comparison with the data from Bussolotti et al. [26]. Furthermore, the data from Ref. 26 have been recalibrated according to the determination of x described in A.3.*

Bussolotti *et al.* propose an interpretation of this behavior based on a gradual up-shift of the chemical potential upon increasing the K concentration [26]. However, it is more likely that a lack of thermodynamical equilibrium and a K concentration gradient are the cause of this behavior, as it is the case for K-doped picene (see Chap. 4.4.1). The effect of a non-homogeneous chemical potential was already observable for the spectra of pristine Pn in Chap. 5.3.2. While in $K_x$picene the non-equilibrium behavior is obvious due to the appearance of spectral weight above the chemical potential, the effect is less pronounced in K_xPn. It only occurs for low K concentrations ($x \lesssim 0.3$). The saturation for already small x is probably due to a better diffusion of the K atoms into the films leading to a faster cancelation of the doping concentration gradient.

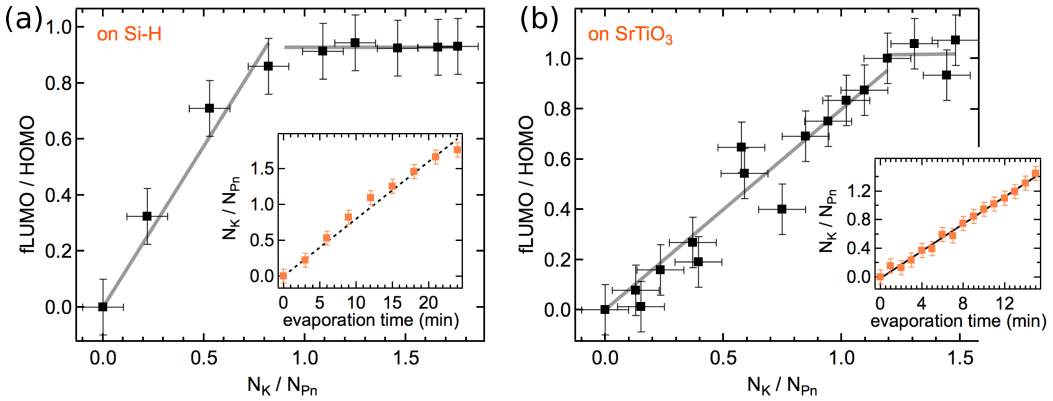

Figure 5.11: *fLUMO-HOMO-ratio deduced from the valence band spectra plotted against the K concentration $x = N_K/N_{Pn}$ for a Pn film on (a) Si-H and one on (b) $SrTiO_3$. The inset in each panel shows the K concentration depending on K evaporation time.*

LUMO filling

After the saturation of the HOMO peak shift, the most prominent impact of K doping becomes obvious by the appearance of a new peak in the former band gap. Depending on the substrate, it appears at -1.0 (-1.1) eV for Pn on Si-H ($SrTiO_3$). Upon further doping ($0.5 < x < 1$) the feature gains intensity and displays a slight shift to an energy of -1.1 (-1.2) eV with respect to μ_{exp}. For an even higher amount of K atoms ($x > 1$) the intensity of the new feature saturates and the spectra show no further changes. The arising new feature is assigned to the photoemission of the fLUMO (fL), getting progressively filled by electrons. In order to get a better idea of its filling, the ratio of the integral intensity of fL to H has been extracted from the valence band spectra.[1] To do so, the spectra have been corrected for He I_β and He I_γ satellites. Additionally, an exponential background has been subtracted to account for the inelastically scattered photoelectrons. Note that not necessarily all corrections have been applied to the data shown in Fig. 5.9. The integrated peak areas used for the determination are illustrated in Fig. 5.9 (a) by the different shading (H: blue, fL: orange). From the thus deduced areas the fLUMO-HOMO-ratio was calculated. In Fig. 5.11 the results are plotted versus the amount of K atoms per Pn molecule, $x = N_K/N_{Pn}$. Note also the linear relationship between evaporation time and potassium concentration, as shown in the insets of both Figs. 5.11 (a) and (b). Regarding the K concentration, in the regime of $0 < x < 1$ the intensity ratio between fL and H increases linearly. For the film on Si-H saturation clearly sets in at $N_K/N_{Pn} = 1$ [see Fig. 5.11 (a)]. Also in Fig. 5.11 (b), a trend towards saturation is identifiable for $x = N_K/N_{Pn}$ close to 1 ($x = 1.2$). Note that the fLUMO-HOMO ratio as well approaches the same value in the saturated regime. However, the value of 1 must not be misinterpreted as a complete filling of the fLUMO, since due to unknown

[1] This corresponds to a normalization of fL to the filled HOMO.

photoionization cross-sections of HOMO and fLUMO this value is no absolute measure for the actual filling. Nonetheless, the value N_K/N_{Pn} can be taken for granted. Assuming the transfer of one electron from each K atom to the neighboring Pn molecule, $x = 1$ corresponds to half filling in K_xPn. The saturation of fLUMO/HOMO thus suggests that Pn can only host one additional electron, agreeing with the literature [15, 168, 169]. On the other hand, this immediately poses the question about what happens with the excess potassium atoms which has to be clarified in the future.

Absence of metallicity

Directly related to the just before described effect is the most striking result of the presented measurements. Despite the gradual filling of the fLUMO, in none of the recorded spectra a finite intensity at μ_{exp} could be observed. This implies that the K-doped Pn films do not reach a metallic state for any doping level. All spectra rather show a true gap of about 300 meV. This unexpected behavior will be unraveled in the next section.

5.4.3 Towards electronic correlations

Remarkably, the occurrence of a new feature in the former HOMO-LUMO gap upon doping, together with the absence of spectral weight at the chemical potential is characteristic for a great variety of alkali metal-doped organic semiconductors investigated by photoelectron spectroscopy [16–26]. In order to illustrate the fact of lacking metallicity more thoroughly, valence band spectra of K_xPn on different substrates are displayed in Fig. 5.12, each for the particular case of $x = 1$. Under the assumption of a transfer of the 4*s*-electron from potassium to the neighboring Pn molecule, in a simple band picture $x = 1$ is equivalent to half filling of the fLUMO band. Thus, in this scenario K_1Pn is expected to be metallic, which is also claimed by basic DFT calculations [15, 158]. From Fig. 5.12, however, unambiguously no metallicity is observable.

Searching for an explanation, one might first think of electron-phonon interaction playing the decisive role in this system. Note that in the case of organic thin films one should more precisely speak of electron-molecular vibration interaction. A metallic DOS at μ_{exp} would be suppressed due to the energy loss of the ejected photoelectrons by the simultaneous excitation of lattice or molecular vibrations. The renormalized spectral function would follow an exponential decay towards the chemical potential, resulting in a pseudo-gap [112, 170]. Such polaronic effects showing pseudo-gap behavior have been observed, e.g., in oxides [111]. However, the recorded spectra do not only lack spectral weight at the chemical potential, i.e., metallic behavior but they exhibit a true gap of at least 300 meV. To underline this, the onset of the fL feature is depicted by the solid black line in each spectrum in Fig. 5.12. A corresponding polaronic scenario thus has to be excluded.

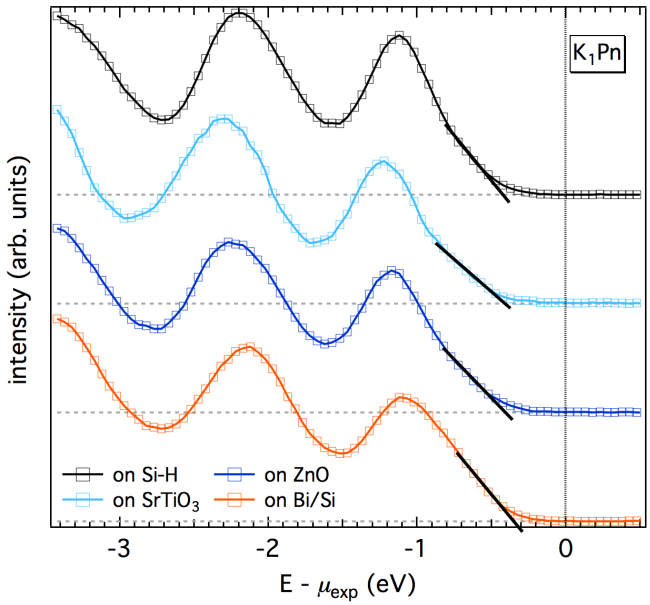

Figure 5.12: *Valence band spectra of K_1Pn on various substrates in the vicinity of μ_{exp}. The onset of each spectrum is depicted by the solid black line. Note that in the case of Bi/Si $x \sim 0.8$.*

Based on both, the ansatz of Craciun *et al.* [15] and the similarity to $K_x$picene, the focus now shall be put on an interpretation in terms of electronic correlations. Since the reported behavior is depending on the doping concentration, the insulating state is expected to be reached by a (band) filling-controlled metal-to-insulator transition (FC-MIT). Here, owing to the interplay of high on-molecule Coulomb repulsion and narrow band width, the insulating state is defined by a Mott insulating state. To understand the underlying physics, first, the evolution of the spectral function expected for the scenario of a (Mott) FC-MIT is sketched. It is displayed on the left-hand side of Fig. 5.13, according to Imada *et al.* [118].

- The spectral function of pristine Pn basically consists of the completely filled HOMO [Fig. 5.13 (a)]. For an ideal semiconductor the chemical potential μ is located in the middle of the HOMO-LUMO gap at T=0.
- Slight doping leads to a partial filling of the former LUMO, the chemical potential shifts and spectral weight emerges at μ induced by the electrons doped into the conduction band [panel (b)]. This is accompanied with a finite conductivity in transport measurements.
- For a doping concentration approaching half filling, electronic correlations come into play and lead to the formation of a correlation induced incoherent band, the lower Hubbard band (LHB), at higher binding energy. Additional to the spectral weight of the LHB, a quasi-particle (QP) peak arises (coherent weight) at μ [panel (c)].

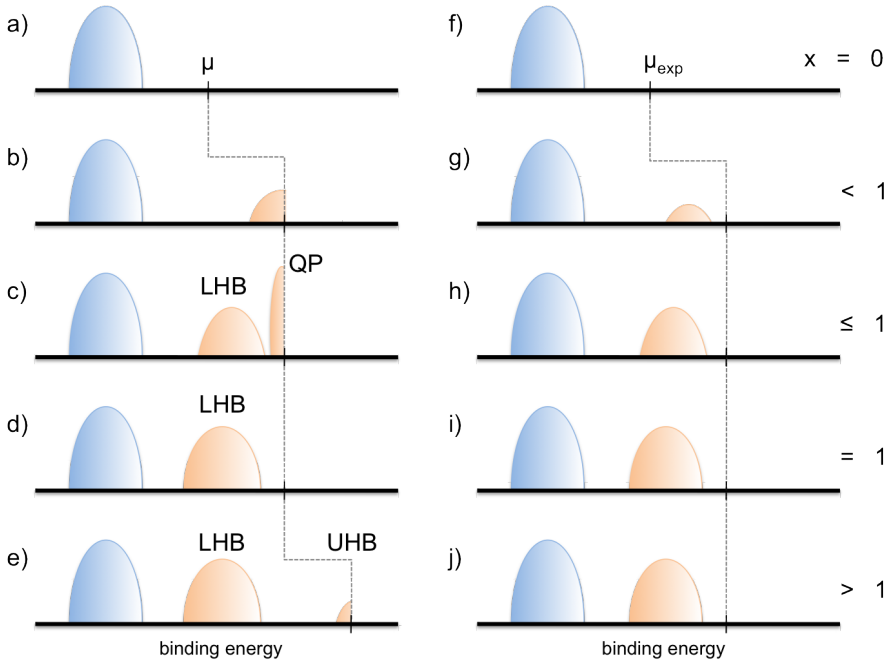

Figure 5.13: *Evolution of the occupied part of the spectral function of K-intercalated Pn in a simple Hubbard approach [panels (a-e)] and for the recorded photoemission data [panels (f-j)]. Details see text.*

- For half filling, which corresponds to one additional electron per Pn molecule, the quasiparticle peak vanishes and the complete spectral weight resides in the LHB [panel (d)].
- Further doping beyond half filling involves the appearance of the upper Hubbard band (UHB) and a further shift of the chemical potential [panel (e)]. Now, additional electrons are donated into the UHB, and again conductivity should be measurable. Note that a QP will also develop for doping concentrations slightly larger than half filling (cf. Chap. 2.2).

On the right-hand side of Fig. 5.13 the evolution of the *measured* spectral function is sketched for comparison.

- The situation for the pristine film is the same [panel (f)] and for slight doping also a shift of μ_{exp} is observable [panel (g)].
- However, no spectral weight occurs at the chemical potential at any doping level. Instead, a new peak develops in the former energy gap [panels (g,h,i)] and increases until a saturation of intensity and energy position is reached for high K concentrations [panel (j)].

Despite the observed discrepancies, the observations reported in this study hint at the great importance of electronic correlations in K-intercalated Pn. For the particular case of $N_K/N_{Pn} = 1$ insulating behavior is observed. Under the assumption of a transfer of one electron per K atom to the molecules, $x = 1$ corresponds to exactly half filling. Thus, K_1Pn can be classified as a Mott insulator displaying a LHB in photoemission. Assuming the chemical potential to lie in the middle of LHB and UHB the energetic position of the new peak yields a Hubbard U of 2.2 eV between the maxima of LHB and UHB. This is in good agreement with the estimated value of $U = 2$ eV from Ref. 26 and the calculated $U = 1.5$ eV from Ref. 15. Apart from Pn, similar behavior has been found in K-doped picene with a U of 1.6 eV (see Chap. 4.4.2) and Alq_3 ($U = 1.5$ eV) [114]. Furthermore, various other alkali metal-doped compounds such as C_{70} [17], C_{84} [16, 18], CuPc [20, 22, 25], and PTCDA [24] show the same characteristics in photoemission. This suggests that the formation of a Mott insulator upon alkali metal-intercalation is an ubiquitous property of many organic semiconductors due to their narrow bandwidths and the sufficiently high on-molecule Coulomb repulsion.

The deviation from the expected trend in case of higher K concentrations ($x > 1$) is easily elucidated. In Fig. 5.11 a saturation of the fLUMO-HOMO intensity ratio at a K concentration of $x = 1$ has been shown. As claimed before by Craciun *et al.* this behavior can be interpreted as the inability of Pn molecules to accept more than one additional electron [168, 169]. Hence, further doping is not possible. However, this immediately poses the question what happens to the excess K atoms. Independent of how the additional K atoms couple, photoemission of the 4 *s*-level is expected to be measurable in the valence band region, but is not observable in the accessible energy range. It is conceivable that the spectral weight of the 4 *s*-level gets lost in the secondary electron background of the valence band.

In the doping regime below the transition to a Mott insulator ($x < 1$), the differences between expectation and measurement can be explained as follows. For non-integer doping concentrations the films separate into coexisting domains of either pristine Pn or K_1Pn. Hence, in photoemission a superposition of the two phases, which are both insulating, is measured. Similar phase separation effects have been observed in K-doped fullerenes [171] and K-doped picene [119]. However, for K-doped Pn no experimental data are available pointing to the occurrence of phase separation. A remaining open point is the question of metallicity in slightly doped Pn for which an increasing conductivity has been found in various transport measurements [15, 147, 150]. As the reported conductivities are small it might result from hopping between impurities, which is not observable in photoemission.

In summary, a model-like filling-controlled metal-to-Mott insulator transition including the occurrence of a quasi-particle peak could not be observed. Nonetheless, the insulating behavior at $x = 1$ most likely originates from electronic correlations, leading to the formation of a lower Hubbard band measurable in photoemission. This assumption is supported by a recent DFT+DMFT study, revealing a Mott insulating state for K_1Pn [121].

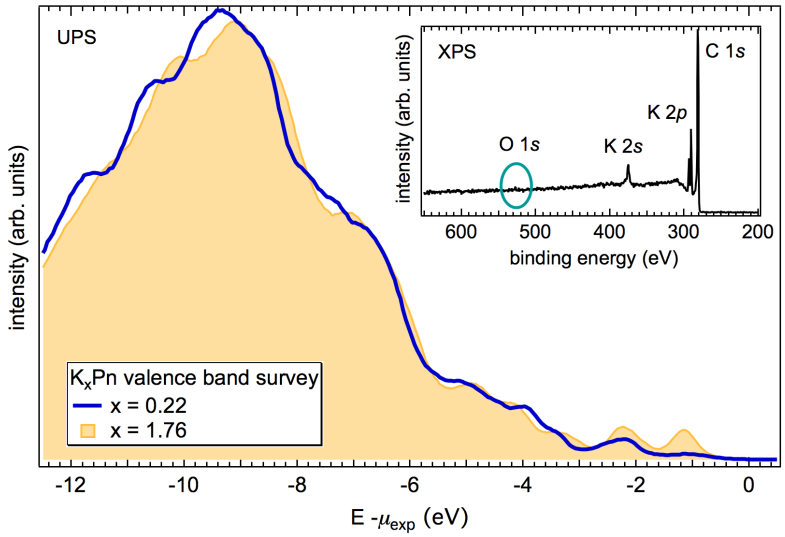

Figure 5.14: *Valence band survey spectrum of K_xPn for $x = 0.22$ and $x = 1.76$, respectively, to illustrate the negligible influence of K oxidation on the electronic structure. The inset shows a survey spectrum from XPS indicating the absence of a O 1s signal.*

5.4.4 Influence of irradiation/oxygen

Recalling the discussions about K-doped picene, two effects had a non-negligible influence on the electronic structure which have been disregarded for Pn so far. These are (1) irradiation damage and (2) the reaction of potassium with oxygen in the residual gas of the UHV system. Remarkably, both effects do not play a role regarding K_xPn.

Concerning the former, neither crucial time effects have been observed during the irradiation of the samples with UV light, nor did any changes in the valence band structure occur after exposure to X-ray irradiation. Both statements are valid for pristine as well as for K-doped Pn. On the other hand, slight changes in the C 1*s* core level spectrum of K_xPn upon X-ray exposure have been detected, which might be assigned to the impact of irradiation. In Fig. 5.8 (a) a small doping – and thus time – dependent 'shoulder' occurs between binding energies of 287 and 289 eV. This might originate from different C 1*s* binding energies due to, e.g., breaking of bonds or cross-linking in Pn caused by the incident X-rays (see also Chap. 6.6.2).

Regarding the influence of oxygen in the residual gas on K-doped Pn, its insignificance is presented in Fig. 5.14. Valence band survey spectra ($-12 < E < \mu_{exp}$) are displayed for K concentrations $x = 0.22$ and $x = 1.76$, respectively. Characteristic photoemission features of K oxide should be detectable at about $E \simeq$-2 eV and -5.8 eV. Though, at these energy positions no distinct changes between a slightly K doped and a massively K doped Pn film are observable in the line shape. Note, however, that in contrast to picene, Pn has a smaller band gap. Owing to this smaller gap, K oxide peak A (see A.4) is located approximately at the same position as the HOMO and thus would be superimposed by

the stronger emission of H. However, also no indication for the occurrence of K oxide feature B can be found in the spectra. Furthermore, no signal from any oxygen species is detectable in XPS, as illustrated in the inset of Fig. 5.14. Hence, it can be assumed that oxygen from the residual gas does not show a significant influence on the samples under investigation in the case of K-doped Pn.

5.5 Short summary

Concluding the chapter on pentacene and the impact of K-doping on its electronic structure, the most intriguing results will be summarized. In the framework of this thesis, pentacene films of high structural quality have been grown on a variety of substrates. Concerning the electronic structure of pristine pentacene films, the recorded core level and valence band photoemission spectra are well reproducible and coincide with or even outperform corresponding spectra from the literature. K-doping influences the electronic structure of pentacene in three respects. For low K concentrations a shift of the entire spectrum to higher binding energies is observable. Moreover, upon doping a new photoemission feature appears in the former HOMO-LUMO gap. However, the feature does not have metallic character, thus, K_xPn remains insulating for any K concentration. Most likely, the shift can be explained by a lack of thermodynamic equilibrium in combination with a K concentration gradient in the films which both gradually decrease. Origin of the feature in the former gap is the filling of the LUMO with electrons. The concomitant absence of metallicity is ascribed to the crucial role of electronic correlations in K_xPn coming along with the formation of a lower Hubbard band.

A further remarkable aspect is that in pristine and K-doped pentacene neither the incident UV and X-ray radiation nor the oxygen in the residual gas of the UHV system have a significant impact on the electronic structure in photoemission. This is in sharp contrast to, e.g., picene and coronene, as discussed in this thesis.

6 A further alleged aromatic superconductor: $K_x$coronene

In the context of the new 'family' of aromatic superconductors, one more polycyclic aromatic hydrocarbon (PAH) attracted considerable attention in the nearest past, namely, coronene. Next to the other PAHs picene, phenanthrene, and dibenzopentacene [7, 8, 11] it is reported to exhibit a pronounced Meissner-Ochsenfeld effect below $T_c = 7\,K$ when intercalated with potassium for $2.5 < x < 3.5$ (x = K concentration) [10]. Strikingly, here again *three* K atoms lay the foundation of reaching the superconducting state. Considering the electron-intramolecular-phonon coupling, already in 2002 the occurrence of superconductivity in negatively charged coronene has been proposed [172]. Furthermore, more recent DFT calculations reveal the formation of metallic bands for K-doped coronene [173], which could host the superconductivity at sufficiently low temperatures. In contrast, in photoemission K-doped coronene appears to be an insulator [85], which is actually not surprising with regard to the photoemission properties of picene and pentacene reported in this thesis. Nevertheless, it is of great interest to extensively explore the electronic structure of coronene in the pristine state as well as upon doping. Especially the differing molecular structure makes it interesting to see which differences from and commonalities to picene or pentacene can be identified.

The electronic structure of pristine coronene and of coronene doped with various amounts of potassium has been investigated by means of PES in this thesis. To this end, valence band and core level analyses have been conducted using UPS and XPS, respectively. In order to structurally characterize the fabricated films also AFM and XRD results will be presented.

6.1 From the parent compound to $K_x$coronene

Depending on the point of view, the molecule coronene ($C_{24}H_{12}$, abbreviated Cor in the following) can be considered as either a ring built up of six benzene rings or a disk made of seven benzene rings. Both representations appear in the literature [85, 173]. A single Cor molecule is sketched in Fig. 6.1 (a). Since it is a planar, π-conjugated molecule, it is often also classified as one of the *nano-graphenes*. Cor crystallizes in a monoclinic structure (space group $P2_1/a$) with the lattice parameters $a = 16.095\,Å$, $b = 4.690\,Å$, $c = 10.050\,Å$, and $\beta = 110.79°$ [174]. Similar to the previously presented materials picene and pentacene and to most of the aromatics [88], the Cor molecules arrange

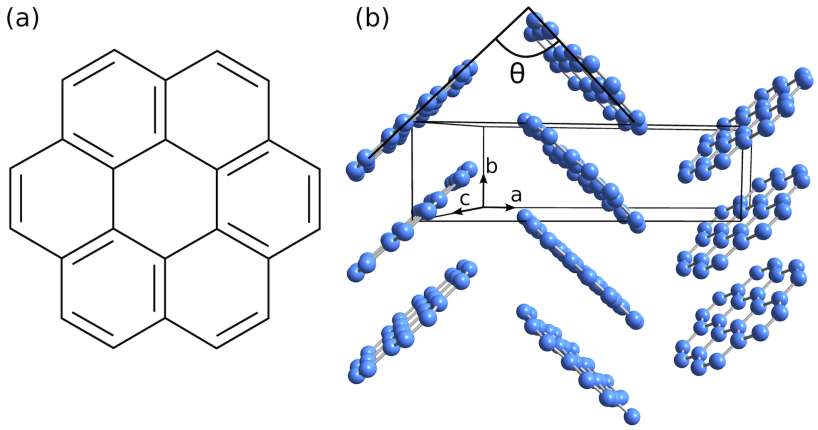

Figure 6.1: *(a) Structural formula of a single coronene ($C_{22}H_{14}$) molecule. (b) Unit cell structure of pristine coronene crystals or thin films. The molecules are arranged in a herringbone manner and the unit cell contains two inequivalent Cor molecules. Note that the H-atoms are not included.*

in a herringbone manner, ending up with two inequivalent molecules in the unit cell. Figure 6.1 (b) displays a view onto the (a, b)-plane of the Cor crystal structure. Calculations of the structure within density functional theory (DFT) are able to reproduce the given experimental lattice parameters [10, 173]. Furthermore, the herringbone angle θ (angle between the molecular planes of the inequivalent molecules) has been determined from DFT to be 95° [173]. Crystallized in the way described above, Cor forms an organic semiconductor with a transport gap of $E_{\text{gap}} = 3.3 - 3.6\,\text{eV}$ [175–177]. The corresponding optical gap has been determined as $E_{\text{opt}} \simeq 2.8\,\text{eV}$ [176, 177].

Concerning K-doped coronene (K_xCor), no structural data neither from experiment nor from theory are available up to now. DFT calculations of the superconducting phase K_3Cor only propose a candidate structure for which K atoms are inserted into the layers as well as between. Consequently, one cannot clearly separate between intra- and interlayer insertion in the case of K_xCor.

6.2 Fabrication of pristine coronene films

As is the case for picene and pentacene, *in vacuo* grown thin films have been the first choice for the present study on coronene. Especially concerning K-doped Cor, the advantages of thin films opposite to single crystals are the same as for picene and pentacene (see Chap. 4.2 or 5.2). However, very little is known about the growth and the structure of Cor thin films exceeding the deposition of single molecules or monolayers, which in general leads to molecules lying flat on the substrate surface [178–180]. Regarding the growth of Cor films on NaCl(001) substrates, the formation of very small crystallites ($< 1\mu$m) with no preferred orientation has been observed [181]. In the framework of this thesis, natively oxidized silicon (denoted **SiO$_2$**) and the 7×7-reconstructed (111)-surface

of silicon (**Si-7×7**) have been used as substrates for the fabrication of Cor films (see A.1 for details of substrate preparation). Deposition of Cor molecules was achieved at room temperature by evaporation of purified Cor powder from a commercial effusion cell (organic molecular effusion cell, OME, by MBE Komponenten GmbH). All films were grown in a UHV environment at a pressure of $5 \cdot 10^{-9}$, not exceeding $1 \cdot 10^{-8}$ mbar during growth. The formation of K_xCor was realized by subsequent evaporation of K from a commercial SAES getter source onto the films in the analysis chamber (pressure $< 5 \cdot 10^{-10}$ mbar). For structural film characterization an AFM operated in tapping mode (Veeco) and XRD using Cu K_α radiation ($\lambda = 1.5418$ Å) were employed.

Since the film growth of Cor is not well-established up to now, the films presented here have to be considered as first attempts towards Cor thin film growth. This is manifested in the largely undefined structure. For illustration, Fig. 6.2 (a) shows a $700 \times 700\,\mathrm{nm}^2$ AFM image of the surface morphology of a Cor film on Si-7×7 with a nominal thickness of 15 nm as obtained by QCM monitoring. In this cutout, it can be clearly seen that Cor forms small crystallites with a size of a few hundred nm. The formation of flat islands or the coalescence of the islands could not be observed. Instead, the islands show the trend to grow along the substrate surface normal, leading to the creation of elevated structures. Larger survey images could not be recorded by AFM, since even higher crystallites on the surface hindered a meaningful measurement. As the molecules preferably arrange out-of-plane, large areas on the substrate surface between the crystallites remain uncovered. This is pointed out in Fig. 6.2 (b) showing a $350 \times 350\,\mathrm{nm}^2$ zoom into the surface morphology image from (a), indicated by the dashed square. One can discern a terraced shape with a step height of ~ 3 Å. The step height has been deduced from the line profile plotted in Fig. 6.2 (d), which has been recorded along the light solid line in the AFM image in (b). This step height of 3 Å perfectly coincides with the step height of the 7×7-reconstructed Si(111) surface [182], thus, implying the observation of the bare substrate surface. A further hint to the formation of large (out-of-plane) structures can be gathered from Fig. 6.2 (e). It shows a $1.00 \times 0.75\,\mu\mathrm{m}^2$ image recorded with an optical microscope. The coarse graining of the deposited film is clearly observable. For comparison, a $1.00 \times 0.75\,\mu\mathrm{m}^2$ image of a picene film on silicon is displayed in Fig. 6.2 (f). Here, the surface morphology exhibits visibly less coarse graining ascribed to the significantly flatter islands, which coalesce upon further film growth.

However, the Cor films are not completely disordered but show at least a certain ordering as can be deduced from the X-ray diffractogram in Fig. 6.2 (c). A weak Bragg peak can be identified at a momentum transfer of $q_z = 0.665\,\mathrm{Å}^{-1}$ corresponding to a lattice spacing of 9.44 Å. Most likely, this represents the Bragg reflection of the Cor crystal's c-axis ($c = 10.05$ Å) with a slightly higher tilting angle compared to the single crystal. This implies a growth in standing mode also in the case of Cor (cf. growth mode of picene, pentacene).

Concerning the film thickness, in the case of Cor no statement is possible, since the effective film thicknesses could not be scrutinized by AFM. Moreover, due to the insufficient data situation no reliable information could be gained about the coverage.

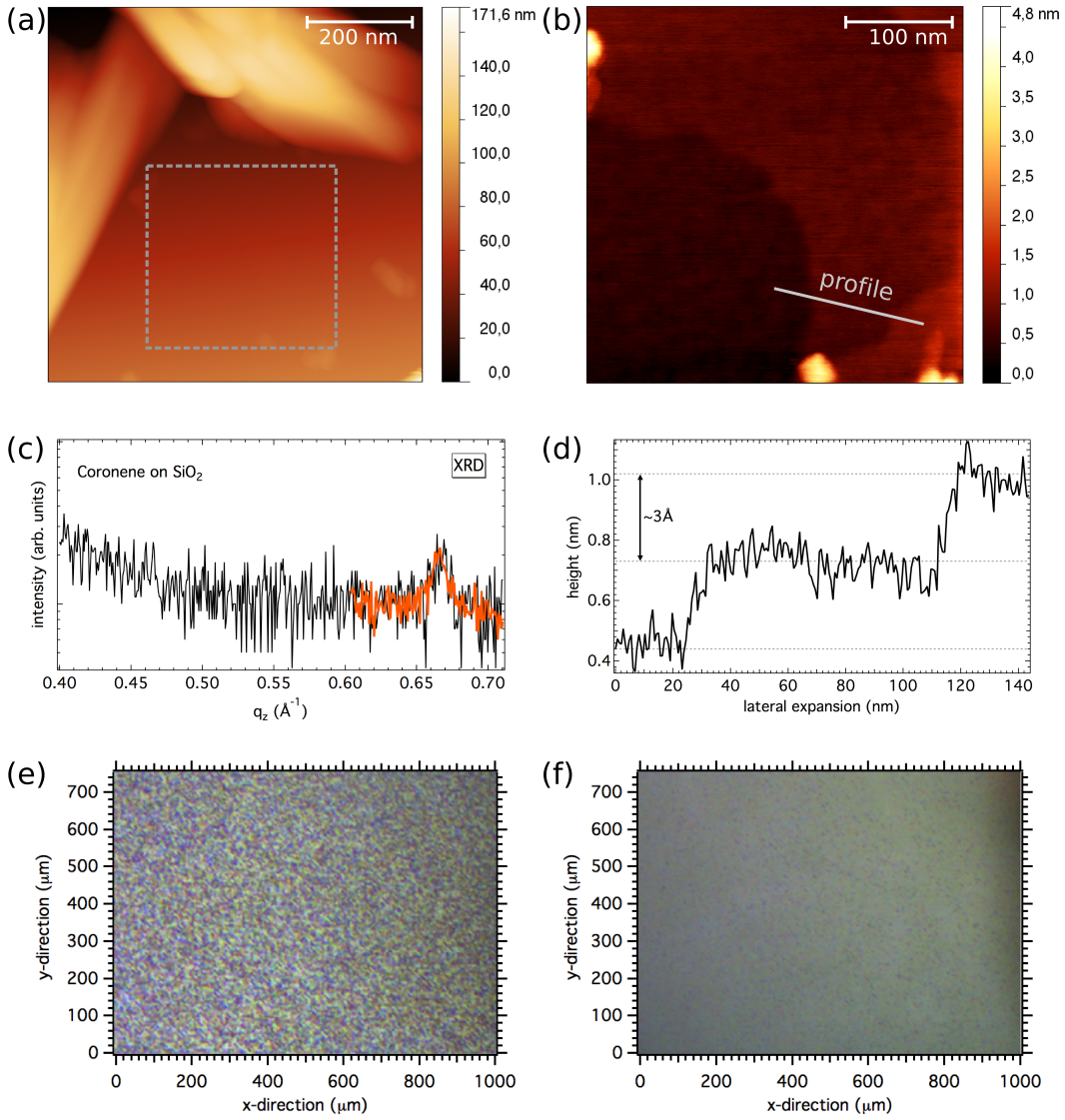

Figure 6.2: *Structural characterization of Cor films. (a) 700×700 nm² AFM image of a Cor film on Si-7×7. (b) 350 × 350 nm² zoom into (a), indicated by the dashed square. (c) X-ray diffractogram of a Cor film on SiO_2. (d) Height profile along the light solid line in (b). (e) 1.00 × 0.75 µm² optical microscope image of the surface of a Cor film. (f) Corresponding 1.00 × 0.75 µm² image of the surface of a picene film for comparison. Details see text.*

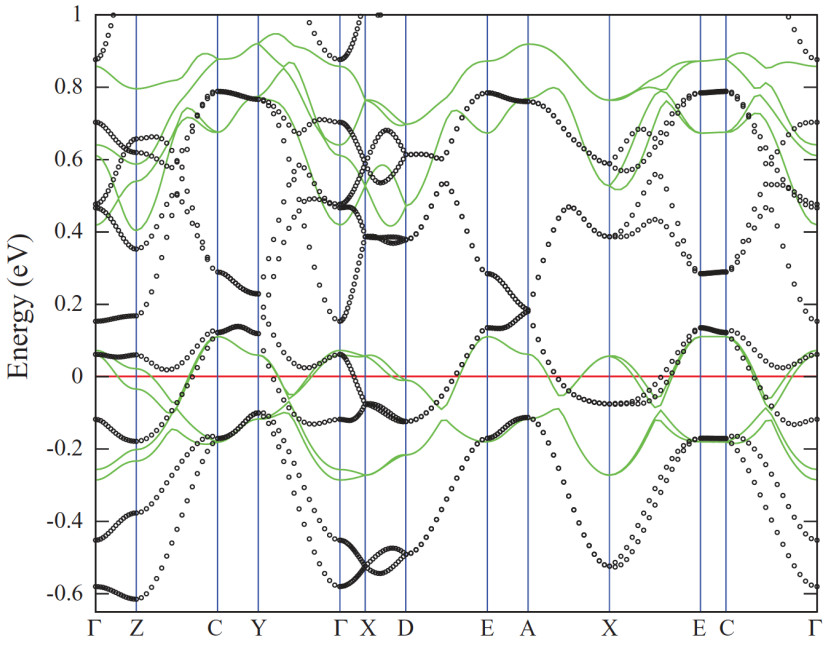

Figure 6.3: *DFT band structure of pristine Cor (solid green curves) and K_3Cor (black circles). Zero energy for K_3Cor is set to its Fermi level. For better comparison, the origin of energy for pristine Cor is set for an assumed filling with three additional electrons in a rigid-band shift. For the definition of the high symmetry points of the monoclinic lattice see Fig. 4.3 (d). Figure reprinted from Ref. 173 with permission from R. Arita. Copyright (2013) by The American Physical Society.*

In summary, the results of the structural characterization presented in this chapter call for further improvement of the growth conditions to reach a controlled and ordered growth of Cor films. The films under investigation basically consist of small crystallites growing largely perpendicular to the substrate surface. Thereby, elevated structures with abrupt height differences are formed, which make the investigations by means of AFM highly sophisticated. Nonetheless, some ordering in *c*-direction as deduced from XRD is present. Hence, despite some structural deficiencies, the films are assumed to be adequate for a photoemission study.

6.3 General aspects of the electronic structure of $K_x$coronene

Apart from the largely unexplored *real space* structure of Cor films, also the research on the *electronic* structure of these films is still in its infancy. Up to now, only a single study is available, addressing the prediction of the electronic structure of pristine and K-doped Cor by DFT calculations [173]. The reported band structures are plotted in Fig. 6.3 in which pristine and K-doped Cor are represented by the solid green curves and the black

circles, respectively. For pristine Cor, the conduction band (located between -0.3 and 0.1 eV) consists of four single bands originating from the doubly degenerate LUMOs of the two inequivalent Cor molecules in the unit cell. Note that in picene, for comparison, the conduction band only contains two bands. Zero energy has been set to a filling of the LUMO band with three additional electrons to allow for a better comparison with the K_3Cor band structure for which $E = 0$ has been set to the position of the Fermi level. The x-axis is labelled with the high symmetry points of the monoclinic Brillouin zone [see Fig. 4.3 (d)]. Two major aspects can be deduced from the calculations: (1) Upon doping by alkali metal intercalation a non-rigid band behavior is observed. Thus, Cor behaves very similar to picene. (2) For the particular case of K_3Cor, which is reported to be superconducting at low temperatures, the DFT calculations reveal a metallic state. This is similar to picene as well. However, regarding picene, it turned out that the DFT calculations were not able to describe the doped compound properly. A more detailed look at the electronic structure of Cor will thus be given in the following.

First experiments on Cor thin films have been conducted by Roth *et al.* who probed the electronic structure by means of EELS [177]. The analyzed K-doped Cor films with a stoichiometry close to K_3Cor (determined by core level excitation data) reveal a reduction in intensity of the lowest-lying C 1s excitation features indicating that potassium addition leads to a filling of the Cor conduction bands. Furthermore, they observe changes in the electron energy loss spectrum upon doping where a new low-energy feature is assigned to a charge carrier plasmon [177]. Thus, metallicity of K_3Cor is concluded. In contrast, Mahns *et al.* provide first photoemission results of K_xCor with $0 < x < 4.74$, yielding insulating behavior independent of the K concentration [85]. Based on these preliminary results, a detailed study of the electronic structure of pristine and K-doped Cor films from photoemission will be presented in the following sections.

6.4 Electronic structure of pristine coronene

In order to have a closer look at the electronic structure of K_xCor, suitable films have been investigated by means of photoelectron spectroscopy within the framework of this thesis. Core level and valence band analyses have been carried out using monochromatized Al K_α (1486.6 eV) as well as He I (21.2 eV) radiation. All measurements have been performed at room temperature with a total energy resolution of 0.7 eV and 0.1 eV for XPS and UPS, respectively. The spectra are generally plotted with respect to the experimental chemical potential, μ_{exp}, of the spectrometer, determined by measuring the Fermi cut-off of a sputtered gold foil.

6.4.1 The valence band region

Valence band spectra of different Cor films grown on SiO_2 and Si-7×7 are displayed in Fig. 6.4 (a). The general spectral shape is similar for all films containing two pronounced

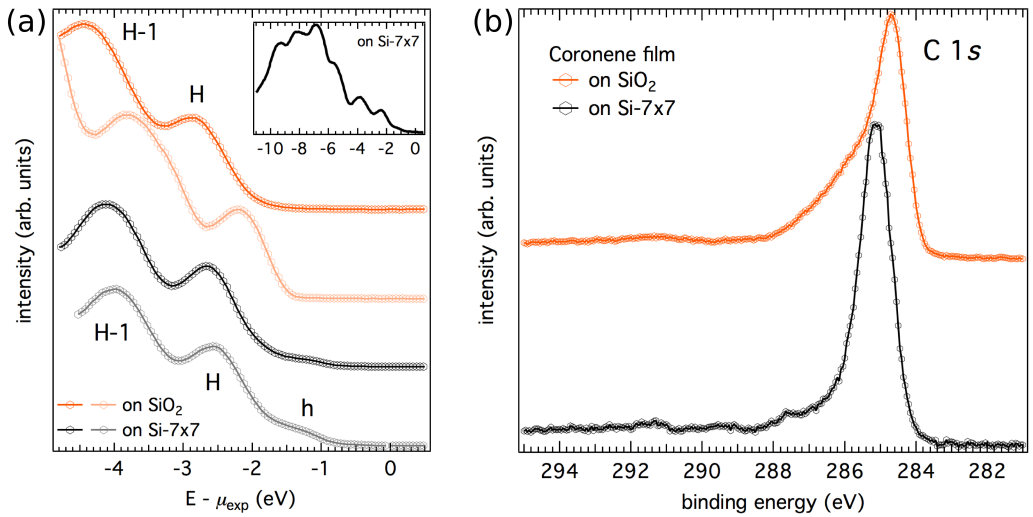

Figure 6.4: *Photoemission spectra of Cor films on SiO_2 and Si-7×7. (a) Valence band spectra of different films, each containing the HOMO (H) and HOMO-1 (H-1). For spectra of Cor on Si-7×7, a further HOMO feature is indicated by 'h'. The inset shows a valence band survey spectrum of Cor on Si-7×7. (b) Corresponding C 1s core level spectra of Cor on SiO_2 and Si-7×7.*

peaks which are assigned to the photoemission of the HOMO (H) and the HOMO-1 (H-1). In the inset of Fig. 6.4, showing a valence band survey spectrum, further molecular orbitals can be identified. All spectra of pristine Cor films agree well with data from the literature [85, 175]. Since the different spectra all exhibit a certain shift with respect to the others, no exact energy positions of the molecular orbitals can be specified. Nonetheless, the approximate position of H is located between -2.2 and -2.9 eV, and the energy of H-1 varies from -3.8 to -4.5 eV relative to μ_{exp}. Beside H and H-1, a small additional peak is observable in the spectra of Cor on Si-7×7 at approximately -1.3 eV. This structure is assumed to be also ascribed to the HOMO, partially renormalized in energy. This might be due to slightly differing structural details of films on Si-7×7 compared to Cor on SiO_2. Therefore, it is labelled 'h' in Fig. 6.4 (a).

Different energy positions of the measured peaks relative to μ_{exp} can again be attributed to the absence of an electronic equilibrium between substrate and Cor film, since also in Cor the stacked molecular layers are only weakly van der Waals-coupled. However, the noticeable difference between spectra of similar films on identical substrates hints to a strong influence of the incident radiation on the samples during the measurement. This will be addressed in detail in Chap. 6.6.2.

6.4.2 The carbon core level

Since coronene (like picene and pentacene) only consists of carbon and hydrogen atoms, here too, the only relevant core level which is accessible by the utilized excitation energy

of 1486.6 eV, is the carbon 1*s* (C 1*s*) core level. Two C 1*s* spectra of Cor grown on Si-7×7 and SiO_2, respectively, are plotted in Fig. 6.4 (b). In the upper spectrum (Cor on Si-7×7) the peak is located at a binding energy of $E_{\mathrm{bind}} = 285.1$ eV, exhibiting a FWHM of 1.1 eV. It thus agrees well with corresponding core level spectra from the literature [85, 175, 183]. On the contrary, the lower spectrum (Cor on SiO_2) with C 1*s* located at $E_{\mathrm{bind}} = 284.7$ eV displays a pronounced shoulder between 285.5 and 287 eV. Such unusual behavior points again to a strong impact of the X-ray radiation used for the photoemission experiments on the samples under investigation. A more comprehensive analysis will be presented in Chap. 6.6.2.

6.5 K-doping and its impact on the electronic structure of coronene

Experimentally, the picture of the electronic structure of K-doped Cor is still controversial. On the one hand, polycrystalline powder samples of K_xCor with $2.5 < x < 3.5$ are reported to become superconducting below $T_c = 7$ K [10]. Furthermore, DFT calculations reveal a metallic band structure which can serve as the basis for the transition to a superconducting state at low temperatures [173]. On the other hand, thin films of K_xCor display insulating behavior for all probed K concentrations [85]. The latter is supported by the results gained within the framework of this thesis, as will be presented in the following. Again, K concentrations have been determined by the aid of the potassium and carbon core levels using the procedure described in A.3.

6.5.1 The valence band region

Regarding the valence band in an energy range of a few eV relative to μ_{exp}, the evolution of the spectral function of Cor films upon K doping is illustrated in Fig. 6.5. The topmost curve represents the spectrum of a pristine Cor film, as already discussed in Chap. 6.4.1. Here again, the HOMO and HOMO-1 are labelled H and H-1, respectively. Upon doping the entire spectrum is shifted by approximately 1.2 eV, taking H-1 as a reference. This shift can be attributed to a change of the chemical potential due to the insertion of additional electrons into the system. Furthermore, the impact of K doping manifests itself in the spectra in three respects:

(1) The appearance of an additional spectral feature at -0.9 eV, gaining in intensity with increasing K concentration.

(2) A further, slightly visible, spectral feature at -2.1 eV, independent of x.

(3) A change of the HOMO energy position with respect to H-1.

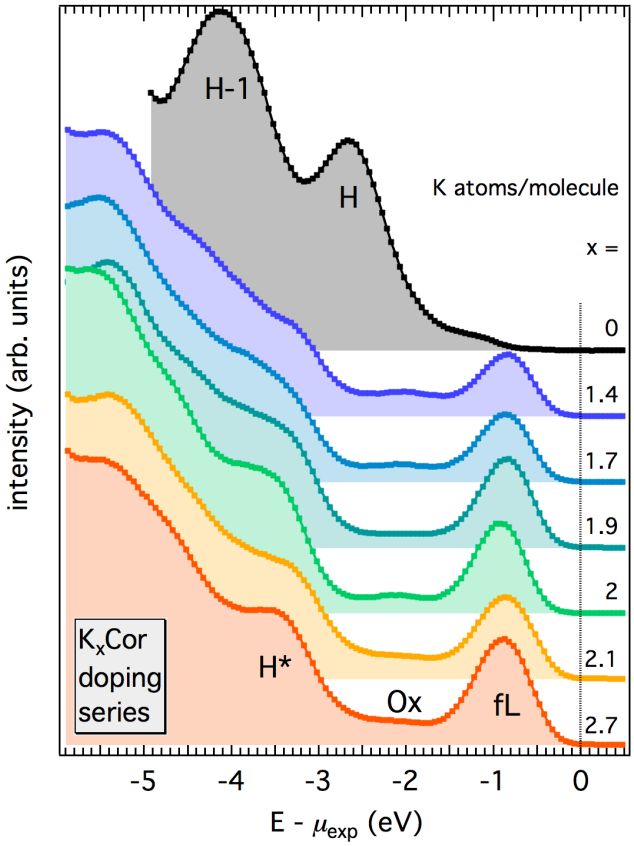

Figure 6.5: *Valence band photoemission spectra of a K_xCor doping series with $0 < x < 2.7$. In the spectrum of pristine Cor the HOMO and HOMO-1 are labelled H and H-1, respectively. For doped Cor, three main peaks are observable: the relaxed HOMO (H*), an oxygen induced feature (Ox), and the filled former LUMO (fL). The spectra are gapped for all probed K concentrations.*

Beginning with (3), the initial two-peak structure of H and H-1 firstly develops to a three-peak structure observable in the spectrum of $K_{1.4}$Cor. The corresponding peaks are positioned at -3.3 eV, -4.4 eV, and -5.4 eV, respectively. For higher K concentrations the separate peaks at -4.4 and -5.4 eV largely merge, whereas the peak at -3.3 eV remains unaffected and gets more pronounced in the spectra of films with larger K amount. This peak is assigned to the energy renormalized HOMO and thus denoted H* in Fig. 6.5. The energy renormalization is owing to the reorientation of the molecules in the lattice upon insertion of foreign atoms [101, 125]. (2) The second new feature appearing at -2.1 eV (labelled Ox) is ascribed to the formation of potassium oxide during the measurements and will be addressed in detail in Chap. 6.6.1. (1) Similar to picene, the most prominent doping-induced feature in Cor is the novel peak emerging at -0.9 eV, which increases in intensity depending on the K concentration. Due to the given x-dependence, the feature can be assigned to the photoemission of the former LUMO (denoted fL) getting

progressively filled with electrons. Contrary to the predictions from theory, for none of the analyzed compositions of K_xCor, spectral weight at μ_{exp} has been detected. This unambiguous absence of metallicity will be discussed in the next section.

6.5.2 Importance of electronic correlations

Due to the striking similarity of the photoemission results obtained for K_xCor to the results for $K_x$picene and K_xPn (see Chaps. 4.4.2 and 5.4.2), it seems reasonable to explain the origin of the observed insulating behavior here as well in terms of electronic correlations. Polaronic effects are again unlikely, since the spectra exhibit a gap of at least 200 meV instead of showing an exponential decay of the spectral weight towards the Fermi level.

On the other hand, the necessary prerequisites for the emergence of electronic correlations are fulfilled in Cor. A narrow band width of $\sim$ 0.4 eV (LUMO band [173]) together with an on-site effective Coulomb repulsion of 1.3 eV [74] leads to a correlation strength of $U/W = 3.25$, strongly hinting to the importance of electronic correlations in K_xCor. In analogy to the photoemission and DFT+DMFT results for $K_x$picene (see Chap. 4.4.2), Cor, too, is assumed to be a Mott insulator upon K-doping for integer x. In this scenario, the spectral feature at -0.9 eV in the photoemission spectra which was ascribed to the gradually filled LUMO, represents the lower Hubbard band. Under the assumption of the Fermi level lying in the middle of the Mott-Hubbard gap, one can get an estimate of U in K_xCor. Independent of x, the maximum of the LHB is located at -0.9 eV. Thus, the Hubbard U can be estimated to be 1.8 eV, agreeing well with the prediction of 1.3 eV from theory [74].

Concerning compositions of K_xCor with non-integer K concentrations, the uniform appearance of the photoemission spectra independent of x might be elucidated as follows. The determined doping concentration is a macroscopic quantity, averaged over the extension of the photon spot ($\sim$ 1 mm) defined by the UV source. The thus probed area may be composed of phase-separated domains with integer doping concentrations. Similar phase separation behavior has been observed in, e.g., potassium doped fullerenes or picene [119, 171]. In this manner the photoemission spectra can be understood as a superposition of different phases with integer x (cf. also Chap. 4.4.2).

6.5.3 Core level photoemission

Topping off the section about the impact of K doping on the electronic structure of Cor films, the associated relevant core levels will be considered. Due to the composition of the K_xCor films of solely carbon and potassium, the important core levels in the accessible energy range are K $2p$ and C $1s$. In Fig. 6.6 the corresponding photoemission spectra (as measured) are plotted for $0 < x < 2.7$. A spectrum of pristine Cor, as described above, is included. Doping manifests itself in a shift of the C $1s$ core level by 0.9-1.2 eV, which is close to the value observed for the shift in the valence band. The position of C $1s$ varies

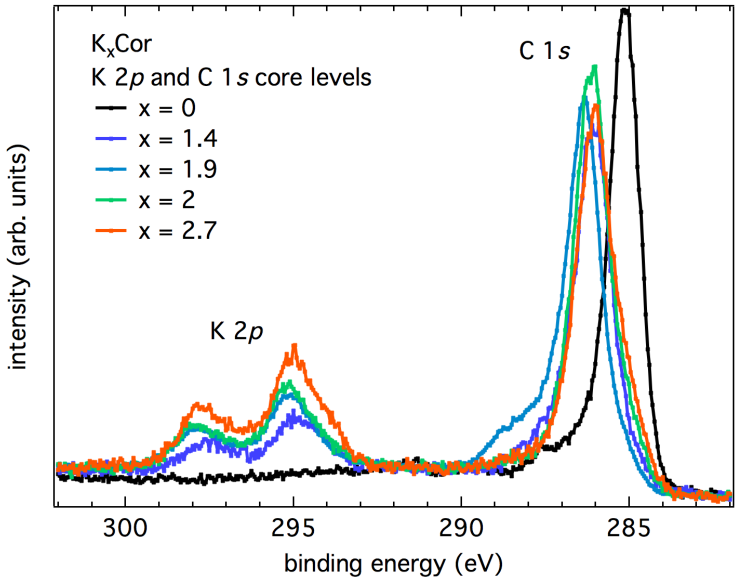

Figure 6.6: *C 1s and K 2p core level photoemission spectra of a K_xCor doping series with $0 < x < 2.7$. The increasing K amount is reflected by the intensity gain of the K 2p core level, whereas the C 1s intensity remains largely unaffected.*

between $E_{\mathrm{bind}} = 286$ and 286.4 eV depending on the K concentration. Furthermore, the increasing amount of K is reflected in the intensity gain of the K 2p core level of which the spin-orbit levels are located at $E_{\mathrm{bind},3/2} = 295$ eV and $E_{\mathrm{bind},1/2} = 297.7$ eV, respectively. Besides the varying energy position of C 1s, two distinctive features can be discerned from Fig. 6.6: (i) For higher K concentrations the K 2p core level displays a small shoulder at the lower binding energy side. This shoulder may be assigned to the formation of K oxide resulting from the reaction of the dopant material with molecular oxygen in the residual gas of the UHV system. A detailed analysis of this effect will be given in Chap. 6.6.1. (ii) In the spectrum of $K_{1.9}Cor$ a shoulder is observable at the higher binding energy side of the C 1s core level. Compared to the spectra of pristine Cor, this may hint to radiation damage caused by the incident X-rays. The influence of irradiation on the electronic structure of K_xCor will be discussed in Chap. 6.6.2.

6.6 Extrinsic influences

As already observed in the previous sections, Cor is subject to extrinsic influences on the electronic structure coming along with the measurement conditions. More precisely, samples stored in UHV for a longer period show a certain reaction of the K atoms with molecular oxygen present in the residual gas of the UHV system. Furthermore, a considerable impact of the incident X-ray radiation on the electronic structure is observable.

6.6.1 Oxidation of potassium

From Fig. 6.5, a small additional spectral feature between H* and fL can be identified at an energy of -2.1 eV relative to μ_{exp}. It is assigned to the oxidation of potassium and thus denoted 'Ox'. This assumption will be substantiated in the following. Figure 6.7 (a) shows valence band photoemission spectra of two K_xCor films ($x = 1.4$ and 2) on Si-7×7. For each film two spectra are plotted, the one recorded immediately after K deposition and the other after a 12 h storage in the UHV system. The storage in UHV results in an intensity increase of the feature Ox accompanied by an intensity increase of a second feature, separated from Ox by 3.7 eV (both highlighted by the gray shading). As described in detail in A.4, both features are directly related to the photoemission of K oxide [122]. Note that the second oxide induced peak (B in Fig. A.5) overlaps with H-1 which hampers a clear discrimination between the two contributions. However, the considerable intensity increase cannot be caused by H-1 and can thus safely be ascribed to the presence of K oxide. The statement is consolidated by core level analysis regarding the O 1s and K 2p core levels displayed in Fig. 6.7 (b) and (c). As is obvious from Fig. 6.7 (c), the storage in UHV manifests itself in the K 2p core level by a redistribution of spectral weight towards lower binding energies. Compared to pure potassium, the occurrence of spectral weight at slightly lower binding energies clearly indicates the formation of K oxide [123]. Furthermore, the presence of oxygen can be directly deduced from the O 1s spectrum. While for the spectrum recorded immediately after K deposition only background signal is measurable in the energy range of 536eV $< E_{\text{bind}} <$ 529 eV, a distinct O 1s peak appears for the 12 h stored samples see Fig. 6.7 (b).

The described effect of the reaction of K with molecular oxygen in the residual gas on the electronic structure is even more pronounced in Cor films on SiO_2. A corresponding valence band spectrum is represented by the lowest curve in Fig. 6.7 (a). Compared to $K_{1.4}$Cor on Si-7×7 (dark blue curve), in the spectrum of $K_{1.5}$Cor on SiO_2 a stronger contribution of Ox is clearly visible, while simultaneously fL exhibits lower intensity. Also from the associated O 1s spectrum in Fig. 6.7 (b), a considerably larger amount of oxygen can be deduced. Here, the contribution of the oxygen bound to potassium appears as a shoulder of the major O 1s peak, which originates from the photoemission of the SiO_2 substrate.

The electronic structure of K-doped coronene hence reacts very sensitive on the oxidation of the dopant atoms, manifested in the occurrence of a fully extrinsic K oxide related structure in the valence band and a simultaneous intensity reduction of fL. Consequently, the K concentration does not give a proper statement about the fL filling, since the assumption of the transfer of each K 4s electron to the neighboring Cor molecule is no longer valid. Note that, regarding the K 2p core level, besides the chemical shift, the spin-orbit split peaks experience an increase in intensity relative to the intensity of C 1s. This hints to an increasing K amount at the film surface, most likely due to the formation of a K oxide overlayer or K oxide clusters. The K atoms which have previously diffused into the film, segregate to the surface again and get oxidized.

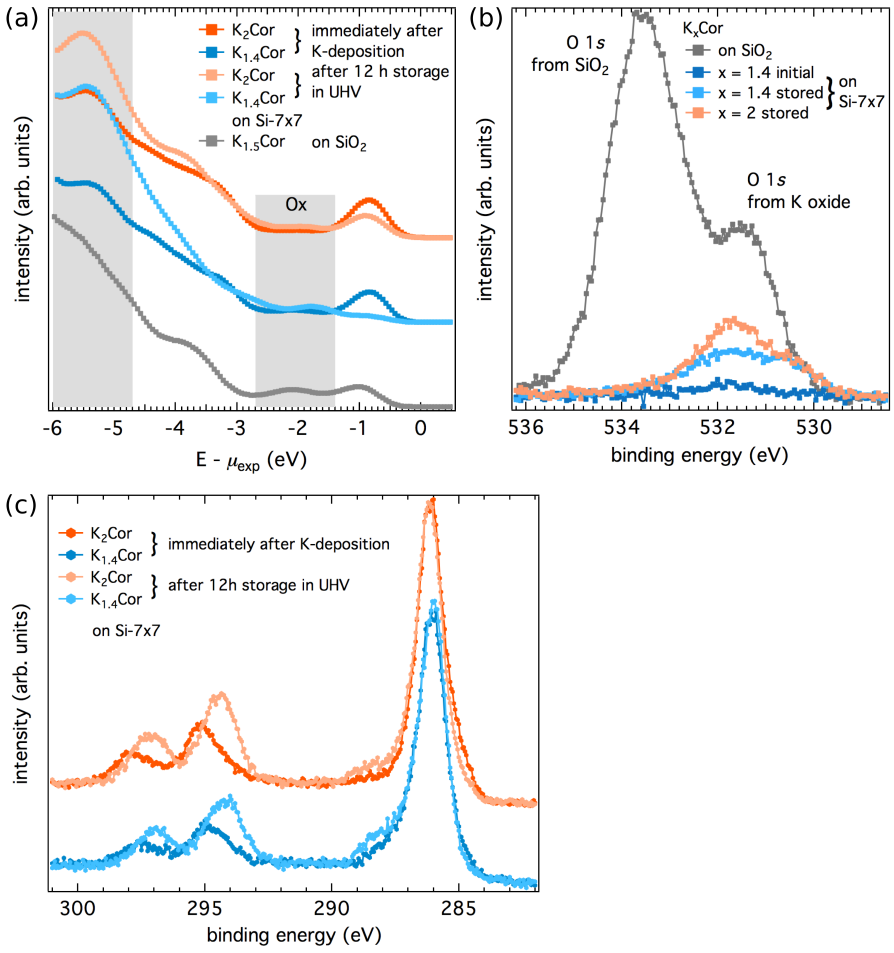

Figure 6.7: *Impact of K oxidation on the electronic structure of K_xCor. (a) Valence band spectra of K_xCor films on Si-7×7 recorded immediately after K deposition as well as after a 12 h storage in UHV. Furthermore, a spectrum of K_xCor on SiO_2 is plotted (labelled separately). (b) Corresponding O 1s (b) and K 2p as well as (c) C 1s core level spectra. Details see text.*

Finally, one can identify a small shoulder on the higher binding energy side of the C 1*s* core levels of the oxidized samples in Fig. 6.7 (c). In analogy to the C 1*s* spectra presented in the previous sections, this points to irradiation damage of the Cor molecules, which will be addressed in the next section.

6.6.2 Irradiation damage

Most of the so far presented C 1*s* core level spectra of either pristine or K-doped Cor films show a slight shoulder at the higher binding energy side with an arbitrarily varying intensity. In each case, this shoulder can be attributed to irradiation damage caused by the incident X-rays used for the XPS measurements. But not only the C 1*s* core level

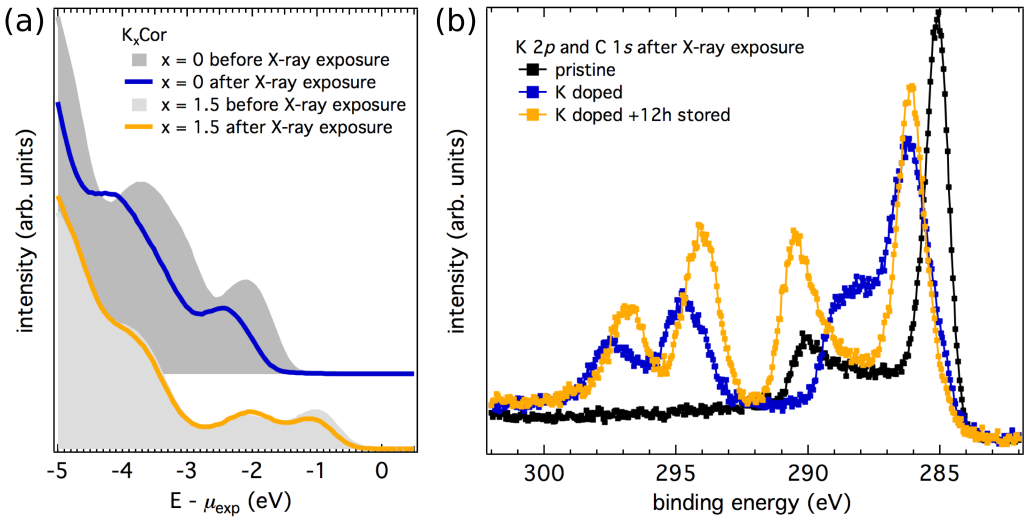

Figure 6.8: *Valence band (a) and core level photoemission spectra (b) of K_xCor for the illustration of the impact of X-ray irradiation on the electronic structure. For the UPS as well as the XPS spectra significant changes are observable upon the exposure to X-rays.*

is affected by the incident light. The valence band spectra reveal visible changes upon exposure to X-rays as well. In Fig. 6.8 (a) the changes in the valence band spectrum are illustrated for K_xCor with $x = 0$ and 1.5. Note that the UV light employed for the UPS experiments causes only marginal changes in the spectra and can be neglected for the most part. The influence of X-rays on the electronic structure of pristine Cor, in turn, manifests itself in a distinct shift of the entire spectrum as well as a loss of the pronounced structuring of the HOMO levels. Concerning K-doped Cor the changes in the spectrum are less prominent and are rather due to an enhanced oxidation of the sample.

Turning to the C 1s core level, the X-ray induced effects on the spectrum are reflected by the redistribution of spectral weight to higher binding energies with the position of the new 'peak' varying arbitrarily for different samples. Figure 6.8 (b) displays C 1s spectra for a pristine Cor film, a K-doped film, and a K-doped film which has been stored in UHV for 12 h. All samples have been irradiated with X-rays for a certain time (> 40 min). Note again the chemical shift of the K 2p core level of the 12 h stored film indicating K oxidation. In order to ascertain that the X-ray radiation is in fact responsible for the spectral changes, a time-dependent series of C 1s spectra of a pristine Cor film is plotted in Fig. 6.9. The sample has been exposed to X-rays up to 90 min. Note that the acquisition time for each spectrum was 1 min, included in the declared exposure times. It is clearly visible that the exposure to X-rays causes the occurrence of a shoulder, which gets broader upon further irradiation resulting in a extended plateau ranging from $E_{\mathrm{bind}} = 286$ to 288.5 eV. At the same time the intensity of the initial C 1s peak is reduced by the same amount implying a redistribution of spectral weight

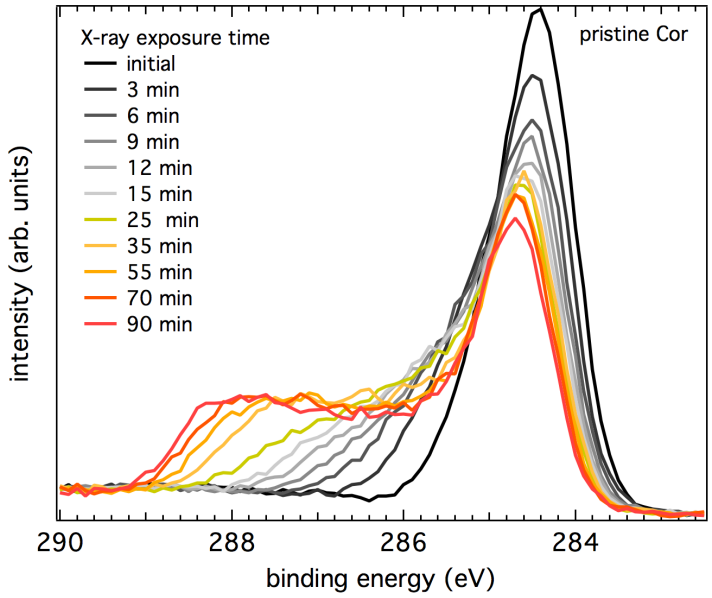

Figure 6.9: *C 1s core level spectra of a pristine Cor film depending on the time exposed to X-ray irradiation. The irradiation results in a extended plateau of spectral intensity at higher binding energy side in the spectra ranging from* $E_{bind} = 286$ *to* $288.5\,eV$.

to higher binding energies. However, the cause of the differences in the spectra from Fig. 6.8 (b) and Fig. 6.9 could not be elucidated. For the time-dependent series, no strongly pronounced peak as shown in Fig. 6.8 (b) was measured.

The observed effects on both the valence band and the C 1*s* core level are most likely caused by chemical reactions like cross-linking or breaking of bonds occurring in the Cor molecules. This results in a loss of the π-conjugated character and a modification of the chemical nature of the sample [46, 47]. Concerning the C 1*s* core level, this leads to dramatic changes of the binding energy of a large part of the involved electrons. Although these effects apparently are photon-induced, scattered photoelectrons and electrons from the secondary electron background make the greatest contribution to the damaging of the molecules [126, 127]. The additionally discernible shift in the spectra, as can be inferred from the position of the main line, might be caused, e.g., by a change in the work function or ionization potential or just by positive charging of the films due to the ejection of the photoelectrons [47].

Concluding this section, it is worth stating that special care has to be taken when conducting photoemission experiments on K_xCor. In order to be sure to probe the intrinsic electronic structure, the exposure to X-rays should be kept as short as possible to avoid massive beam damage. On the other hand, the investigation of the valence band electronic structure using UV light is largely unproblematic.

6.7 Short summary

To shortly summarize, in the chapter about Cor and its K-doped compounds it has been shown that the growth of Cor films on the substrates Si-7×7 and SiO_2 is not yet technically mature and still has to be optimized in the future. Moreover, the structural characterization proved to be difficult, most likely due to the largely unordered growth. Nonetheless, concerning the investigation of the electronic structure, the films seem to be of adequate quality since the valence band and core level spectra of pristine Cor films agree well with the literature and even exceed the quality of the reported spectra. Upon doping with potassium, besides a shift of the entire spectrum, three major effects are observable: (1) The gradual filling of the former LUMO with electrons, remarkably not accompanied with the occurrence of metallicity. (2) An energy relaxation of the HOMO due to the reorientation of the Cor molecules in the lattice. (3) The appearance of an additional peak between the relaxed HOMO and the former LUMO, which is ascribed to the photoemission of K oxide. The unexpected absence of metallicity can be explained by electronic correlations playing a crucial role in K_xCor due to a high on-molecule Coulomb repulsion compared to a very narrow band width. In this scenario the filled LUMO represents the lower Hubbard band. Owing to phase separation effects, for all probed K concentrations the same insulating behavior is observed.

Concerning the method of measurement itself, special care has to be taken to avoid the reaction of K with molecular oxygen present in the residual gas of the UHV system. Furthermore, also the use of X-rays must be handled delicately since the radiation has a visible influence on the electronic structure of K_xCor at long-time exposure.

7 Summary

The goal of this thesis was to clarify the modifications in the electronic structure of the organic semiconductors *picene*, *pentacene*, and *coronene* upon intercalation with potassium and other alkali metals in view of recent reports on superconductivity in picene and coronene and a metal-to-Mott insulator transition in pentacene. For this purpose, pristine and doped films of the respective molecules have been investigated by means of photoelectron spectroscopy.

Regarding picene, films of adequate quality have been fabricated on various substrates. The electronic properties, reflected by the photoemission spectra, turned out to be in perfect agreement with the literature confirming the high quality of the films. Doping with potassium manifests itself by the occurrence of four interesting effects: (i) Spectral weight is partly observable *above* the chemical potential in the photoemission spectra. Basis of this unusual behavior is the formation of a non-equilibrium situation between substrate and film surface. By deposition of weakly van der Waals-coupled molecules, a homogeneous chemical potential cannot be established throughout the entire film. Thus, photoemission features measured at the sample surface must not be related to the chemical potential of the reference system, i.e., the chemical potential of the spectrometer. (ii) A doping-induced feature emerges in the HOMO-LUMO gap, which is ascribed to the filling of the former LUMO. However, metallicity could not be observed for any composition of K-doped picene. Based on DFT+DMFT calculations, the insulating nature is assigned to electronic correlations playing a crucial role in this aromatic semiconductor, particularly upon doping. (iii) A further feature appears in the gap which could be traced back to the photoemission of potassium oxide. Potassium, used for doping, partly gets oxidized by molecular oxygen present in the residual gas of the UHV system. Thus, the feature is purely extrinsic. (iv) Due to the reorientation of the picene molecules in the unit cell upon dopant atom insertion the energy of the HOMO experiences a renormalization. This is reflected in a new photoemission feature close to the unreacted HOMO. Besides these four major points, additional information could be deduced from the photoemission experiments. One aspect deals with the homogeneity of the doping concentration. While the inserted potassium atoms exhibit a concentration gradient from the film surface to the substrate interface, laterally, the atoms appear to be homogeneously distributed over the film as inferred from photoemission electron microscopy. Nevertheless, phase separation occurs in the films, but on a smaller scale not covered by the insufficient spatial resolution of the microscope. Furthermore, the applied radiation used for the photoemission experiments turned out to significantly influence the electronic structure upon long-time exposure. Hence, a reasonable compromise between

acquisition time and duration of irradiation has to be found.

Concerning pentacene, also films of high quality have been prepared on different substrates. This was again validated by the well-pronounced structure in the photoemission spectra agreeing well with the literature. Very similar to picene, upon doping with various amounts of potassium all pentacene films remain insulating and display a true gap. Based on the results for picene, the insulating behavior again is assigned to the essential role of electronic correlations induced by the appropriate combination of on-molecule Coulomb repulsion and narrow bandwidths in pentacene. While a Mott metal-to-insulator transition could not be observed upon doping, as it has been proposed, the Mott insulating nature of K_1picene could be confirmed. A further important aspect was extracted from the photoemission analysis. Since the filling of the former LUMO saturates for doping concentrations larger than one K atom per molecule, it can be assumed that pentacene is able to accept only *one* additional electron.

In the case of coronene the film growth still calls for improvement. Structurally no satisfactory quality could be achieved. Nonetheless, the films yield well-shaped photoemission spectra reproducing data from the literature. Despite a different structure of the coronene molecule compared to picene and pentacene, doping with potassium has the same impact on the electronic structure. Independent of the doping concentrations the films are insulating. Again, this fact suggests the importance of electronic correlations since also in coronene the correlation strength U/W is sufficiently high. Furthermore, coronene and its doped compounds react very sensitive to the long-time exposure to X-ray and UV irradiation. Like for picene, the use of X-rays and UV light has to be dosed carefully to avoid beam damage. Moreover, also regarding $K_x$coronene, potassium easily reacts with oxygen. Reasonable measurements have to be conducted immediately after sample preparation. Storage in UHV over a long period has to be avoided.

The main striking aspect deduced from the photoemission analysis presented in this thesis is the uniform behavior of all samples upon doping. Alkali metal-doped films of picene, pentacene, and coronene are insulators independent of the doping concentrations, showing a gap in the range of $1 - 2$ eV. Remarkably, this seems to be an ubiquitous property of not only the molecules studied in this thesis, but also for a great variety of other organic systems like phthalocyanines, PTCDA, Alq_3, C_{60}, and C_{70}. Since all the organic materials exhibit narrow bandwidths and a high on-molecule Coulomb repulsion, it is conceivable that electronic correlations are the driving mechanism for these systems to be insulators.

Recalling the reported superconductivity in alkali metal-doped picene and coronene, one important question remains open: How can the insulating nature obtained from photoemission analysis be reconciled with the superconducting ground state observed in the susceptibility and transport measurements? An important aspect might be the structural difference. Photoemission has always been conducted using thin films, whereas the Meissner-Ochsenfeld effect has been observed in polycrystalline powder samples. Certainly, the alkali metal-doped polycyclic aromatic hydrocarbons remain a hotly discussed topic in the near future and more clarifying work needs to be done.

A Appendix

A.1 Substrate preparation

In this section, details about the substrate preparation are given. The following substrates have been used for growth of picene, pentacene, and coronene thin films within the framework of this thesis: natively oxidized silicon (denoted **SiO_2**), the 7×7-reconstructed surface of Si(111) (**Si-**7×7), the hydrogen-terminated surface of Si(001) (**Si-H**), thin films of bismuth on the 7×7-reconstructed surface of Si(111) (**Bi/Si**), the TiO_2-terminated (001)- surface of strontium titanate (**$SrTiO_3$**), and the Zn-terminated (0001)-surface of zinc oxide (**ZnO**).

Preparation procedures:

- **SiO_2:** Small wafer cutouts (usually $5 \times 5\,mm^2$) of natively oxidized silicon were cleaned by applying an *ex situ* three-step organic cleaning procedure. The substrates were kept in acetone, 2-propanol, and methanol in an ultrasonic bath for several minutes each and were finally blown off with high purity nitrogen. Afterwards the substrates were immediately introduced into the UHV system on a standard sample holder and directly used for film growth without any further *in situ* treatment.

- **Si-7x7:** $10 \times 2\,mm^2$ pieces of Si(111) passed the three-step organic cleaning procedure described above and were subsequently mounted on a special sample holder with the capability of direct current heating. In UHV the samples were degased using a direct current of $\sim 0.9\,A$ ($T \simeq 400°C$) for 12 h and finally 'flashed' at a current of 5.1 A ($T \simeq 1200°C$) for 10 s to remove the remaining oxide and prepare the 7×7-reconstruction.

- **Si-H:** Here, the same wafer cutouts as for SiO_2 were used and cleaned by the three-step organic treatment. Afterwards, the substrates were wet-chemically etched in buffered hydrofluoric (HF) acid for 20 s and subsequently rinsed in deionized water for 3 min to remove the oxide and achieve H-termination. Then the substrates were instantaneously brought to the UHV system and directly used for film growth.

- **Bi/Si:** Si-7×7 substrates prepared as described above served as template for thin bismuth films. The $\sim 10\,nm$ thick films were fabricated *in situ* by evaporation of high purity bismuth from a commercial effusion cell (MBE Komponenten GmbH).

- **$SrTiO_3$:** $5 \times 5\,mm^2$ pieces of as-purchased $SrTiO_3$ were first prepared by applying an *ex situ* wet-chemical etching procedure described in Ref. 184, containing treatment with buffered HF acid and deionized water as well as heating under oxygen flow. Afterwards the substrates were loaded into the UHV system and *in situ* heated to 770 K to finally remove remaining adsorbates.
- **ZnO:** Prior to loading to the UHV system, $5 \times 5mm^2$ pieces of ZnO were heated *ex situ* at ~ 1220 K under oxygen flow. Mounted on a standard sample holder the substrates were again heated *in situ* up to ~ 900 K before usage as template for film growth.

A.2 Height distribution analysis of pristine picene and pentacene films on various substrates

Pristine picene films

Figure A.1 displays the corresponding height distributions to the morphology images recorded by AFM (see Chap. 4.2). The average island height which was estimated from the respective height profiles can be quantized by the height distributions. As the distribution should exhibit a Gaussian shape, an appropriate curve adapted to the data is added to the graphs. The average island heights are ~ 55 nm for films on SiO_2, ~ 30 nm (on Si-7x7), ~ 50 nm (on ZnO), ~ 40 nm (on $SrTiO_3$), and ~ 15 nm for films on Bi/Si.

Pristine pentacene films

Similar to the data analysis for picene, Fig. A.2 displays the height distributions deduced from the morphology images recorded by AFM illustrated in Chap. 5.2. All height distributions are plotted together with a conforming Gaussian shape. The resulting average island heights are ~ 20 nm for films on SiO_2, ~ 15 nm (on Si-H and $SrTiO_3$), and ~ 25 nm for films on ZnO. In the height distributions of Pn films on $SrTiO_3$ and ZnO one can clearly observe local maxima reflecting the mono-molecular steps characteristic for growth in standing mode.

A.3 Calibration of the K concentration via K_3C_{60}

A general problem with samples of a certain unknown stoichiometry is the determination of the actual composition. In the particular case of the $K_x$picene powder samples of, e.g., Mitsuhashi *et al.* this has been achieved by using nominal compositions given by the weight of the constituents [7]. A different possibility, especially for the characterization of thin films, is Rutherford backscattering spectroscopy, as used by Craciun *et al.*

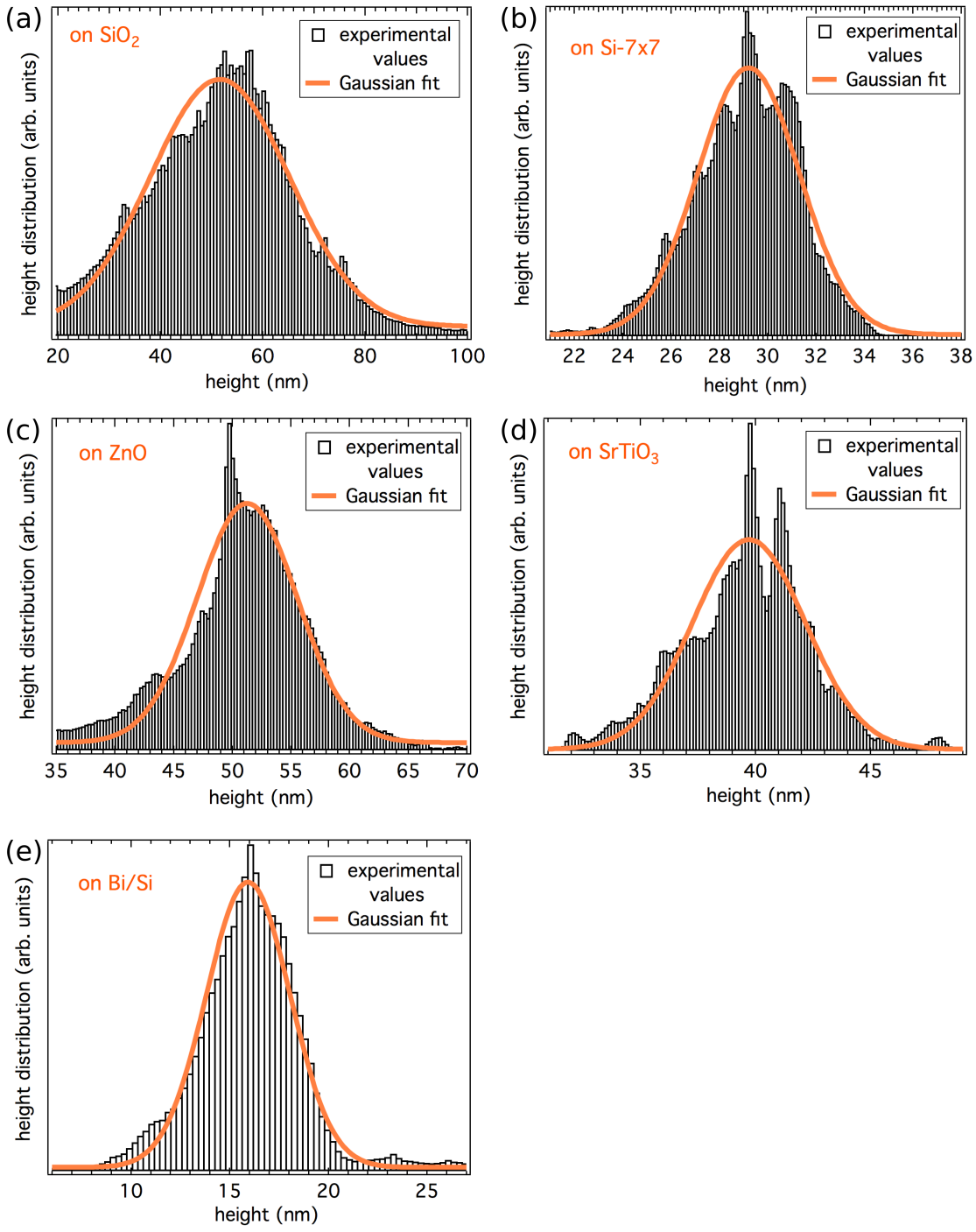

Figure A.1: *Height distributions of picene films on (a) SiO_2, (b) Si-7x7, (c) ZnO, (d) $SrTiO_3$, and (e) Bi/Si. Data are deduced from the morphology images recorded by means of AFM.*

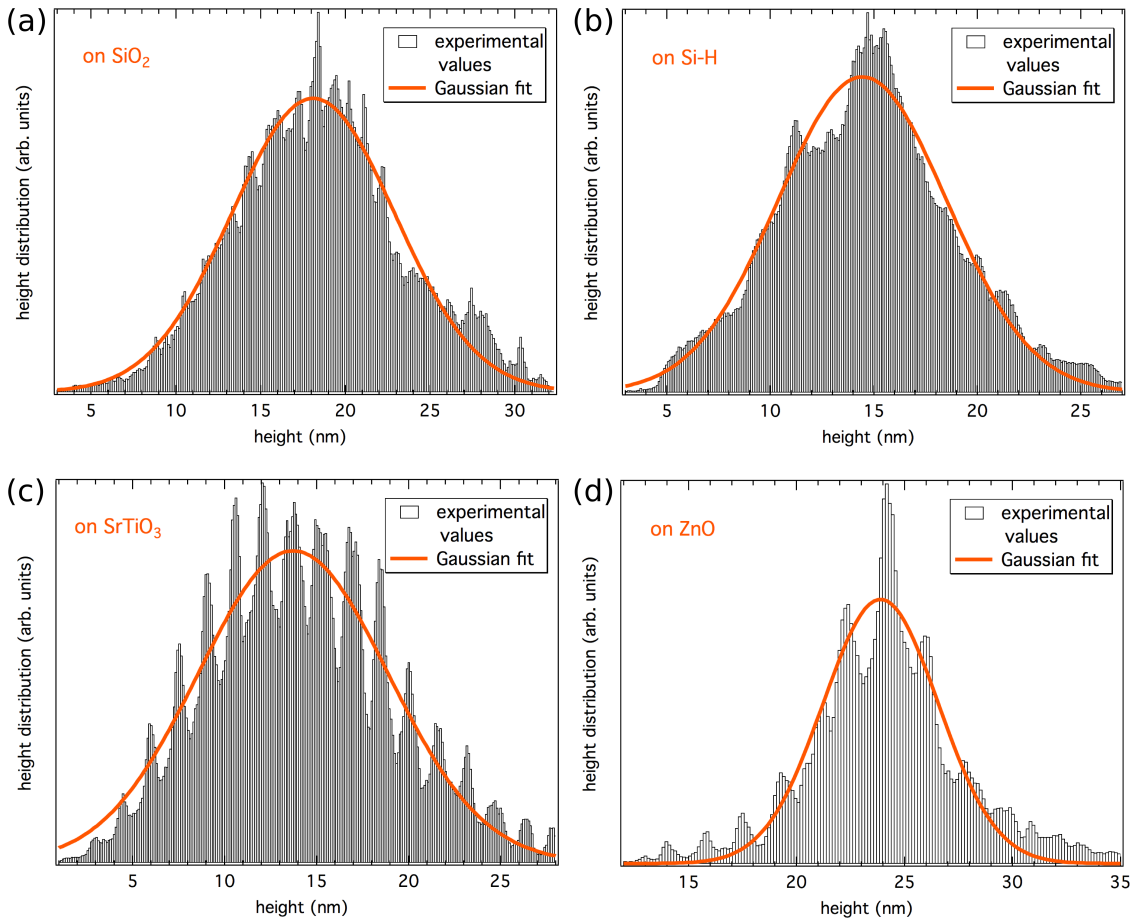

Figure A.2: *Height distributions of pentacene films on (a) SiO_2, (b) Si-H, (c) $SrTiO_3$, and (d) ZnO. Data are deduced from the morphology images recorded by means of AFM.*

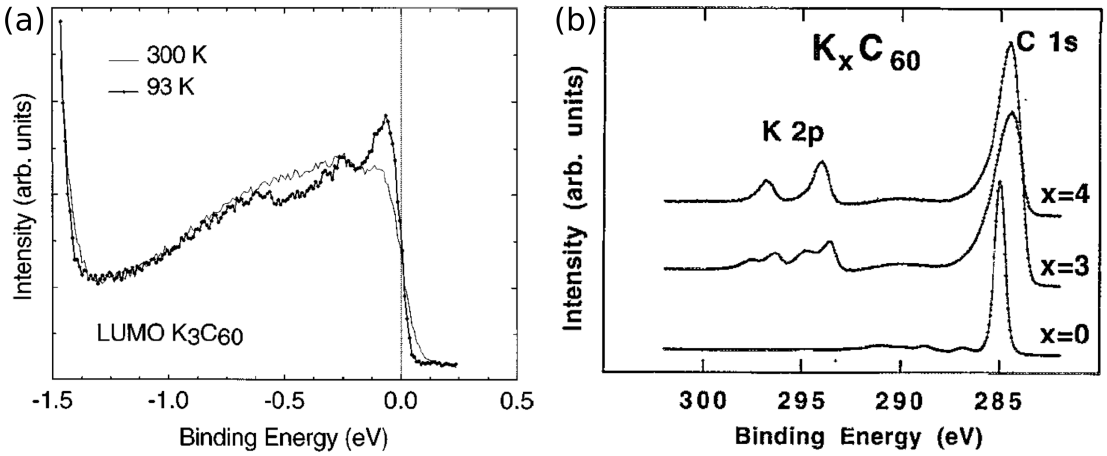

Figure A.3: *(a) Valence band photoemission from K_3C_{60} for room temperature and 93 K from Goldoni et al. Figure reprinted from Ref. 138 with permission from A. Goldoni. Copyright (2013) by The American Physical Society. (b) Core level spectra of different phase pure K_xC_{60} compounds from Poirier et al. Figure reprinted from Ref. 120, Copyright (2013), with permission from AIP Publishing.*

for identifying the potassium amount in $K_x$pentacene films [15]. Most groups who investigate alkali metal-doped organic samples by means of photoelectron spectroscopy determine the stoichiometry by comparing the core level spectra of the corresponding alkali metal and carbon. Doping with potassium provides an advantageous situation since the relevant core levels K $2p$ and C $1s$ are energetically separated by only a few eV. For similar kinetic energies, the energy dependent inelastic mean free path of the escaping electrons does not differ much between K and C (see Chap. 3.2.3). Thus, the electrons essentially stem from the same volume of the sample allowing for better comparability. Besides the IMFP and the analyzer transmission the most important parameters in Eq. 3.17 in Chap. 3.2.4 are the photoionization cross-sections. Usually they are obtained from Yeh and Lindau [59] who provide calculated photoionization cross-sections for single free atoms which are, in turn, not necessarily correct for solids and films. To achieve a better estimate of the photoionization cross-sections, one can use an easily reproducible reference system of well-defined stoichiometry, e.g., K_3C_{60}. Phase-pure K_3C_{60} can be fabricated following the *vacuum distillation technique* [120, 185]. The phase purity can be checked by the metallic DOS in valence band photoemission since K_3C_{60} is the only K-doped C_{60}-phase exhibiting metallicity. Exemplarily, corresponding valence band spectra from Goldoni *et al.* [138] recorded at room temperature and at 93 K as well as core level spectra from Poirier *et al.* [120] for different K concentrations are shown in Fig. A.3.

The observable energy splitting of the K $2p$ core level of K_3C_{60} results from different positions of the K atoms in the lattice. K atoms are placed in octahedral as well as tetrahedral interstitials of the fcc-lattice of C_{60}. Following the recipe from Poirier *et al.*,

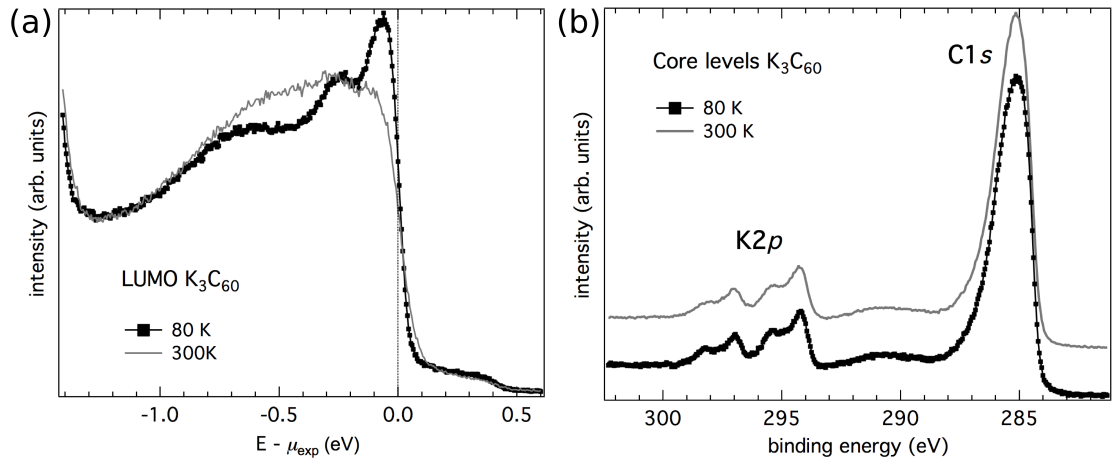

Figure A.4: *(a) Valence band photoemission from K_3C_{60} fabricated by the vacuum distillation technique. Spectra are shown for room temperature and LN_2 cooling (80 K). (b) Corresponding core level spectra for room temperature and 80 K.*

K_3C_{60} films have been fabricated on GaAs substrates. The resulting valence band and core level spectra from UPS and XPS, respectively, are displayed in Fig. A.4. Both, the valence band and the energy range containing K 2*p* and C 1*s* core levels have been recorded at room temperature and at 80 K (LN_2 cooling). Figure A.4 (a) clearly shows the metallic nature of the K_3C_{60} films reflected by the sharp Fermi cut-off for both temperatures. Except for the contribution of He $I_{\beta,\gamma}$-satellites the spectra are in perfect agreement with the literature demonstrating the easy reproducibility of this special C_{60}-phase. Also the core level spectra in Fig. A.4 (b) are in excellent agreement with the previously reported data.

Since the correct stoichiometry is known due to the phase pure fabrication of the samples, it can be used to recalibrate the calculated photoionization cross-sections from Yeh and Lindau. Using the cross-sections from Ref. 59 to determine the K concentration x in K_xC_{60} obviously results in an incorrect stoichiometry. Table A.1 contains the determined K concentrations x for two different samples (fabricated by the *vacuum distillation technique*) measured at 80 and 300 K, respectively. Furthermore, the corresponding cross-section ratio $(\sigma_{C1s}/\sigma_{K2p})^*$ is listed as obtained by using the calculated cross-sections from Yeh and Lindau. In order to correctly reproduce the $x = 3$ phase in the determination of the stoichiometry, the cross-section ratio has to be adjusted. In Tab. A.1 the adjusted cross-section ratio $(\sigma_{C1s}/\sigma_{K2p})^{**}$, leading to a K concentration of $x = 3$ using Eq. 3.17, is included. Note that using the calculated cross-sections from Ref. 59 overestimates the actual K concentration by $\sim 30\,\%$ as can be seen from Tab. A.1.

Besides $(\sigma_{C1s}/\sigma_{K2p})$, in Eq. 3.17 in Chap. 3.2.4 also the asymmetry function containing the asymmetry parameter β has to be taken into account. Tentative changes in the asymmetry parameter compared to the calculated values from Yeh and Lindau are not considered separately, but are covered in $(\sigma_{C1s}/\sigma_{K2p})^{**}$. Since the cross-section ratio

Table A.1: *Determined K concentration x in K_xC_{60} for two different samples at 80 and 300 K using calculated cross-sections from Ref. 59. $(\sigma_{C1s}/\sigma_{K2p})$: cross-section ratio of K 2p and C 1s core levels.*

* *using calculated values from Ref. 59*

** *recalibrated cross-section ratio for obtaining $x = 3$*

	x at 80 K	x at 300 K	$(\sigma_{C1s}/\sigma_{K2p})^*$	$(\sigma_{C1s}/\sigma_{K2p})^{**}$
sample 1	3.95	3.84	0.2453	0.1865
sample 2	3.93	3.80	0.2453	0.1873

has been calibrated on K_3C_{60} it is still error-prone concerning $K_x$picene, $K_x$pentacene, and $K_x$coronene but a considerably better estimate than using the values from Ref. 59. Thus, in the framework of this thesis, all declared K concentrations are based on the calibration described above.

A.4 Photoemission of potassium oxide

In conjunction with the findings described in Chap. 4.4.3 some details on the photoemission of potassium oxide shall be discussed here. In general, three different species of potassium oxide can be formed by the reaction of potassium with oxygen. These are potassium oxide (K_2O), peroxide (K_2O_2), and superoxide (KO_2), involving O^{2-}, O_2^{2-}, and O_2^- ions, respectively [128, 186]. K_2O is considerably unstable and occurs solely for a low oxygen quantity compared to the available potassium amount. The most stable phase is K_2O_2 which oxidizes further to KO_2 only for high oxygen dosing. From the literature several studies are known which investigate the oxidation of pure potassium films by means of photoelectron spectroscopy [122, 187–191] and thus are helpful in identifying the feature F_2 in the spectra presented in this thesis. Qiu *et al.* [122] present core level and valence band spectra for K oxide films in a large range of oxygen dosing as shown in Fig. A.5. Note that the measurements have been conducted at low temperature (35 K).

In Fig. A.5 (a) the O 1*s* core level spectrum for the case of oxidized potassium is highlighted by the box. Several peaks can be identified and are unambiguously assigned to the corresponding oxygen ions in Refs. 122 and 192. The highest binding energy feature at ~ -541 eV is attributed to the presence of molecular oxygen O_2 adsorbed on the surface of the samples under investigation. Within the energy range of -536 eV to -526 eV one can identify the emission from the different species described above. Only present as a shoulder at ~ -535 eV of the pronounced peak is the contribution of potassium superoxide KO_2 superimposed by the emission from the peroxide K_2O_2 at -533 eV contributing the most to the observed spectrum. A further distinct peak is located at ~ -528 eV reflecting the existence of potassium oxide K_2O. Extracted from

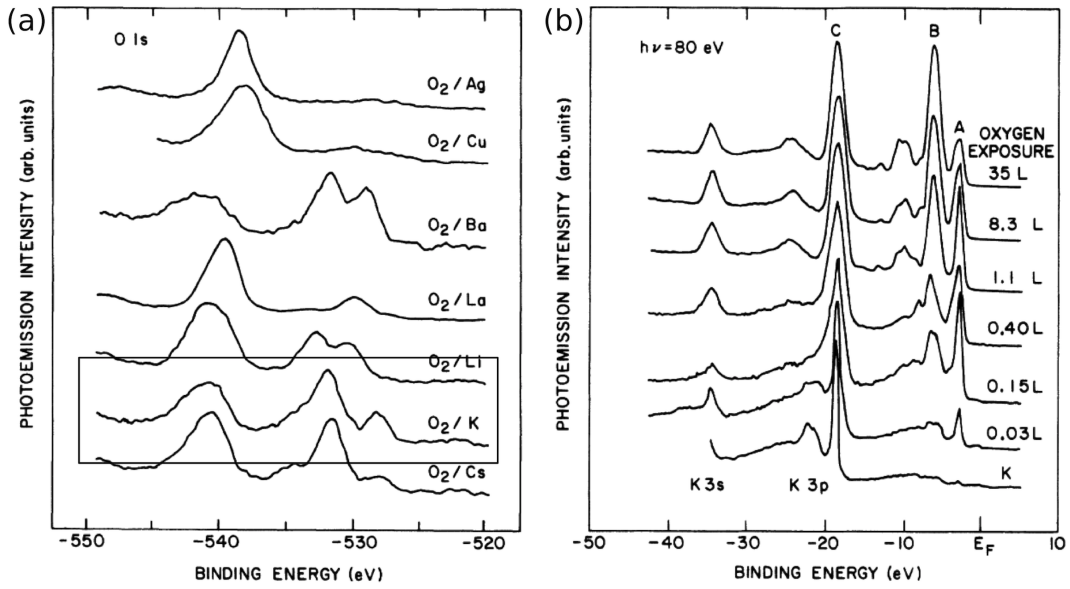

Figure A.5: *(a) O 1s core level spectra for various oxidized alkali metals. The important case of potassium is highlighted by the box. (b) Valence band spectra of K oxide for different amounts of oxygen exposure. Figures reprinted from Ref. 122 with permission from M. Strongin. Copyright (2013) by The American Physical Society.*

the measurements in this thesis the binding energy of the O 1*s* core level lies in the range of $531 - 532\,\mathrm{eV}$. This value agrees well with the one given for K_2O_2 in Ref. 122. Furthermore, due to the appearance of only a single peak in the entire spectrum the presence of KO_2 and K_2O can be excluded, since the oxygen dosing was not high enough to generate the former one and the formation of the latter one is rather unlikely at room temperature.

Considering the valence band spectra in Fig. A.5 (b), one can basically observe the evolution of two features (labelled A and B) upon oxygen dosing. An unambiguous classification of the peaks is not possible in this case. Nonetheless, the authors of Ref. 122 ascribe feature A to the formation of K_2O and B to the formation of K_2O_2 when more oxygen is available. Note, however, that for highly oxygen dosed films feature A does not vanish. Conclusively, a clear distinction between the two features, unambiguously reflecting a certain oxidation state, cannot be made. Both features have their origin in the formation of a 'potassium oxide'. Here, the peak positions of A and B, and more significantly the relative energy distance, coincide with F_2 and the second newly evolving feature upon oxygen exposure in the valence band data in this thesis.

Similar behavior as observed for $K_x$picene has previously been reported for potassium doped fullerenes (K_xC_{60}) in the particular case of heavily overdoped films ($K_{11.5}C_{60}$) measured under UHV conditions [190], indicating that oxidation always represents a problem when conducting experiments containing alkali metals.

Bibliography

[1] D. Gundlach, *Organic electronics: Low power, high impact*, Nature Mater. **6**, 173 (2007).

[2] C. Melzer and H. von Seggern, *Organic electronics: Enlightened organic transistors*, Nature Mater. **9**, 470 (2010).

[3] I. Mcculloch, *Thin films: Rolling out organic electronics*, Nature Mater. **4**, 583 (2005).

[4] M. Berggren, D. Nilsson and N. Robinson, *Organic materials for printed electronics*, Nature M **6**, 3 (2007).

[5] N. Toyota, M. Lang and J. Müller, *Low-Dimensional Molecular Metals*, Springer-Verlag Berlin Heidelberg (2007).

[6] T. Palstra, O. Zhou, Y. Iwasa, P. Sulewski, R. Fleming and B. Zegarski, *Superconductivity at 40 K in cesium doped C_{60}*, Solid State Commun. **93**, 327 (1995).

[7] R. Mitsuhashi, Y. Suzuki, Y. Yamanari, H. Mitamura, T. Kambe, N. Ikeda, H. Okamoto, A. Fujiwara, M. Yamaji, N. Kawasaki, Y. Maniwa and Y. Kubozono, *Superconductivity in alkali-metal-doped picene*, Nature **464**, 76 (2010).

[8] X. Wang, R. Liu, Z. Gui, Y. Xie, Y. Yan, J. Ying, X. Luo and X. Chen, *Superconductivity at 5 K in alkali-metal-doped phenanthrene*, Nat. Commun. **2**, 507 (2011).

[9] X. Wang, Y. Yan, Z. Gui, R. Liu, J. Ying, X. Luo and X. Chen, *Superconductivity in $A_{1.5}$phenanthrene (A=Sr,Ba)*, Phys. Rev. B **84**, 214523 (2011).

[10] Y. Kubozono, H. Mitamura, X. Lee, X. He, Y. Yamanari, Y. Takahashi, Y. Suzuki, Y. Kaji, R. Eguchi, K. Akaike, T. Kambe, H. Okamoto, A. Fujiwara, T. Kato, T. Kosugi and H. Aoki, *Metal-intercalated aromatic hydrocarbons: a new class of carbon-based superconductors*, Phys. Chem. Chem. Phys. **13**, 16476 (2011).

[11] M. Xue, T. Cao, D. Wang, Y. Wu, H. Yang, X. Dong, J. He, F. Li and G. Chen, *Superconductivity above 30 K in alkali-metal-doped hydrocarbons*, Sci. Rep. **2**, 389 (2012).

[12] K. Teranishi, X. He, Y. Sakai, M. Izumi, H. Goto, R. Eguchi, Y. Takabayashi, T. Kambe and Y. Kubozono, *Observation of zero resistivity in K-doped picene*, Phys. Rev. B **87**, 060505(R) (2013).

[13] M. Capone, M. Fabrizio, C. Castellani and E. Tosatti, *Strongly correlated superconductivity*, Science **296**, 2364 (2002).

[14] B. Powell and R. McKenzie, *Quantum frustration in organic Mott insulators: from spin liquids to unconventional superconductors*, Rep. Prog. Phys. **74**, 056501 (2011).

[15] M. F. Craciun, G. Giovanetti, S. Rogge, G. Brocks, A. F. Morpurgo and J. van den Brink, *Evidence for the formation of a Mott state in potassium-intercalated pentacene*, Phys. Rev. B. **79**, 125116 (2009).

[16] S. Hino, K. Matsumoto, S. Hasegawa, K. Kamiya, H. Inokuchi, T. Morikawa, T. Takahashi, K. Seki, K. Kikuchi, S. Suzuki, I. Ikemoto and Y. Achiba, *Ultraviolet photoelectron spectra of C_{84} and K_xC_{84}*, Chem. Phys. Lett. **190**, 169 (1992).

[17] M. Knupfer, D. Poirier and J. Weaver, *K-C_{70}: Stable phases and electronic structures*, Phys. Rev. B **49**, 8464 (1994).

[18] A. Ito, O. Akaki and T. Takahashi, *Photoemission study of K- and Sc-doped C_{84}*, J. Electron. Spectrosc. Rel. Phenom. **78**, 457 (1996).

[19] T. Schwieger, H. Peisert, M. Knupfer, M. S. Golden and J. Fink, *Electronic structure of K-intercalated 8-tris-hydroxyquinoline aluminum studied by photoemission spectroscopy*, Phys. Rev. B **63**, 165104 (2001).

[20] T. Schwieger, H. Peisert, M. S. Golden, M. Knupfer and J. Fink, *Electronic structure of the organic semiconductor copper phthalocyanine and K-CuPc studied using photoemission spectroscopy*, Phys. Rev. B **66**, 155207 (2002).

[21] N. Koch, J. Ghijsen, R. L. Johnson, J. Schwartz, J.-J. Pireaux and A. Kahn, *Physisorption-like interaction at the interfaces formed by pentacene and samarium*, J. Phys. Chem. B **106**, 4192 (2002).

[22] O. V. Molodtsova, V. M. Zhilin, D. V. Vyalikh, V. Y. Aristov and M. Knupfer, *Electronic properties of potassium-doped CuPc*, J. Appl. Phys. **98**, 093702 (2005).

[23] H. Ding and Y. Gao, *Alkali metal doping and energy level shift in organic semiconductors*, Appl. Surf. Sci. **252**, 3943 (2006).

[24] G. G. Fuentes and M. Knupfer, *Electronic structure and work function of potassium-doped PTCDA thin films*, Appl. Phys. A **84**, 329 (2006).

[25] H. Ding, K. Park and Y. Gao, *Evolution of the unoccupied states in alkali metal-doped organic semiconductor*, J. Electron. Spectrosc. Relat. Phenom. **174**, 45 (2009).

[26] F. Bussolotti, S. Kera and N. Ueno, *Potassium doping of single crystalline pentacene thin film*, Phys. Rev. B **86**, 155120 (2012).

[27] N. Ashcroft and N. Mermin, *Solid State Physics*, Cengage Learning, Brooks/Cole (1976).

[28] J. de Boer and E. Verwey, *Semi-conductors with partially and with completely filled 3d-lattice bands*, Proc. Phys. Soc. **49**, 59 (1937).

[29] N. Mott, *Discussion of the paper by de Boer and Verwey*, Proc. Phys. Soc. **49**, 72 (1937).

[30] N. Mott, *The basis of the electron theory of metals, with special reference to the transition metals*, Proc. Phys. Soc. A **62**, 416 (1949).

[31] N. Mott, *The transition to the metallic state*, Philosophical Magazine **6**, 287 (1961).

[32] J. Hubbard, *Electron correlations in narrow energy bands*, Proc. R. Soc. Lond. A **276**, 238 (1963).

[33] M. Gutzwiller, *Effect of correlation on the ferromagnetism of transition metals*, Phys. Rev. Lett. **10**, 159 (1963).

[34] J. Kanamori, *Electron correlation and ferromagnetism of transition metals*, Prog. Theor. Phys. **30**, 275 (1963).

[35] A. Georges, G. Kotliar, W. Krauth and M. Rozenberg, *Dynamical mean-field theory of strongly correlated fermion systems and the limit of infinite dimensions*, Rev. Mod. Phys. **68**, 13 (1996).

[36] R. Bulla (2001), private communications, see also Ref. 193.

[37] P. Hohenberg and W. Kohn, *Inhomogeneous electron gas*, Phys. Rev. **136**, B864 (1964).

[38] G. Kotliar and D. Vollhardt, *Strongly correlated materials: insight from dynamical mean-field theory*, Phys. Today **57**, 53 (2004).

[39] W. Kohn and L. Sham, *Self-consistent equations including exchange and correlation effects*, Phys. Rev. **140**, A1133 (1965).

[40] D. Langreth and M. Mehl, *Beyond the local-density approximation in calculations of ground-state electronic properties*, Phys. Rev. B **28**, 1809 (1983).

[41] W. Metzner and D. Vollhardt, *Correlated lattice fermions in d=∞ dimensions*, Phys. Rev. Lett. **62**, 324 (1989).

[42] A. Georges and G. Kotliar, *Hubbard model in infinite dimensions*, Phys. Rev. B **45**, 6479 (1992).

[43] S. Hüfner, *Photoelectron Spectroscopy. Principles and Applications, 3rd ed.*, Springer-Verlag Berlin Heidelberg New York (2003).

[44] A. Damascelli, *Probing the electronic structure of complex systems by ARPES*, Physica Scripta **T109**, 61 (2004).

[45] F. Reinert and S. Hüfner, *Photoemission spectroscopy – from early days to recent applications*, New J. Phys. **7**, 97 (2005).

[46] K. Okudaira, S. Hasegawa, P. Sprunger, E. Morikawa, V. Saile, K. Seki, Y. Harada and N. Ueno, *Photoemission study of pristine and photodegraded poly(methyl methacrylate)*, J. Appl. Phys. **83**, 4292 (1998).

[47] N. Koch, D. Pop, R. Weber, N. Böwering, B. Winter, M. Wick, G. Leising, I. Hertel and W. Braun, *Radiation induced degradation and surface charging of organic thin films in ultraviolet photoemission spectroscopy*, Thin Solid Films **391**, 81 (2001).

[48] K. Siegbahn, *Electron spectroscopy for atoms, molecules, and condensed matter*, Science **217**, 111 (1982).

[49] H. Hertz, *Ueber einen Einfluss des ultravioletten Lichtes auf die elektrische Entladung*, Ann. Phys. **267**, 983 (1887).

[50] A. Einstein, *Über einen die Erzeugung und Verwandlung des Lichtes betreffenden heuristischen Gesichtspunkt*, Ann. Phys. **322**, 132 (1905).

[51] S. Doniach and M. Sunjic, *Many-electron singularity in X-ray photoemission and X-ray line spectra from metals*, J. Phys. C.: Solid State Phys. **3**, 285 (1970).

[52] S. Hüfner, R. Claessen, F. Reinert, T. Straub, V. Strocov and P. Steiner, *Photoemission spectroscopy in metals: band structure-Fermi surface-spectral function*, J. Electron. Spectrosc. Rel. Phenom. **100**, 191 (1999).

[53] A. Damascelli, Z. Hussain and Z.-X. Shen, *Angle-resolved photoemission studies of the cuprate superconductors*, Rev. Mod. Phys. **75**, 473 (2003).

[54] D. Shirley, *High-resolution X-ray photoemission spectrum of the valence bands of gold*, Phys. Rev. B **5**, 4709 (1972).

[55] M. Seah and W. Dench, *Quantitative electron spectroscopy of surfaces: A standard data base for electron inelastic mean free paths in solids*, Surf. Interface Anal. **1**, 2 (1979).

[56] S. Tanuma, C. Powell and D. Penn, *Calculations of electron inelastic mean free paths. V. Data for 14 organic compounds over the 50-2000 eV range*, Surf. Interface Anal. **21**, 165 (1994).

[57] P. Cumpson and M. Seah, *Elastic scattering corrections in AES and XPS. II. Estimating attenuation lengths and conditions required for their valid use in overlayer/substrate experiments*, Surf. Interface Anal. **25**, 430 (1997).

[58] S. Tanuma, C. Powell and D. Penn, *Calculation of electron inelastic mean free paths (IMFPs) VII. Reliability of the TPP-2M IMFP predictive equation*, Surf. Interface Anal. **35**, 268 (2003).

[59] J. J. Yeh and I. Lindau, *Atomic subshell photoionization cross sections and asymmetry parameters:* $1 \leq Z \leq 103$, Atom. Data Nucl. Data **32**, 1 (1985).

[60] M. Trzhaskovskaya, V. Nefedov and V. Yarzhemsky, *Photoelectron angular distribution parameters for elements Z=1 to Z=54 in the photoelectron energy range 100-5000 eV*, At. Data Nucl. Data Tables **77**, 97 (2001).

[61] P. Ruffieux, P. Schwaller, O. Gröning, L. Schlappbach, P. Gröning, Q. Herd, D. Funnemann and J. Westermann, *Experimental determination of the transmission factor for the Omicron EA125 electron analyzer*, Rev. Sci. Instrum. **71**, 3634 (2000).

[62] D. Briggs and M. Seah, *Practical Surface Analysis: Auger and X-ray Photoelectron Spectroscopy*, Wiley & Sons (1990).

[63] D. Phillips, *Polynuclear aromatic hydrocarbons. I. A new synthesis of picene*, J. Am. Chem. Soc. **75**, 3223 (1953).

[64] A. De, R. Gosh, S. Roychowdhury and P. Roychowdhury, *Structural analysis of picene,* $C_{22}H_{14}$, Acta Chryst. **C41**, 907 (1985).

[65] H. Okamoto, N. Kawasaki, Y. Kaji, Y. Kubozono, A. Fujiwara and M. Yamaji, *Air-assisted high-performance field-effect transistor with thin films of picene*, J. Am. Chem. Soc. **130**, 10470 (2008).

[66] Y. Kaji, N. Kawasaki, X. Lee, H. Okamoto, Y. Sugawara, S. Oikawa, A. Ito, H. Okazaki, T. Yokoya, A. Fujiwara and Y. Kubozono, *Low voltage operation in picene thin film field-effect transistor and its physical characteristics*, Appl. Phys. Lett. **95**, 183302 (2009).

[67] Y. Kaji, R. Mitsuhashi, X. Lee, H. Okamoto, T. Kambe, N. Ikeda, A. Fujiwara, M. Yamaji, K. Omote and Y. Kubozono, *High-performance C_{60} and picene thin film field-effect transistors with conducting polymer electrodes in bottom contact structures*, Org. Electron. **10**, 432 (2009).

[68] N. Kawasaki, Y. Kubozono, H. Okamoto, A. Fujiwara and M. Yamaji, *Trap states and transport characteristics in picene thin film field-effect transistors*, Appl. Phys. Lett. **94**, 043310 (2009).

[69] N. Kawasaki, W. Kalb, T. Mathis, Y. Kaji, R. Mitsuhashi, H. Okamoto, Y. Sugawara, A. Fujiwara, Y. Kubozono and B. Batlogg, *Flexible picene thin film field-effect transistors with parylene gate dielectric and their physical properties*, Appl. Phys. Lett. **96**, 113305 (2010).

[70] N. Kawai, R. Eguchi, H. Goto, K. Akaike, Y. Kaji, T. Kambe, A. Fujiwara and Y. Kubozono, *Characteristics of single crystal field-effect transistors with a new typo of aromatic hydrocarbon, picene*, J. Phys. Chem. C **116**, 7983 (2012).

[71] T. Kosugi, T. Miyake, S. Ishibashi, R. Arita and H. Aoki, *First-principles electronic structure of solid picene*, J. Phys. Soc. Jpn. **78**, 113704 (2009).

[72] P. de Andres, A. Guijarro and J. Vergés, *Crystal structure and electronic states of tripotassium picene*, Phys. Rev. B **83**, 245113 (2011).

[73] T. Kosugi, T. Miyake, S. Ishibashi, R. Arita and H. Aoki, *First-principles structural optimization and electronic structure of the superconductor picene for various potassium doping levels*, Phys. Rev. B **84**, 214506 (2011).

[74] Y. Nomura, K. Nakamura and R. Arita, *Ab initio derivation of electronic low-energy models for C_{60} and aromatic compounds*, Phys. Rev. B **85**, 155452 (2012).

[75] A. Subedi and L. Boeri, *Vibrational spectrum and electron-phonon coupling of doped solid picene from first principles*, Phys. Rev. B **84**, 020508(R) (2011).

[76] T. Kato, T. Kambe and Y. Kubozono, *Strong intramolecular electron-phonon coupling in the negatively charged aromatic superconductor picene*, Phys. Rev. Lett. **107**, 077001 (2011).

[77] M. Casula, M. Calandra, G. Profeta and F. Mauri, *Intercalant and intermolecular phonon assisted superconductivity in K-doped picene*, Phys. Rev. Lett. **107**, 137006 (2011).

[78] A. Girlando, M. Masino, I. Bilotti, A. Brillante and R. D. V. E. Venuti, *Phonon dynamics and electron-phonon coupling in pristine picene*, Phys. Chem. Chem. Phys. **14**, 1694 (2012).

[79] B. Joseph, L. Boeri, L. Malavasi, F. Capitani, G. Artioli, S. Protti, M. Fagnoni, A. Albini, C. Marini, L. Baldassarre, A. Perucchi, S. Lupi, P. Postorino and P. Dore, *Vibrational spectrum of solid picene ($C_{22}H_{14}$)*, J. Phys.: Condens. Matter **24**, 252203 (2012).

[80] T. Sato, N. Iwahara and K. Tanaka, *Critical reinvestigation of vibronic couplings in picene from view of vibronic coupling density analysis*, Phys. Rev. B **85**, 161102(R) (2012).

[81] M. Casula, M. Calandra and F. Mauri, *Local and nonlocal electron-phonon couplings in K_3 picene and the effect of metallic screening*, Phys. Rev. B **86**, 075445 (2012).

[82] M. Kim, B. Min, G. Lee, H. Kwon, Y. Rhee and J. Shim, *Density functional calculations of electronic structure and magnetic properties of the hydrocarbon K_3picene superconductor near the metal-insulator transition*, Phys. Rev. B **83**, 214510 (2011).

[83] G. Giovanetti and M. Capone, *Electron correlation effects in superconducting picene from ab initio calculations*, Phys. Rev. B **83**, 134508 (2011).

[84] H. Okazaki, T. Wakita, T. Muro, Y. Kaji, X. Lee, H. Mitamura, N. Kawasaki, Y. Kubozono, Y. Yamanari, T. Kambe, T. Kato, M. Hirai, Y. Muraoka and T. Yokoya, *Electronic structure of pristine and K-doped solid picene: Nonrigid band change and its implication for electron-intramolecular-vibration interaction*, Phys. Rev. B **82**, 195114 (2010).

[85] B. Mahns, F. Roth and M. Knupfer, *Absence of photoemission from the Fermi level in potassium intercalated picene and coronene films: Structure, polaron, or correlation physics?*, J. Chem. Phys. **136**, 134503 (2012).

[86] M. Caputo, G. D. Santo, P. Parisse, L. Petaccia, L. Floreano, A. Verdini, M. Panighel, C. Struzzi, B. Taleatu, C. Lal and A. Goldoni, *Experimental study of pristine and alkali metal doped picene layers: Confirmation of the insulating phase in multilayer doped compounds*, J. Phys. Chem. C **116**, 19902 (2012).

[87] H. Jeschke, M. Tomić, H. Lee and R. Valentí, *Structure of alkali metal-doped picene from DFT* (2012), to be published.

[88] J. Fraxedas, *Molecular Organic Materials - From Molecules to Crystalline Solids*, Cambridge University Press (2006).

[89] F. Roth, M. Gatti, P. Cudazzo, M. Grobosch, B. Mahns, B. Büchner, A. Rubio and M. Knupfer, *Electronic properties of molecular solids: the peculiar case of solid picene*, New J. Phys. **12**, 103036 (2010).

[90] G. Kresse and J. Hafner, *Ab initio molecular dynamics for liquid metals*, Phys. Rev. B **47**, 558 (1993).

[91] G. Kresse and J. Furthmüller, *Efficient iterative schemes for ab initio total-energy calculations using a plane-wave basis set*, Phys. Rev. B **54**, 11169 (1996).

[92] P. E. Blöchl, *Projector augmented-wave method*, Phys. Rev. B **50**, 17953 (1994).

[93] G. Kresse and D. Joubert, *From ultrasoft pseudopotentials to the projector augmented-wave method*, Phys. Rev. B **59**, 1758 (1999).

[94] T. Hosokai, A. Hinderhofer, A. Vorobiev, C. Lorch, T. Watanabe, T. Koganezawa, A. Gerlach, N. Yoshimoto, Y. Kubozono and F. Schreiber, *In situ structural characterization of picene thin films by X-ray scattering: Vacuum versus O_2 atmosphere*, Chem. Phys. Lett. **544**, 34 (2012).

[95] J. Sadowski, G. Sazaki, S. Nishikata, A. Al-Mahboob, Y. Fujikawa, K. Nakajima, R. Tromp and T. Sakurai, *Single-nucleus polycrystallization in thin film epitaxial growth*, Phys. Rev. Lett. **98**, 046104 (2007).

[96] Q. Xin, S. Duhm, F. Bussolotti, K. Akaike, Y. Kubozono, H. Aoki, T. Kosugi, S. Kera and N. Ueno, *Accessing surface brillouin zone and band structure of picene single crystals*, Phys. Rev. Lett. **108**, 226401 (2012).

[97] H. Ishii, K. Sugiyama, E. Ito and K. Seki, *Energy level alignment and interfacial electronic structures at organic/metal and organic/organic interfaces*, Adv. Mater. **11**, 605 (1999).

[98] M. Greiner, M. Helander, W.-M. Tang, Z.-B. Wang, J. Qiu and Z.-H. Lu, *Universal energy-level alignment of molecules on metal oxides*, Nature Materials **11**, 76 (2012).

[99] A. Ruff, M. Sing, R. Claessen, H. Lee, M. Tomić, H. Jeschke and R. Valentí, *Absence of metallicity in K-doped picene: Importance of electronic correlations*, Phys. Rev. Lett. **110**, 216403 (2013).

[100] K. Horn, M. Alonso and R. Cimino, *Non-equilibrium effects in photoemission from metal-semiconductor interfaces*, Appl. Surf. Sci. **56-58**, 271 (1992).

[101] N. Koch, C. Chan, A. Kahn and J. Schwartz, *Lack of thermodynamic equilibrium in conjugated organic molecular thin films*, Phys. Rev. B **67**, 195330 (2003).

[102] M. H. Hecht, *Role of photocurrent in low-temperature photoemission studies of Schottky-barrier formation*, Phys. Rev. B (R) **41**, 7918 (1990).

[103] M. Alonso, R. Cimino and K. Horn, *Surface photovoltage effects in photoemission from metal-GaP(110) interfaces: Importance for band-bending evaluation*, Phys. Rev. Lett. **64**, 1947 (1990).

[104] M. Moreno, M. Alonso, M. H. ricke, R. Hey, K. Horn, J. S. n and K. Ploog, *Photoemission results on intralayer insertion at III-V/III-V junctions: A critical appraisal of the different interpretations*, J. Vac. Sci. Technol. B **18(4)**, 2128 (2000).

[105] S. Sze and K. Ng, *Physics of Semiconductor Devices*, John Wiley & Sons, Inc., Hoboken, New Jersey (2007).

[106] B. Henke, E. Gullikson and J. Davis, *X-ray interactions: photoabsorption, scattering, transmission, and reflection at* $E = 50 - 30,000$ *V,* $Z = 1 - 92$, At. Data Nucl. Data Tables **54**, 181 (1993).

[107] J. Kawai, M. Takami, M. Fujinami, Y. Hashiguchi, S. Hayakawa and Y. Gohshi, *A numerical simulation of total reflection X-ray photoelectron spectroscopy (TRXPS)*, Spectrochim. Acta **47B**, 983 (1992).

[108] J. Scott and G. Malliaras, *Charge injection and recombination at the metal-organic interfaces*, Chem. Phys. Lett. **299**, 115 (1999).

[109] J. Delany and J. Hirsch, *Conductivity induced by electron bombardment in anthracene*, Solid State Commun. **4**, 107 (1966).

[110] J. Keister, J. Rowe, J. Kolodziej and T. Madey, *Photoemission spectroscopy of platinum overlayers on silicon dioxide films*, J. Vac. Sci. Technol. B **18(4)**, 2174 (2000).

[111] D. Schrupp, M. Sing, M. Tsunekawa, H. Fujiwara, S. Kasai, A. Sekiyama, S. Suga, T. Muro, V. Brabers and R. Claessen, *High-energy photoemission on* Fe_3O_4*: Small polaron physics and the Verwey transition*, Europhys. Lett. **70(6)**, 789 (2005).

[112] A. Alexandrov and J. Ranninger, *Polaronic effects in the photoemission spectra of strongly coupled electron-phonon systems*, Phys. Rev. B **45**, 13109 (1992).

[113] R. Claessen, M. Sing, U. Schwingenschlögl, P. Blaha, M. Dressel and C. Jacobsen, *Spectroscopic signatures of spin-charge separation in the quasi-one-dimensional organic conductor TTF-TCNQ*, Phys. Rev. Lett. **88**, 096402 (2002).

[114] M. Knupfer, H. Peisert and T. Schwieger, *Band-gap and correlation effects in the organic semiconductor* Alq_3, Phys. Rev. B **65**, 033204 (2001).

[115] R. Lof, M. van Veenendaal, B. Koopmans, H. Jonkman and G. Sawatzky, *Band gap, excitons, and Coulomb interaction in solid C_{60}*, Phys. Rev. Lett. **68**, 3924 (1992).

[116] F. Roth, B. Mahns, B. Büchner and M. Knupfer, *Exciton character in picene molecular solids*, Phys. Rev. B **83**, 165436 (2011).

[117] A. Ruff, M. Sing, R. Claessen, H. Lee, M. Tomić, H. Jeschke and R. Valentí, *Absence of metallicity in K-doped picene: Importance of electronic correlations*, arXiv:12104065, accepted for publication in Phys. Rev. Lett.

[118] M. Imada, A. Fujimori and Y. Tokura, *Metal-insulator-transitions*, Rev. Mod. Phys. **70**, 1039 (1998).

[119] T. Kambe, X. He, Y. Takahashi, Y. Yamanari, K. Teranishi, H. Mitamura, S. Shibasaki, K. Tomita, R. Eguchi, H. Goto, Y. Takabayashi, T. Kato, A. Fujiwara, T. Kariyado, H. Aoki and Y. Kubozono, *Synthesis and physical properties of metal doped picene solids*, Phys. Rev. B **86**, 214507 (2012).

[120] D. Poirier, *Isolation of fulleride phases by distillation*, Appl. Phys. Lett. **64**, 1356 (1994).

[121] M. Kim, B. Min, H. Choi and J. Shim, *Correlated electronic structure and the phase diagram of hydrocarbon-based superconductors*, arXiv:1304.1613v1.

[122] S. Qiu, C. Lin, J. Chen and M. Strongin, *Photoemission studies of the low-temperature reaction of metals and oxygen*, Phys. Rev. B **41**, 7467 (1990).

[123] J. Moulder, W. Stickle, P. Sobol and K. Bomben, *Handbook of X-ray Photoelectron Spectroscopy*, Perkin-Elmer Corporation (1992).

[124] R. D. Souza, V. Metlenko, D. Park and T. Weirich, *Behavior of oxygen vacancies in single-crystal $SrTiO_3$: Equilibrium distribution and diffusion kinetics*, Phys. Rev. B **85**, 174109 (2012).

[125] M. Ramsey, M. Schatzmayr, S. Stafström and F. Netzer, *Interacting bipolarons in n-doped sexiphenyl films*, Europhys. Lett. **28**, 85 (1994).

[126] P. Bröms, N. Johansson, R. Gymer, S. Graham, R. Friend and W. Salaneck, *Low energy electron degradation of poly(p-phenylene vinylene)*, Adv. Mater. **11**, 826 (1999).

[127] F. Amy, C. Chan, W. Zhao, J. Hyung, M. Ono, T. Sueyoshi, S. Kera, G. Nesher, A. Salomon, L. Segev, O. Seitz, H. Shpaisman, A. Schöll, M. Haeming, T. Böcking, D. Cahen, L. Kronik, N. Ueno, E. Umbach and A. Kahn, *Radiation damage to alkyl chain monolayers on semiconductor substrates investigated by electron spectroscopy*, J. Phys. Chem. B **110**, 21826 (2006).

[128] N. Greenwood and A. Earnshaw, *Chemistry of Elements*, VCH, Weinheim (1988).

[129] H. Sirringhaus, T. Kawase, R. H. Friend, T. Shimoda, M. Inbasekaran, W. Wu and E. P. Woo, *High-resolution inkjet printing of all-polymer transistor circuits*, Science **290**, 2123 (2000).

[130] G. H. Gelinck, H. E. A. Huitema, E. van Veenendaal, E. Cantatore, L. Schrijnemakers, J. B. P. H. van der Putten, T. C. T. Geuns, M. Beenhakkers, J. B. Giesbers, B.-H. Huisman, E. J. Meijer, E. M. Benito, F. J. Touwslager, A. W. Marsmann, B. J. E. van Reens and D. M. de Leuw, *Flexible active-matrix displays and shift registers based on solution-processed organic transistors*, Nature Mater. **3**, 106 (2004).

[131] H. Klauk, U. Zschieschang, J. Pflaum and M. Halik, *Ultralow-power organic complementary circuits*, Nature **445**, 745 (2007).

[132] D. J. Gundlach, T. N. Jackson, D. G. Schlom and S. F. Nelson, *Solvent-induced phase transition in thermally evaporated pentacene films*, Appl. Phys. Lett. **74**, 3302 (1999).

[133] O. D. Jurchescu, T. Baas and T. T. M. Palstra, *Effect of impurities on the mobility of single crystal pentacene*, Appl. Phys. Lett. **84**, 3061 (2004).

[134] S. F. Nelson, Y.-Y. Lin, D. J. Gundlach and T. N. Jackson, *Temperature-independent transport in high-mobility pentacene transistors*, Appl. Phys. Lett. **72**, 1854 (1998).

[135] C. D. Dimitrakopoulos and P. R. L. Malenfant, *Organic thin film transistors for large area electronics*, Adv. Mater. **14**, 99 (2002).

[136] G. Brocks, J. van den Brink and A. F. Morpurgo, *Electronic correlations in oligoacene and -thiopene organic molecular crystals*, Phys. Rev. Lett. **93**, 146405 (2004).

[137] M. Sing, J. Meyer, M. Hoinkis, S. Glawion, P. Blaha, G. Gavrila, C. Jacobsen and R. Claessen, *Structural vs electronic origin of renormalized band widths in TTF-TCNQ: An angular dependent NEXAFS study*, Phys. Rev. B **76**, 245119 (2007).

[138] A. Goldoni, S. Friedmann, Z.-X. Shen and F. Parmigiani, *Correlation and electron-phonon effects in the valence-band photoemission spectra of single-phase K_3C_{60} film*, Phys. Rev. B **58**, 11023 (1998).

[139] C. Mattheus, A. Dros, J. Baas, A. Meetsma, J. de Boer and T. Palstra, *Polymorphism in pentacene*, Acta Chryst. **C57**, 939 (2001).

[140] W.-H. Soe, C. Manzano, A. D. Sarkar, N. Chandrasekhar and C. Joachim, *Direct observation of molecular orbitals of pentacene physisorbed on Au(111) by scanning tunneling microscope*, Phys. Rev. Lett. **102**, 176102 (2009).

[141] S. Lukas, S. Söhnchen, G. Witte and C. Wöll, *Epitaxial growth of pentacene films on metal surfaces*, ChemPhysChem **5**, 266 (2004).

[142] I. P. M. Bouchoms, W. A. Schoonveld, J. Vrijmoeth and T. M. Klapwijk, *Morphology identification of the thin film phases of vacuum evaporated pentacene on SiO_2 substrates*, Synth. Met. **104**, 175 (1999).

[143] J. H. Kang and X.-Y. Zhu, *Pi-stacked pentacene thin films grown on Au(111)*, Appl. Phys. Lett. **82**, 3248 (2003).

[144] D. Faltermeier, B. Gompf, M. Dressel, A. Tripathi and J. Pflaum, *Optical properties of pentacene thin films and single crystals*, Phys. Rev. B **74**, 125416 (2006).

[145] E. Silinsh, V. Kolesnikov, I. Muzikante and D. Balode, *On charge carrier photogeneration mechanisms in organic molecular crystals*, Phys. Stat. Sol. B **113**, 379 (1982).

[146] F. Amy, C. Chan and A. Kahn, *Polarization at the gold/pentacene interface*, Org. Electron. **6**, 85 (2005).

[147] T. Minakata, M. Ozaki and H. Imai, *Conducting thin films of pentacene doped with alkaline metals*, J. Appl. Phys. **74**, 1079 (1993).

[148] Y. Matsuo, S. Sasaki and S. Ikehata, *Stage structure and electrical properties of rubidium-doped pentacene*, Phys. Lett. A **321**, 62 (2004).

[149] Y. Matsuo, T. Suzuki, Y. Yokoi and S. Ikehata, *Stage structure in cesium doped pentacene*, J. Phys. Chem. Solids **65**, 619 (2004).

[150] Y. Kaneko, T. Suzuki, Y. Matsuo and S. Ikehata, *Metallic electrical conduction in alkaline metal-doped pentacene*, Syth. Met. **154**, 177 (2005).

[151] R. Ruiz, B. Nickel, N. Koch, L. C. Feldman, R. F. Haglund, A. Kahn and G. Scoles, *Pentacene ultrathin film formation on reduced and oxidized Si surfaces*, Phys. Rev. B **67**, 125406 (2003).

[152] P. Parisse, S. Picozzi, M. Passacantando and L. Ottaviano, *Experiments and theory on pentacene in the thin film phase: structural, electronic, transport properties, and gas response to oxygen, nitrogen, and ambient air*, Thin Solid Films **515**, 8316 (2007).

[153] D. Käfer, C. Wöll and G. Witte, *Thermally activated dewetting of organic thin films: the case of pentacene on SiO_2 and gold*, Appl. Phs. A **95**, 273 (2009).

[154] A. Brillante, I. Bilotti, R. della Valle, E. Venuti, A. Girlando, M. Masino, F. Liscio, S. Milita, C. Albonetti, P. D'angelo, A. Shehu and F. Biscarini, *Structure and dynamics of pentacene on SiO_2: From monolayer to bulk structure*, Phys. Rev. B **85**, 195308 (2012).

[155] M. E. Helou, E. Lietke, J. Helzel, W. Heimbrodt and G. Witte, *Structural and optical properties of pentacene films grown on differently oriented ZnO surfaces*, J. Phys.: Condens. Matter **24**, 445012 (2012).

[156] R. Ruiz, D. Choudhary, B. Nickel, T. Toccoli, K.-C. Chang, A. C. Mayer, P. Clancy, J. M. Blakely, R. L. Headrick, S. Ianotta and G. G. Malliaras, *Pentacene thin film growth*, Chem. Mater. **16**, 4497 (2004).

[157] H. Yoshida and N. Sato, *Crystallographic and electronic structures of three different polymorphs of pentacene*, Phys. Rev. B **77**, 235205 (2008).

[158] A. Hansson, J. Böhlin and S. Stafström, *Structural and electronic transitions in potassium-doped pentacene*, Phys. Rev. B **73**, 184114 (2006).

[159] A. Vollmer, H. Weiss, S. Rentenberger, I. Salzmann, J. Rabe and N. Koch, *The interaction of oxygen and ozone with pentacene*, Surf. Sci. **600**, 4004 (2006).

[160] N. Watkins and Y. Gao, *Interface formation and energy level alignment of pentacene on SiO_2*, J. Appl. Phys. **94**, 5782 (2003).

[161] H. Fukagawa, H. Yamane, T. Kataoka, S. Kera, M. Nakamura, K. Kudo and N. Ueno, *Origin of the highest occupied band position in pentacene films from ultraviolet photoelectron spectroscopy: Hole stabilization versus band dispersion*, Phys. Rev. B **73**, 245310 (2006).

[162] S. Cho, D. Park, W. Jang, M.-H. C. K.-H. Yoo, K. Jeong, C.-N. Whang, Y. Yi and K. Chung, *Electronic structure of pentacene/ultrathin gate dielectric interfaces for low-voltage organic thin film transistors*, J. Appl. Phys. **102**, 064502 (2007).

[163] F. Li, P. Graziosi, Q. Tang, Y. Zhan, X. Liu, V. Dediu and M. Fahlmann, *Electronic structure and molecular orientation of pentacene thin films on ferromagnetic $La_{0.7}Sr_{0.3}MnO_3$*, Phys. Rev. B **81**, 205415 (2010).

[164] C. Baldacchini, F. Allegretti, R. Gunnella and M. G. Betti, *Molecule-metal interaction of pentacene on copper vicinal surfaces*, Surf. Sci. **601**, 2603 (2007).

[165] M. L. Ng, A. B. Preobrajenski, A. A. Zakharov, A. S. Vinogradov, S. A. Krasnikov, A. A. Cafolla and N. M. rtensson, *Effect of substrate nanopatterning on the growth and structure of pentacene films*, Phys. Rev. B **81**, 115449 (2010).

[166] M. Alagia, C. Baldacchini, M. G. Betti, F. Bussolotti, V. Carravetta, U. Ekström, C. Mariani and S. Stranges, *Core-shell photoabsorption and photoelectron spectra of gas-phase pentacene: Experiment and theory*, J. Chem. Phys. **122**, 124305 (2005).

[167] M. Helander, M. Greiner, Z. Wang and Z. Lu, *Effect of electrostatic screening on apparent shifts in photoemission spectra near metal/organic interfaces*, Phys. Rev. B **81**, 153308 (2010).

[168] J. Szczepanski, C. Wehlburg and M. Vala, *Vibrational and electronic spectra of matrix-isolated pentacene cations and anions*, Chem. Phys. Lett. **232**, 221 (1995).

[169] T. Halasinski, D. Hudgins, F. Salama and L. Allamandola, *Electronic absorption of neutral pentacene ($C_{22}H_{14}$) and its positive and negative ions in Ne, Ar, and Kr matrices*, J. Phys. Chem. A **104**, 7484 (2000).

[170] G. Sawatzky, *Testing Fermi-liquid models*, Nature **342**, 480 (1989).

[171] P. Benning, D. Poirier, T. Ohno, Y. Chen, M. Jost, F. Stepniak, G. Kroll, J. Weaver, J. Fure and R. Smalley, *C_{60} and C_{70} fullerenes and potassium fullerides*, Phys. Rev. B **45**, 6899 (1992).

[172] T. Kato and T. Yamabe, *Electron-intramolecular-phonon coupling and possible superconductivity in negatively charged coronene and corannulene*, J. Chem. Phys. **117**, 2324 (2002).

[173] T. Kosugi, T. Miyake, S. Ishibashi, R. Arita and H. Aoki, *Ab initio electronic structure of solid coronene: Differences from and commonalities to picene*, Phys. Rev. B **84**, 020507 (2011).

[174] T. Echigo, M. Kimata and T. Maruoka, *Crystal-chemical and carbon-isotopic characteristics of karpatite ($C_{24}H_{12}$) from the Picacho Peak Area, San Benito County, California: Evidences for the hydrothermal formation*, Am. Mineral. **92**, 1262 (2007).

[175] P. Schroeder, C. France, B. Parkinson and R. Schlaf, *Orbital alignment at p-sexiphenyl and coronene/layered materials interfaces measured with photoemission spectroscopy*, J. Appl. Phys. **91**, 9095 (2002).

[176] P. Djurovich, E. Mayo, S. Forrest and M. Thompson, *Measurement of the lowest unoccupied molecular orbital energies of molecular organic semiconductors*, Org. Electron. **10**, 515 (2009).

[177] F. Roth, J. Bauer, B. Mahns, B. Büchner and M. Knupfer, *Electronic structure of undoped and potassium-doped coronene investigated by electron energy-loss spectroscopy*, Phys. Rev. B **85**, 014513 (2012).

[178] K. Walzer, M. Sternberg and M. Hietschold, *Formation and characterization of coronene monolayers on HOPG(0001) and MoS_2(0001): a combined STM/STS and tight-binding study*, Surf. Sci. **415**, 376 (1998).

[179] K. Cho, T. Shimada, M. Sakurai and A. Koma, *Effect of growth temperature and substrate materials on epitaxial growth of coronene*, J. Appl. Phys. **84**, 268 (1998).

[180] L. Zhang, D. Shi, S. Du, L. Chi, H. Fuchs and H.-J. Gao, *Structural transition and thermal stability of a coronene molecular monolayer on Cu(110)*, J. Phys. Chem. C **114**, 11180 (2010).

[181] M. Möbus, M. Schreck and N. Karl, *Epitaxial growth of thin films of perylenetetracarboxylic dianhydride and coronene on NaCl(001)*, Thin Solid Films **175**, 89 (1989).

[182] J.-L. Lin, D. Petrovykh, J. Viernow, F. Men, D. Seo and F. Himpsel, *Formation of regular step arrays on Si(111)*7×7, J. Appl. Phys. **84**, 255 (1998).

[183] M. Casu, Y. Zou, S. K. D. Batchelor, T. Schmidt and E. Umbach, *Investigation of polarization effects in organic thin films by surface core-level shifts*, Phys. Rev. B **76**, 193311 (2007).

[184] G. Koster, B. L. Kropmann, G. Rijnders, D. H. A. Blank and H. Rogalla, *Quasi-ideal strontium titanate crystal surfaces through formation of strontium hydroxide*, Appl. Phys. Lett. **73**, 2920 (1998).

[185] M. Knupfer, J. Fink, J. Armbruster and H. Romberg, *Preparation and electronic structure of phase pure K_3C_{60}*, Z. Phys. B **98**, 9 (1995).

[186] F. A. Cotton, G. Wilkinson, C. Murillo and M. Bochmann, *Advanced Inorganic Chemistry, 6th ed.*, Wiley, New York (1999).

[187] G. Brodén, G. Pirug and H. Bonzel, *Adsorption of oxygen on potassium-covered Pt(111) and Fe(110)*, Chem. Phys. Lett. **73**, 506 (1980).

[188] E. Bertel, F. Netzer, G. Rosina and H. Saalfeld, *Alkali-metal oxides. I. Molecular and crystal-field effects in photoemission*, Phys. Rev. B **39**, 6082 (1989).

[189] J. Jupille, P. Dolle and M. Besançon, *Ionic oxygen species formed in the presence of lithium, potassium and cesium*, Surf. Sci. **260**, 271 (1992).

[190] M. Merkel, M. Knupfer, M. Golden, J. Fink, R. Seemann and R. Johnson, *Photoemission study of the electronic structure of C_{60} and K_xC_{60}*, Phys. Rev. B **47**, 11470 (1993).

[191] J. Wu, M. Ma, H. Zheng, H. Yang, J. Zu and M. Ji, *Photoemission study of the effect of annealing temperature on a K_2O_2/Si(100) surface*, Phys. Rev. B **60**, 17102 (1999).

[192] S. Qiu, C. Lin, J. Chen and M. Strongin, *Photoemission studies of the interaction of Li and solid molecular oxygen*, Phys. Rev. B **39**, 6194 (1989).

[193] R. Bulla, *Zero temperature metal-insulator transition in the infinite-dimensional Hubbard model*, Phys. Rev. Lett. **83**, 136 (1999).

List of own publications

- **A. Ruff**, S. Schatz, M. Sing, and R. Claessen, *Valence band photoemission of K-doped picene films: The role of extrinsic contributions to the electronic structure*, in preparation.
- **A. Ruff**, J. Loos, M. Sing, and R. Claessen, *Photoemission of K-doped pentacene thin films: The role of electron correlations*, in preparation.
- **A. Ruff**, M. Sing, R. Claessen, H. Lee, M. Tomić, H.O. Jeschke, and R. Valentí, *Absence of metallicity in K-doped picene: Importance of electronic correlations*, Phys. Rev. Lett. **110**, 216403 (2013).
- M. Paul, D. Kufer, A. Müller, **A. Ruff**, M. Kamp, N.J.C. Ingle, M. Sing, and R. Claessen, *Surface structure, morphology, and growth mechanism of Fe_3O_4/ZnO thin films*, J. Appl. Phys. **110**, 073519 (2011).
- A. Müller, **A. Ruff**, M. Paul, A. Wetscherek, G. Berner, U. Bauer, C. Praetorius, K. Fauth, M. Przybylski, M. Gorgoi, M. Sing, and R. Claessen, *Fe_3O_4 on ZnO: A spectroscopic study of film and interface properties*, Thin Solid Films **520**, 368 (2011).
- C. Blumenstein, S. Meyer, **A. Ruff**, B. Schmid, J. Schäfer, and R. Claessen, *High purity chemical etching and thermal passivation process for Ge(001) as nanostructure template*, J. Chem. Phys. **135**, 064201 (2011).
- S. Glawion, J. Heidler, M.W. Haverkort, L.C. Duda, T. Schmitt, V.N. Strocov, C. Monney, K. J. Zhou, **A. Ruff**, M. Sing, and R. Claessen, *Two-spinon and orbital excitations of the spin-Peierls system TiOCl*, Phys. Rev. Lett. **107**, 107402 (2011).
- M. Paul, A. Müller, **A. Ruff**, B. Schmid, G. Berner, M. Sing, R. Claessen, and M. Mertin, *Probing the interface of $Fe_3O_4/GaAs$ thin films by hard x-ray photoelectron spectroscopy*, Phys. Rev. B **79**, 233101 (2009).
- M. Sing, G. Berner, K. Go, A. Müller, **A. Ruff**, A. Wetscherek, S. Thiel, J. Mannhart, S.A. Pauli, C.W. Schneider, P.R. Willmott, M. Gorgoi, F. Schäfers, and R. Claessen, *Profiling the interface electron gas of $LaAlO_3/SrTiO_3$ heterostructures by hard X-ray photoelectron spectroscopy*, Phys. Rev. Lett. **102**, 176805 (2009).

Danksagung

Da dieses Schriftstück zwar das Werk eines Einzelnen ist, die Entstehung des Ganzen aber mit Vielen verbunden ist, möchte ich an dieser Stelle allen danken, die daran beteiligt waren:

- In erster Linie gilt mein Dank Prof. Dr. Ralph Claessen, dass er mir in seiner Eigenschaft als Doktorvater die Möglichkeit gegeben hat, diese Promotion durchzuführen. Ebenso danke ich für etliche Gelegenheiten, meine Forschungsergebnisse auf Tagungen und Schulen zu präsentieren.
- Weiterhin möchte ich Priv.-Doz. Dr. Michael Sing meinen Dank aussprechen, der mich zusammen mit Prof. Claessen in die Welt der korrelierten Organik einführte, und der immer eine Antwort auf meine zahlreichen Fragen wusste. Vielen Dank auch für das Korrekturlesen dieser Arbeit.
- Außerdem danke ich Prof. Dr. Jens Pflaum für die Bereitschaft, zweiter Gutachter dieser Arbeit zu sein, sowie für viele fruchtbare Diskussionen, und Nis Hauke Hansen aus seiner Arbeitsgruppe für "haufenweise" XRD-Messungen.
- Dank gilt auch Prof. Dr. Roser Valentí von der Universität Frankfurt für die Bereitschaft, dritter Prüfer bei der Doktorprüfung zu sein, sowie ihr und ihren Mitarbeitern Harald Jeschke und Hunpyo Lee für die fruchtbare Kollaboration zwischen Experiment und Theorie.
- Zudem danke ich Florian Kronast und Team an der UE49-PGM-A-SPEEM beamline für die fantastische Unterstützung bei zwei Strahlzeiten, sowie Friedrich Roth und Benjamin Mahns vom IFW Dresden für die gemeinsame Strahlzeit und angenehme Diskussionen.
- Des Weiteren danke ich Benni, Markus, Sebastian, Philipp, Christian, Sebastian, Alexey und Götz (den Alt-Doktoranden) für alles, was ich von ihnen lernen konnte und eine schöne Zeit. Danke auch noch einmal an Markus, Lenart, Philipp, Sebastian und Julian fürs Korrekturlesen.
- Besonderer Dank gilt Andi, von dem ich nicht nur viel gelernt habe, sondern mit dem die Zeit auch äußerst angenehm war, wobei regelmäßige Apfelpausen nur ein Punkt unter vielen waren.
- Und natürlich vielen Dank an alle (Aktive und Ehemalige) vom Team der EP4, allen voran Moni, die bei allem nur möglichen immer gerne geholfen hat.
- Zu guter Letzt danke ich meiner Familie, meiner Freundin und meinen Freunden für Unterstützung in jeglicher Hinsicht, oder einfach auch nur fürs Dasein.